

Synthesis, Characterization and Swift Heavy Ion Induced Modification of Semiconductor (Ge & Si) Nanocrystals

A Thesis Submitted for the Degree of

Doctor of Philosophy

By

**VADAVALLI SAIKIRAN
(08PHPH12)**



**School of Physics
University of Hyderabad
Hyderabad – 500046 India
July 2013**



&
To my mother and myself

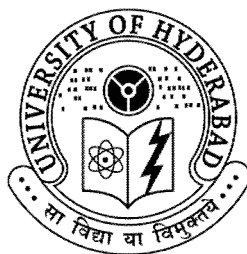
DECLARATION

I hereby declare that the matter embodied in the thesis entitled “**Synthesis, Characterization and Swift Heavy Ion Induced Modification of Semiconductor (Ge & Si) Nanocrystals**” is the result of investigation carried out by me in the School of Physics, University of Hyderabad, India, under direct supervision of **Prof. Anand P Pathak**. This work has not been submitted for any other degree or diploma either in part or in full to this or to any other University or Institution.

Place: Hyderabad

(V. Saikiran)

Date:



CERTIFICATE

This is to certify that the work described in this thesis entitled **“Synthesis, Characterization and Swift Heavy Ion Induced Modification of Semiconductor (Ge & Si) Nanocrystals”** has been carried out by **Mr V. Saikiran**, under my direct supervision and this has not been submitted for any degree or diploma at this or any other University.

Place: Hyderabad

Date:

(Prof. Anand P Pathak)

Dean School of Physics

Table of Contents

Declaration	ii
Certificate	iii
Acknowledgements	iv
Chapter 1 Introduction and Motivation	1-24
1.1 Motivation	2
1.2 Basics of Ion-Solid Interaction	4
1.3 Ion penetration and Stopping	7
1.3.1 Energy loss processes	7
1.3.2 Stopping power	7
1.3.3 Nuclear energy loss	7
1.3.4 Electronic energy loss	8
1.3.5 Comparison of electronic and nuclear stopping	8
1.3.6 Swift heavy ion irradiation and tracks	10
1.3.7 Effective charge	11
1.4 Swift heavy ion induced effects in materials	11
1.4.1 Thermal spike	11
1.4.2 Coulomb explosion	12
1.5 Materials of interest	13
1.5.1 Introduction to nanoscience and nanotechnology	13
1.5.1 Introduction to nanoscience and nanotechnology	14
1.6 Synthesis Methods	15
1.6.1 RF Magnetron Sputtering	16
1.7 Structure and organization of the thesis	16
1.8 References	19
Chapter 2 Experimental Methods	25-51
2.1 Introduction	26
2.2 Samples Growth methods	26
2.3 Radio Frequency Magnetron Sputtering (RF sputtering)	28
2.3.1 Sputtering Yield	29
2.4 Accelerator facilities	30
2.4.1 Pelletron details	30
2.4.2 Tandem accelerator at IGCAR	32
2.4.2.1 Duoplasmatron ion Source	33

2.4.2.2 Negative sputter ion source	33
2.4.3 RBS facility	33
2.4.4 Ion implantation	36
2.5 Rapid thermal annealing (RTA)	37
2.6 Structural characterization 6 X-ray Diffraction (XRD)	38
2.6.1 Crystallite size and lattice parameter calculation	39
2.7 Micro-Raman spectroscopy	40
2.8 Field Emission-Scanning Electron Microscopy (FE-SEM)	41
2.9 Energy dispersive x-ray absorption spectroscopy (EDS)	44
2.10 Transmission Electron Microscopy (TEM)	46
2.11 Atomic force microscopy	48
2.12 Thickness measurement: Surface profilometer	50
2.13 Conclusions	50
2.14 References	51

Chapter 3 Synthesis and Characterization of Ge NCs embedded in SiO₂ and the effects of heavy ion irradiation on these NCs

52-77

3.1 Introduction	53
3.2 Experimental Details	54
3.3 Results and discussion	56
3.3.1 RBS results	56
3.3.2 XRD results	57
3.3.3 Raman results	63
3.3.3 TEM results	67
3.4 Crystallization of Ge implanted SiO ₂ films	71
3.5 Conclusions	75
3.6 References	76

Chapter 4 Synthesis and Characterization of Ge NCs embedded in HfO₂

78-91

4.1 Introduction	79
4.2 Experimental details	80
4.3 Results and Discussions	82
4.3.1 RBS results	82
4.3.2 XRD Results	83
4.3.3 Raman Results	86
4.4 Ion irradiation effects	88
4.5 Conclusions	89

4.6 References	90
Chapter 5 Synthesis, Characterization and the effects of heavy ion irradiation on Ge/GeO₂ NCs	92-106
5.1 Introduction	93
5.2 Experimental Details	93
5.3 Results and discussion	94
5.3.1 RBS results	95
5.3.2 XRD results	95
5.3.3 Micro-Raman Spectroscopy	97
5.3.4 FESEM-EDS and TEM results	98
5.3.5 AFM results	103
5.4 Conclusions	104
5.5 References	105
Chapter 6 Swift heavy ion irradiation effects on Si nanoparticles	107-125
6.1 Introduction	108
6.2 Experimental details	109
6.3 Results and Discussion	110
6.3.1 Raman Results	110
6.3.2 FESEM	113
6.3.3 TEM	114
6.4 Conclusions	122
6.5 References	123
Chapter 7 Conclusions and future outlook	126-129
7.1 Summery of the results	127
7.2 Future outlook	128
CV with list of publications	130-133

Acknowledgements

It would not have been possible to complete this doctoral thesis without the help and support of many nice people around me. It is possible to mention only few of these here.

Above all, I express my gratitude and profound thanks to my thesis supervisor, Prof Anand P Pathak, for his inspiring guidance and constant encouragement throughout the course of this research work. I have been able to learn a great deal in this fascinating field of research through his inspiring and thought provoking discussions, and I consider my association with him a rewarding experience. I also thank his family members for their help.

I thank Prof S Chaturvedi, Dean, School of Physics, former Deans Prof Vipin Srivastava, Prof C Bansal and Prof S P Tewari for their co-operation in providing facilities in the School. I am privileged to have Prof S N Kaul as my Doctoral Committee member whose suggestions and insights have improved the understanding of our results. I thank Prof Ashok Chatterjee and Prof K P N Murthy, for their teaching (Advanced Quantum Mechanics, Advanced Electromagnetic Theory and Advanced Statistical Mechanics) during PhD course work. I thank Prof C S Sunandana and Prof M Ghanashyam Krishna for their encouragement and suggestions during various DC meetings. I sincerely thank Prof P Ananta Lakshmi for her interest and for encouraging words during various interactions. I thank Prof D Narayana Rao for his inspiring words about collaborative research during our interaction. The support provided by Abraham is greatly acknowledged.

I thank Dr Soma Venugopal Rao, ACRHEM and his student Mr Hamad for extending their help in the synthesis of Si NPs by laser ablation for our studies. I take this opportunity to thank Dr Achanta Venu Gopal of TIFR for his help, encouragement and suggestions whenever needed from the time of my admission to PhD to till date.

I am grateful to Prof C Rangacharyulu of Department of Physics and Engineering Physics, University of Saskatchewan, Saskatoon for showing me an opportunity to visit U of S through Canadian commonwealth scholarship program. I thank Prof Gap Soo Chang for accepting me to work in his lab under Canadian commonwealth scholarship scheme. The discussions with him helped me in improving my understanding of the results and his motivational words have inspired me a lot to develop the strength. I thank his group members Paul Bazylewski, Robert Bauer, M M Hussain and Kushbhu for their support during my stay

in Saskatoon. I thank my Indian friend Mr Rishi Vyas for his discussions in U of S during our interactions. I once again thank all the colleagues and telugu friends of Saskatoon.

I thank Dr D K Avasthi for his valuable suggestions during beam time experiments at IUAC. I am also thankful to the members of Pelletron group and other supporting labs in IUAC for necessary support during experiments. I am very much thankful to Dr D Kanjilal for his interest in our work and the suggestions he gave during our discussions. I express my sincere thanks to Mr Saif A Khan for extending help during the beam time experiments. I also thank Lakshmi Akka and her family for their interaction during our stay at IUAC. I thank Dr K G M Nair and Dr B Sundaravel for their suggestions and help during our experiments at IGCAR, Kalpakkam.

I thank CSIR India for providing me financial support in the form of JRF and SRF throughout the period of my work. The international travel support received from DST, India to present my work in 22nd CAARI 2012, in Fort worth, Texas, USA is greatly acknowledged.

I should also express my sincere thanks to Dr S V S Nageswara Rao for his constant support in the development of my research work. The good advice, support and friendship he has given is invaluable on both academic and personal level, for which I am extremely grateful to him. Also I thank Dr Sai Saravanan and Dr Siddiqui who helped me during different discussions. My special word of thanks and appreciation to all my lab seniors, Dr N Sathish, Dr Juby George, Dr N Srinivasa Rao and Dr G Devaraju for constantly encouraging and supporting me throughout my time here and directly helping me in getting into suitable research problems. A special thanks to Srinivas and Deva for their personal interest and friendly support in both academic and personal matters whenever needed. Thanks to my present lab members Vendamani, Manikantha, Dhanunjaya and Arun for creating friendly and pleasant lab atmosphere.

I also thank technical staff Deepthi, Laxmi Narayana, Thirumalaiah, Sandhya, and Durga Prasad for their help. I thank all my friends from my childhood to till date. It is difficult to mention all the names here but a special mention of cheers for the help and support received from good friends Ratnaji, Ranga, Kalyan, Lalitha, Pavan, Sirisha, Raghuram, Praveen, Sreeramulu, Sita, Pardhu, Vasu, Anil and Deepak is essential. My stay on this campus has been pleasant due to association of many other students and friends from various labs. On this occasion I thank each and every one for their interaction and help. A special thanks to all my

-08 batch mates Dr Sreeramulu, Shankar, Sanjeev, Aalu, IV, Monisha, RV, Sriram, Soorat, Ahmed for wonderful time in the campus.

This is the time to express my gratitude to some of my relatives Madhu Mamayya and Vijayatta, Santipinni and Babaigar, Girijakka, Pedda Mamayya, Ram Mamayya and Chinna Vijayatta, Rambabu Babai and Ranga Pinni, Auntygaru (Lalitha's mother) who all have helped me to reach this place during various stages of my studies.

Last but the MOST, I thank my wife Chandrika, for her love, personal support and great patience at all times. My parents and in-laws have given me their unequivocal support throughout, for which my mere expression of thanks does not suffice.

I express my deepest gratitude to all the Gods for being with me all the time and for listening to my prayers to achieve this long time dream.

I thank all of them who have involved either directly or indirectly for the successful completion of this thesis.

V SAIKIRAN
Hyderabad

Chapter 1

Introduction and Motivation

1.1 Motivation

Irradiation of solids with energetic ions has imperative effects on the properties of target materials. Ion beams can act as a tool in the synthesis and modification of nanostructured materials [1]. Ion solid interactions give rise to various processes when solid materials are exposed to energetic ion beams. The main processes are penetration of ions into the solid material, backscattering from and transmission through the material, removal of atoms from the material surface (sputtering) and creation of defects and damage in the material which may even lead to amorphization of solid. In addition, electronic processes like excitation and ionization of target atoms as well as charge state modification of the projectile also takes place. These processes mainly depend on the type of ions, their energy and the type of solids [2]. These processes are well understood and utilized in ion beam analysis and ion beam modification of materials.

Ion beams have been used extensively for synthesis, modification and characterization of nanomaterials [3]. Ion beam irradiation also has been used for fabrication and characterization of the electronic devices in semiconductor industries. In the fast developing field of Nanoscience and Nanotechnology, the role and relevance of ion beams is assuming great significance. For example, energetic ion beams can be and have been used as a novel tool for nanostructuring of various materials [4]. On the other hand the fundamental problem in the field of materials science with ion beams is to understand the effects of ion solid interaction. During the interaction of heavy ions with the solids the material gets modified. The evolution of the materials during ion irradiation and the mechanism thereof, has to be understood. A common misconception is that the irradiation of solids with energetic ions has exclusively detrimental effects on the properties of target materials. In addition to the well-known cases of doping of bulk semiconductors [5] and ion beam nitriding of steels [6], recent experiments show that irradiation can also have beneficial effects on nanostructured systems. Ion beams may serve as tools to synthesize nanoclusters, nanocrystals and nanowires, change their morphology in a controllable manner and tailor their mechanical, electronic, and even magnetic properties [7-9]. In spite of the damage, ion irradiation may overall have a beneficial effect on the target. The best example of this is the well established technique of *ion implantation* in semiconductor industry [10]. This application motivated further studies of

ion irradiation induced modification of nanostructures. Another important example of a positive effect of irradiation coming from biophysics is the radiation-assisted treatment of cancer [11]. Our motivation is to understand the physics behind irradiation induced effects in semiconductor (Ge & Si) nanostructures and also the technical applicability of ion irradiation for the engineering of nanosystems with high precision.

Over the last two decades, there has been a prolific growth in the field of ion beam processing and modification studies of modern materials. These include synthesis of novel phases, tuning of structural, electrical, optical and magnetic properties of materials for various applications [12], ion beam patterning of surfaces [13], ion beam induced self-organization [14] and many more. A huge effort is being put to understand the ion beam synthesis and modification of nanostructured materials. The main issues in ion beam processing of materials can be grouped into three major areas as shown in Fig 1.1. (i) Physics issues ó Ion-solid interaction, diffusion/transport properties, (ii) Materials issues ó Evolution of materials, synthesis of novel phases, ion beam induced crystallization, (iii) Engineering issues ó Tuning materials properties, ion beam patterning, nanostructuring with ion beams. Although some overlaps are unavoidable, they can be understood reasonably well in terms of ion beam modification and the commonly available ion beam analysis techniques like Rutherford backscattering spectrometry (RBS), elastic recoil detection analysis (ERDA), nuclear reaction analysis (NRA) and particle induced X-ray emission (PIXE). The basic concepts of ion-solid interactions are explained in the following sections.

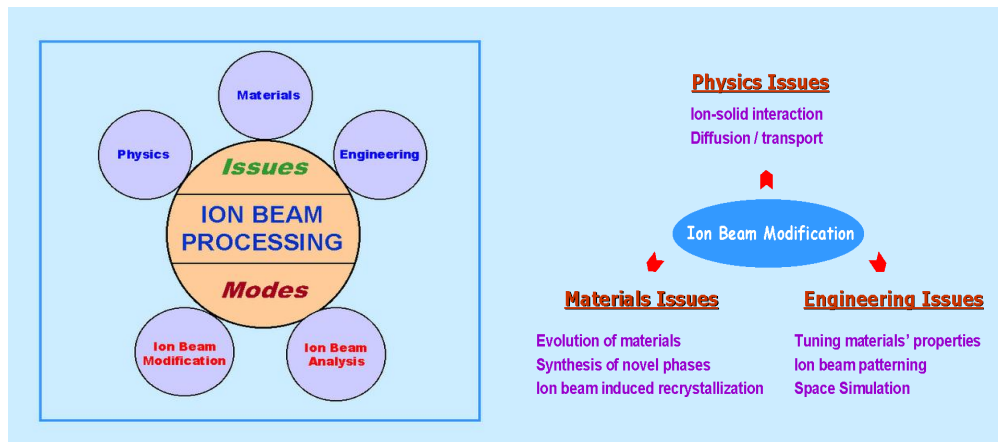


Fig 1.1: Issues of ion beam processing of materials

1.2 Basics of Ion-Solid Interaction

Energetic ion beams play an important role in the field of research in materials science. Ion beam irradiation effects on the material depend on ion energy, fluence and ion species. The interaction of ions with the materials is the governing factor in the ion beam induced modification of materials. Ion beam irradiation not only introduces the modification, but also used as an essential tool for material analysis. Ion propagation in solids creates radiation damage by means of energy loss and charge exchange process [15]. When an energetic ion moves through the material, it loses its energy by depositing/transferring it either to target electrons or to the target atom/ion as a whole. During this propagation of energetic ions in solid, a variety of processes occur. The incident ions may be reflected back right from the surface during collisions resulting in the process called back scattering. If the ions lose all their energy and come to rest within the solid, the process is called ion implantation. The atoms in host solid may be temporarily or permanently relocated to other lattice sites resulting in defects/vacancies. Actually during these collisions with the incident ions, the target atoms inside get recoiled. These recoiled atoms transfer their energy to their neighbouring atoms and in turn generate a collision cascade. Emitted and ejected particles or electromagnetic radiation upon ion bombardment gives information on the near-surface composition and structure. In this way ion irradiation produces structural modification of materials. Ion irradiation also induces mixing in bilayers or multilayers and produces alloys. In contrast to the normal interaction of energetic photons or electrons with the matter, the singular effect of energetic ion impact is extreme and associated with highly localized energy deposition in the target material.

As mentioned above the projectile energetic ion loses its energy through elastic and inelastic scattering processes and as a result, many interesting aspects can be observed which are illustrated below schematically in the Fig. 1.2.

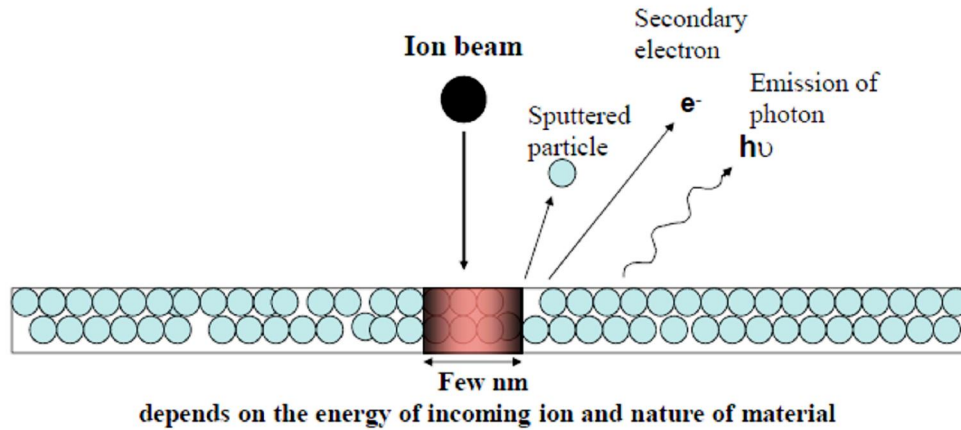


Fig 1.2: Basic ion-solid interaction process

The basic understanding of the interaction of ion beams with solids has its roots in atomic and nuclear physics. Interaction of energetic ions with atoms in a solid causes energy loss to the target atoms/ions through electronic and nuclear energy loss processes. These energy loss processes and their corresponding interaction probabilities at a given energy are responsible for various kinds of modifications that occur during the irradiation of solids with energetic ion beams.

The four main material modification processes which directly result from ion bombardment are illustrated in the Fig. 1.3 [16]. Ion implantation as shown in figure 1.3(a), can lead to the increase and build up of concentration of foreign atoms within the solid, thus altering the near surface composition. The distribution of foreign atoms depends on the ion energy and the stopping (nuclear and electronic) processes which determine how individual ions slow down and where they ultimately come to rest. Figure 1.3(b) illustrates that hard nuclear collisions can result in displacement of lattice atoms from their regular sites. A single heavy ion can lead to the displacement of several tens, and even hundreds, of lattice atoms within a volume surrounding the ion trajectory, known as collision or displacement cascade. As a consequence, ion bombardment can create considerable structural damage to the material. In figure 1.3(c), it has been shown that the nuclear collisions of a single ion can result in the ejection of one or more substrate atoms from the surface. Following bombardment with many ions, significant erosion (sputtering) of the surface can occur. Finally, figure 1.3(d) demonstrates the process of atomic mixing in which solid atoms can be transported within the

dimensions of the collision cascade. Ion bombardment can produce appreciable intermixing of both the substrate atoms into the film and the constituent atoms of the film into the substrate.

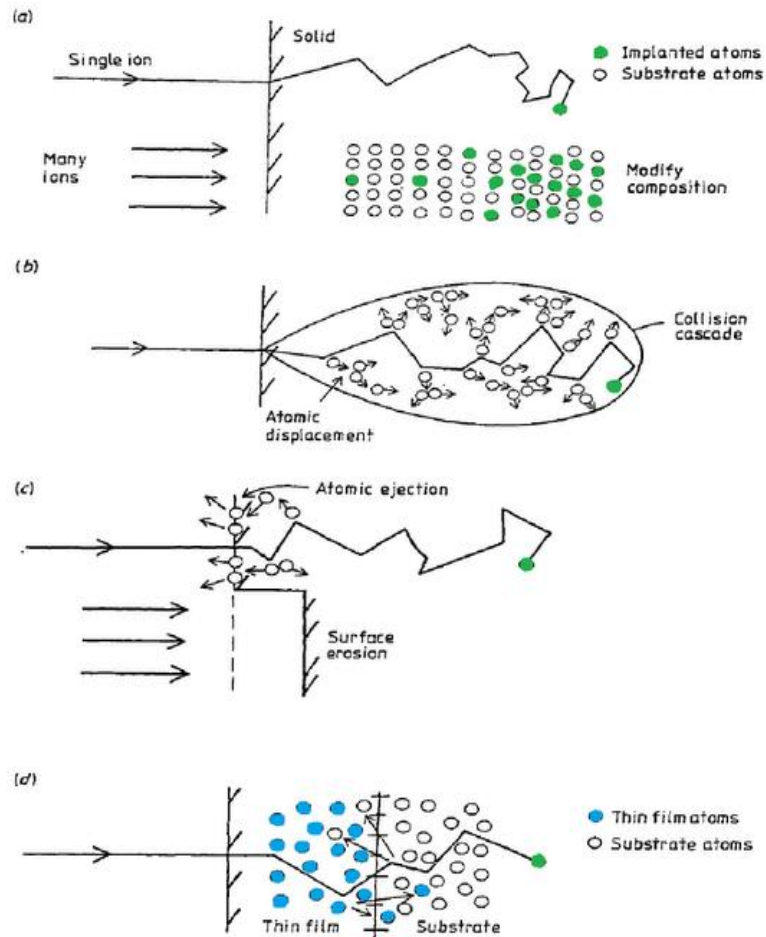


Fig 1.3: Basic materials modification processes (a) implantation; (b) damage; (c) sputtering; and (d) atomic mixing (adapted from Ref.[16]).

1.3 Ion penetration and Stopping

1.3.1 Energy loss processes

Charged particles penetrating inside a solid lose their energy through two main processes: (1) energy transfer to the atoms of the solid by elastic collisions, a process known as nuclear energy loss (S_n) and (2) energy transfer to the electrons by inelastic collisions, by exciting or ionizing the atom, a process known as electronic energy loss (S_e). In both the cases the interaction is basically coulomb type, for electronic case it is pure coulomb, while in nuclear case it is screened coulomb potential. The stopping cross section, $\varepsilon(E)$ describes the energy loss of an ion travelling through a target material per unit length ΔX so that [17]

$$\left(\frac{dE}{dX}\right)_{total} \approx \left(\frac{dE}{dX}\right)_{elec.} + \left(\frac{dE}{dX}\right)_{nuc.} = -N\varepsilon(E) \quad (1.1)$$

1.3.2 Stopping power

Ions backscattered from atoms beneath the surface will have less energy than those backscattered at the surface, due to electronic interactions. The rate of energy loss, dE/dx (referring to the projectile) is directly related to stopping power (referring to target material) and is basically the energy loss per unit depth the ion travels through the material. It is the property of the target material and also depends on ion projectile and its energy.

1.3.3 Nuclear energy loss

The Classical transfer of energy between projectile ion and stationary particle depends only on the mass and charge of the two particles and the moving particle's initial speed and direction. While the moving charge passes, the stationary particle recoils and absorbs energy. The moving particle is deflected. The final velocities and trajectories can be found out from the conservation of momentum and energy of the system. The kinematics is calculated from the atom-atom interatomic potentials [18]. When a particle of charge Z_1e , mass M_1 and velocity v hits another particle of charge Z_2e , mass M_2 then the equation which gives the nuclear energy loss on the basis of calculations is given by,

$$\left(-\frac{dE}{dX}\right)_{nuc.} = \left(\frac{4\pi Z_1^2 Z_2^2 e^4 N}{M_2 v^2}\right) * \left(\ln \frac{b_{max.}}{b_{min.}}\right) \quad (1.2)$$

where N is the number of target atoms per unit volume, b_{min} is minimum impact parameter and corresponds to the maximum energy transfer to a target atom in a head-on collision.

1.3.4 Electronic energy loss

It is prominent at velocities much greater than speed of electrons in their outer most orbits (i.e, for $v \gg v_0 Z_1^{2/3}$). At these velocities, charge $Z_1 e$ interacts elastically (inelastically) with free electrons (bound electrons) in the target. An energetic ion penetrates a solid, its trajectory is not affected by collisions with the light electrons and the collision lasts for such a short time that electron acquires an impulse without changing its position. To calculate the energy transfer during collision, electrons are considered at rest w.r.t. the projectile ions of energy \sim MeV/amu and moving with a velocity comparable to or more than Bohr velocity. There will be a net momentum transfer to the electron caused by the electric field of the incident ion at the position of the electron. A swift ion passing through the matter sees electrons at various distances from its path. The energy loss of incident ion per unit distance is calculated by multiplying the energy transfer with the differential cross section and integrates over all the impact parameters. Thus, the energy loss per unit distance i.e, the electronic energy loss is given by

$$\left(-\frac{dE}{dX}\right)_{electronic} = \left(\frac{4\pi Z_1^2 e^4 n}{m v^2}\right) * \left(\ln \frac{b_{max.}}{b_{min.}}\right) \quad (1.3)$$

where n is the number of electrons per unit volume.

1.3.5 Comparison of electronic and nuclear stopping

An energetic ion traverses into a solid; it gradually loses its energy in the material and comes to rest at some depth below the surface. The stopping is dominated by the nuclear energy loss for ion velocities **lower than** $v_0 Z_1^{2/3}$. In this energy range ions predominantly lose their energy due to Rutherford scattering. Due to collisions with the incident ions, target atoms are displaced from their original positions leading to subsequent nuclear collision cascade. The direct interaction between incoming ion and target atoms can lead to generation of defects, the amorphization of crystalline materials, and/or structural transformation in amorphous materials. Nuclear stopping is the origin of most sputtering at these low energies. At low

velocities, energy of ion is transferred from nucleus of projectile to target nucleus by electrostatic interaction (elastic collision) between the screened charges of the two nuclei. As suggested by Bohr and later developed by Lindhard et.al [19], S_n is normally the major component of energy loss at low energies, especially for heavy projectile atoms. Nuclear energy loss has two regimes, displacement followed by replacement collisions. At the entrance to surface, the ions dislodge atoms from lattice. Replacement collision occurs at the end of the ion range where the collision cascades are dominant. The nuclear energy loss is much smaller than the electronic energy loss for increasing projectile velocities and energies. The comparison of both the processes is described in figure 1.4, which illustrates the typical ratio between nuclear and electronic stopping powers. In comparison of equations (1.2) and (1.3), the major differences are the mass (m and M_2) in the denominator and the charge Z_2 of the target atom. For example, consider the case of protons, the ratio of nuclear to electronic energy loss per atom, by neglecting the ratio of log terms, is

$$\left(\frac{dE}{dX}\right)_{Nucl} / \left(\frac{dE}{dX}\right)_{elec} = [N (Z_2)^2 / M_2] (m/n) = (Z_2 / M_2) m = (1/3600), \quad (1.4)$$

where the number of electrons per unit volume $n \approx Z_2 N$; $M_2 \approx 2Z_2 m_p$; and $m_p \approx 1836m$ is the mass of proton.

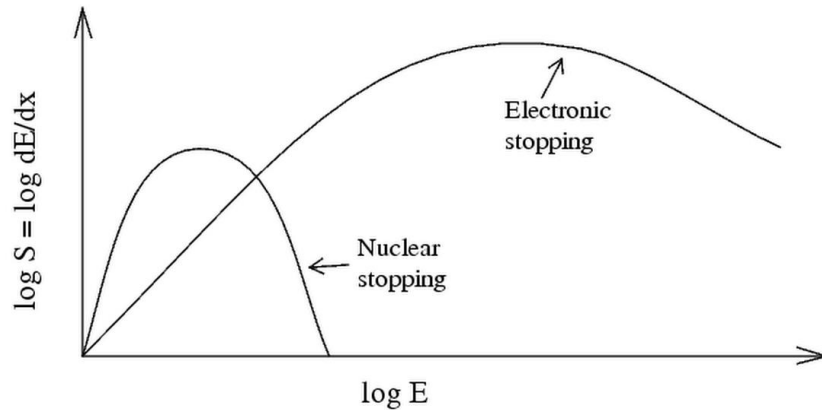


Fig 1.4. Relative magnitudes of nuclear and electronic stopping power. The maximum of the nuclear stopping curve typically occurs at energies between 10-100 keV and that of the electronic stopping power at MeV energies. For very light ions slowing down in heavy materials, the nuclear stopping is weaker than the electronic at all energies.

The nuclear collisions at higher energies usually occur as a sequence of independent binary collisions of atoms, between which the ion moves in an almost straight path where its energy loss is predominantly by electronic stopping. The electronic stopping is governed by inelastic collisions between the moving ion and the electrons in the target, which can be either bound or free. Many different physical processes contribute to the electronic stopping: ionization of the target atoms, excitation of electrons into the conduction band, collective electronic excitations such as plasmons, etc. Electronic stopping dominates at high ion energies. The transition between nuclear and electronic stopping depends on the ion mass. In case of a carbon target, it occurs at 100 keV for Ar ions and 1 MeV for Xe ions. For hydrogen ions (protons), electronic stopping always dominates.

1.3.6 Swift heavy ion irradiation and tracks

Due to the different mechanisms of conversion of electronic excitations into heat, the electronic structure of the target strongly affects the outcome of the ion impact. In metals, the electronic excitations are delocalized due to the presence of conduction electrons. This makes the excitations less likely to lead to atom motion, so that radiation damage comes mostly from knock-on atom displacements. In insulators e.g., diamond [20] or silica [21], above a

certain electronic energy deposition threshold [22] excitations may result in a strong heating of the lattice and damage by a cylindrical form of heat spikes [23]. To reach this deposition regime in heavy ion irradiation, higher energy is required (few tens of MeV or more). Hence the regime is called *swift heavy ion irradiation*. Swift heavy ions can give rise to so called *tracks*-amorphous regions that appear along the trajectory of the high energy ion. Normally the tracks are well aligned with respect to the beam directions and themselves can be viewed as nanostructures inside bulk materials. The track cores can be etched away and filled with some other material, which enables production of long straight nanowires [24]. The tracks may also have an internal structure, being under-dense in the center and over-dense in the surroundings, at least in silica.

1.3.7 Effective charge

The average charge of the ion, which depends on its velocity, is denoted as *effective* charge, Z_{eff} . Most importantly, when ions of arbitrary charge state are impinging on a solid surface, the actual charge state of ions in matter continuously fluctuates and is determined by the net difference of electron loss and electron capture. At high velocities, electron loss dominates, so that the ions become a bare nucleus with $Z_{\text{eff}} = Z_1$ at sufficiently high energy. In low energy regime atomic electrons interact with the electrons of the solid and then ion becomes almost neutral by vanishing effective charge due to electron pick up from the solid. Quantitatively, if the ion velocity is lower than the characteristic orbital velocity of its target atomic electrons then electron attachment to the projectile is effective. Under these conditions, electrons from the electron gas of the solid have sufficient time to adjust with the moving ion. At the end of range, ion velocities are very low which starts interacting with target atoms thereby dislodging atoms from regular lattice sites.

1.4 Swift heavy ion induced effects in materials

1.4.1 Thermal spike

SHI irradiation is known for depositions of high density of energy to electrons along the ion path within very short intervals of time. According to the thermal spike model [25] during the passage of swift heavy ions, the kinetic energy of the electrons is transported

to target lattices via electron-electron or electron-phonon interaction causing sufficient increase of local lattice temperature above the melting point of the material. The temperature increase is followed by a thermal quenching at an extremely high quenching rate at these quenching rates; pre-existing defects in semiconductors can be annealed out. In this initial stage of collision cascade, the system is not thermodynamic at all since the atomic motion occurs much faster than the thermodynamic relaxation time scale of atoms which is of the order of 100 fs or more. Once the ion has lost enough energy, or if several recoils happen to occur close to each other, numerous collisions may occur in close vicinity of each other. In this case, the binary collision concept does not work anymore, but the cascade becomes a complex many-body phenomenon, which leads to the complete breakup of the lattice. Due to the high kinetic energy of the recoils, the region of overlapping collisions can be considered to be *hot* [26-29] and is hence called a *heat spike* or *thermal spike*. In bulk materials, this hot region cools down rapidly due to heat conduction to the surrounding lattice. Heat spikes can become important for heavy projectiles in dense materials.

1.4.2 Coulomb explosion

In this case, an incident energetic ion excites the electron cloud producing charge separation along its path through the solid which results in repulsion between the transiently ionized atoms in the solid causing *Coulomb explosion* [30]. Such transiently ionized region produced by an incident ion is known as an *ionization track* which can produce craters [31] and sputtering [32-34], as well as damage tracks in solids [35, 36]. Coulomb explosion model and the thermal spike model are used to describe defect production in insulators and semiconductors [37]. It is somewhat remarkable since Coulomb explosion is a mechanism for coupling of the electronic excitation energy into atomic motion, whereas a thermal spike model describes the transport of energy out of a heated region. Mostly, thermal spike model is used to interpret the observed effects in semiconductors and coulomb explosion model is being used to explain the observed effects in insulators. However, it is observed that these interaction processes compete with each other in all the materials. Even in insulators, within short intervals of time and few nms after entering the target, enough electrons are generated to screen out the projectile charge resulting in transition from coulomb explosion to thermal spike situation.

1.5 Materials of interest

1.5.1 Introduction to nanoscience and nanotechnology

The word “nano” from which this relatively new field derives its name is a prefix denoting a scale of 10^{-9} . Nano comes from the Greek word “nanos” meaning “dwarf”. Properties of materials of nanometric dimensions are significantly different from those of atoms and bulk materials. They effectively form a bridge between bulk materials and their atomic or molecular counterparts. Nanoscience is the study of the properties and phenomena associated with nanoscale materials. The suitable control of the properties of nanometer scale structures can lead to new sciences as well as new devices and technologies. Nanotechnology is the application of nanoscience, especially to industrial and commercial objectives. The underlying theme of nanotechnology is miniaturization. Bulk materials have physical properties regardless of size, but at the nanoscale, size-dependent properties are often observed. Thus, the properties of materials change as their size approaches the nanoscale and as the percentage of atoms at the surface becomes significant. For materials larger than one micrometer in size, the percentage of atoms at the surface is insignificant in relation to the number of atoms in the bulk of the material. The interesting and sometimes unexpected properties of nanoparticles are therefore largely due to the large surface area of the material, which dominates the contributions made by the small bulk of the material. An excellent example of this is the absorption of solar radiation in photovoltaic cells, which is much higher in materials composed of nanoparticles than it is in thin films of continuous sheets of material [38].

In the present day technology the semiconductor nanocrystals (Si and Ge) are important materials in semiconductor processing and devices [39]. Nanocrystals (NCs) of Si and Ge embedded in a gate dielectric (like SiO_2 or HfO_2) have important role in electronic, photonic and photovoltaic industries [40-42]. Generally, the modification of these materials plays a vital role in tuning their properties for various applications. In particular, swift ion irradiation is established to be one of the versatile techniques for the modification of materials at nanoscale. The aim of this thesis is to report the work on synthesis of semiconducting (Si and Ge) NCs and to investigate the Swift Heavy Ion (SHI) irradiation induced modification of these synthesized NCs. The electronic energy loss and fluence dependence studies were carried out

in tailoring the size and shape of the NCs. The effects of SHI track radius on the size and shape of the embedded NCs has been studied. Ion beam shaping of metallic NCs for various applications have been reported in the literature for Co [43] and Ag [44] NCs embedded in silica glass and for Au [45-47] and Pt [48] NCs embedded in thermally grown SiO₂ on Si substrates.

1.5.2 Ion irradiation effects on Ge and Si NCs

Coming to the effects of SHI irradiation on the already existing NCs, Schmidt et.al [49,50] reported that Ge NCs were flattened into an oblate shape when 38 MeV iodine ion beam was used to irradiate various sizes of Ge NCs embedded in SiO₂. It was shown that the medium-sized nanospheres became oblates and smaller ones shape into rod-like structures whereas large Ge nanospheres remain spherical under the same irradiation energy and fluences. On the other hand, Antonova et.al [51] more recently reported the formation of small Ge NCs and the modification of existing Ge NCs in the SiO₂ matrix by 480 MeV Xe ion irradiation followed by a post-annealing process. They demonstrated the ability of ion irradiation to modify and/or create new Ge NCs in Ge:SiO₂ films with variable Ge composition. A high concentration of Ge NCs with a size of 265 nm was observed in the irradiated and subsequently annealed (at 500 °C) films, while the relatively large Ge NCs of 8-15 nm were formed without ion irradiation. Araujo et.al [52], have shown that crystalline Ge NPs are easily amorphized by SHI irradiation, while bulk c-Ge is not. Moreover, the amorphization occurs at lower fluences for the higher SHI irradiation energy, indicating that electronic energy loss is the dominant process. They have observed Ge NP elongation at fluences higher than those required for amorphization. The combination of initial NP size and SHI irradiation S_e determines the fluence required for shape change and the direction of elongation. There are also some reports on phase separation of GeO_x into Ge NCs and GeO₂ by heavy ion irradiation [53, 54].

There are not many detailed reports available concerning ion beam shaping of Si NCs in an amorphous matrix. Saxena et.al [55, 56] have reported that size of Si NCs decreases from 29 nm to 10 nm under 120 MeV Ni ions irradiation at a fluence 1×10^{14} ions per cm². The reason for the reduction in size was explained by combining spinodal decomposition phenomena and thermal spike model. Chaudhari et.al [57, 58], have observed the growth of Si NCs by ion

irradiation and with the increase in fluence of incident ion NC size was increased, whereas the as deposited sample (amorphous) shows no NCs.

However, up to now there are no consistent experiments in describing swift heavy ion shaping of semiconducting NCs (Ex. Ge, Si). Therefore, one of the goals of the present thesis is also to investigate the irradiation induced effects on size and shape of semiconducting (Si and Ge) NCs. In our studies, the as-deposited, annealed and irradiated samples were characterized by different techniques such as RBS, XRD, Raman, FESEM, TEM and AFM for compositional, structural, optical, luminescence and surface morphology studies respectively to understand the growth and physics of ion beam interaction with semiconductor NCs.

We have synthesized Ge NCs in SiO₂ matrix by RF co-sputtering, followed by Rapid Thermal Annealing (RTA) at 700°C and 800°C. We have used these annealed samples to study the effects of heavy ion irradiation (120 MeV Ag and 80 MeV Ni at different fluences) on the Ge NCs. We have also synthesized Ge NCs embedded in HfO₂ by using RF sputtering and subsequent RTA or heavy ion irradiation [59]. GeO₂ nanocrystal (NC) thin films were deposited on Si substrate using the magnetron sputtering method and irradiated with swift heavy ions of 80 MeV Ni at various fluences ranging from 5×10^{12} to 1×10^{14} ions/cm² [60]. The formation of Ge NCs in the ion-irradiated GeO₂ NC thin films has been understood on the basis of irradiation-induced separation of oxygen from GeO₂ NCs. Finally we have studied the effects of SHI irradiation on the Si nanoparticles synthesized by laser ablation.

1.6 Synthesis Methods

The general method of synthesis of Ge NCs involves the deposition of thin films of Ge by an established physical deposition process and followed by high temperature annealing. There are several established methods for the synthesis Ge NCs embedded in SiO₂ such as atom beam sputtering [61], molecular beam epitaxy [62], chemical vapor deposition [63] and ion implantation [64] followed by high temperature annealing. Rapid thermal annealing (RTA) among various annealing processes has advantages in reducing unwanted diffusion during annealing and minimizes the interaction between film and substrate due to faster timing [61]. Radio frequency magnetron sputtering (RFMS) is a suitable technique for deposition of

composite thin films. The sputtering technique plays an interesting role in the development of materials for various applications. The materials studied in this thesis have been fabricated by RFMS. We have also synthesized Ge NCs in SiO₂ by low energy implantation of Ge⁺ ions into SiO₂ and followed by high temperature annealing. The Si nanoparticles samples have been synthesized by laser ablation of Si wafer in Acetone.

1.6.1 RF Magnetron Sputtering

Sputtering is extensively used in the semiconductor industry to deposit thin films of various materials in integrated circuits processing. Thin anti-reflection coatings on glass, planar waveguides which are useful for photonic applications are deposited by using sputtering. This technique is also used to fabricate thin film sensors, photovoltaic thin films (solar cells), metal cantilevers and interconnects etc. More details about sputtering technique for the synthesis of the samples used in this dissertation can be found in the next chapter.

1.7 Structure and organization of the thesis

Present *chapter* describes the motivation and aim of the present thesis particularly the methods of synthesis, and the choice of materials, the basics and relevant literature, ion-solid interactions and characterization techniques.

Next *chapter* is devoted to the discussion of the details of various experimental techniques that were carried out in these investigations.

Chapter 3 describes the results on the synthesis and characterization of Ge NCs embedded in SiO₂ and the ion irradiation effects on thus synthesized Ge NCs. The Ge NCs embedded in SiO₂ matrix have been synthesized using RF magnetron co-sputtering technique followed by RTA at 700 and 800°C. The Ge NCs samples obtained by annealing at 800°C were irradiated by 120 MeV Ag and 80 MeV Ni ions with various fluences to study the effects of dense ionization on the size and shape of the Ge NCs. The modifications in the structure of the embedded Ge NCs due to the energy deposited by incident ions at various irradiation fluences have been explained on the basis of energy deposited by incident ion inside, both the SiO₂ and embedded Ge NCs. This chapter also includes the results of the

synthesis of Ge NCs in SiO₂ matrix by first low energy Ge implantation into SiO₂ and then followed by high temperature annealing at 700°C and 800°C.

Chapter 4 presents the results of the synthesis and characterization of Ge NCs embedded in HfO₂ by RF sputtering and followed by RTA and SHI irradiation. Tri-layered HfO₂/Ge/HfO₂ thin films were fabricated on Si substrate at room temperature by RF magnetron sputtering of HfO₂ and Ge targets and then the as-deposited samples were annealed by rapid thermal annealing process at 700 and 800°C in order to synthesize the Ge NCs in HfO₂ dielectric matrix. XRD and micro-Raman spectroscopy measurements were carried out to confirm the formation of Ge NCs in the post-annealed samples. On the other hand, the as-deposited samples were also irradiated with swift heavy ions of 150 MeV Au and 80 MeV Ni at a fluence of 3×10^{13} ions/cm² as an alternative approach to induce the formation of Ge NCs through ion beam irradiation. The structural characteristics of NCs in the ion-irradiated samples have been compared with the ones obtained by RTA process.

Chapter 5 reports the results on synthesis and characterization of GeO₂ NCs thin films by using RF sputtering method and the effects of 80 MeV Ni ions at various fluences ranging from 5×10^{12} to 1×10^{14} ions/cm². Grazing incidence XRD measurements demonstrate a decrease in average size of NCs with increase in fluence of ion irradiation. Micro-Raman spectroscopy studies show clearly the formation of Ge NCs with the increase of irradiation fluence. FESEM was employed to study the morphology and modifications in NCs due to ion irradiation. TEM measurements of the ion-irradiated sample at 1×10^{14} ions/cm² confirmed the presence of few nm-sized Ge NCs, which were not observed in as-deposited sample. The overall results suggest that GeO₂ NCs are reduced in size and few of them are converted into Ge NCs due to the effects of electronic energy deposition by the irradiating ions. This formation of Ge NCs in the ion-irradiated GeO₂ NC thin films has been understood on the basis of irradiation-induced separation of oxygen from GeO₂ NCs.

In the **Chapter 6** we have presented the results on the effects of 150 MeV Au ions irradiation on Si nanoparticles (NPs) synthesized by picosecond laser ablation of single crystal Si wafers in acetone. The formation of Si NPs was confirmed by Raman spectroscopy, TEM and FESEM measurements. The size distribution of thus synthesized NPs was found to be in the range from very few nm to 80 nm. These samples were then irradiated with 150

MeV Au ions at various fluences ranging from 1×10^{13} to 1×10^{14} ions/cm². The effects of ion irradiation on size and shape of Si NPs were studied again by using TEM, FESEM and micro Raman spectroscopy. The results thus obtained are compared with those for pristine samples and the effects of 150 MeV Au ions irradiation have been discussed in this chapter using the theoretical models for ion-solid interaction.

Chapter 7 summarizes the results obtained in these investigations. Future outlook, perspectives and possible subsequent direction of these investigations that can be carried out, are discussed in detail.

1.8 References:

1. A V Krasheninnikov and K Nordlund J. Appl. Phys. 107, (2010) 071301.
2. J S Williams Rep. Prog. Phys. 49 (1986) 491.
3. A V Krasheninnikov and F. Banhart Nature Materials 6, (2007) 723.
4. Swift Heavy Ions for Materials Engineering and Nanostructuring Springer Series in Materials Science Vol. 145, (2011) 1-46 by D K Avasthi and G K Mehta.
5. A Colli, A Fasoli, C Ronning, S Pisana, S Piscanec, and A C Ferrari, Nano Lett. 8, (2008) 2188.
6. L F Zagonel, C A Figueroa, F Alvarez Surface and Coatings Technology 200, (2005) 2566.
7. B Peng, M Locascio, P Zapol, S Li, S L Mielke, G C Schatz, and H D Espinosa, Nat. Nanotechnol. 3, (2008) 626.
8. M S Raghuveer, P G Ganesan, J DøArcy-Gall, G Ramanath, M Marshall, and I Petrov, Appl. Phys. Lett. 84, (2004) 4484.
9. H Bernas, J-P Attané, K-H Heinig, D Halley, D Ravelosona, A Marty, P Auric, C Chappert, and Y Samson, Phys. Rev. Lett. 91, (2003) 077203.
10. S M Sze, Physics of Semiconductor Devices (Wiley-Interscience, 1969)
11. H Kaur, G Pujari, M K Semwal, A Sarma and D K Avasthi òIn vitro studies on radiosensitization effect of glucose capped gold nanoparticles in photon and ion irradiation of HeLa cellsö Nucl. Inst. and Meth. in Phys. Res. B 301 (2013) 7.
12. I P Jain, G Agarwal Surface Science Reports 66 (2011) 77.
13. Chan W L and Chason E J. Appl. Phys. 101 (2007) 12130.

14. K H Heinig, T Muller, B Schmidt, M Strobel, and W Möller, Appl. Phys. A: Mater. Sci. Process. 77, (2003) 17.
15. S Dhara, Crit. Rev. Solid State Mater. Sci. 32, (2007) 1.
16. M Nastasi, J Mayer, and J Hirvonen, Ion-Solid Interactions-Fundamentals and Applications Cambridge University Press, cambridge, (1996).
17. L C Feldman and J W Mayer öFundamentals of Surface and thin film analysisö Elsevier Science Publishers
18. W K Chu, J W Mayer, M A Nicolet öBack Scattering Spectrometryö Academic Press 1978.
19. J Lindhard: Mat. Fys. Medd. Dan. Vid. Selsk., 34 (1965) 14.
20. J Krauser, J Zollondz, A Weidinger, and C Trautmann, J. Appl. Phys. 94, (2003) 1959.
21. S Klaumünzer, Nucl. Instrum. Methods Phys. Res. B 244, (2006) 1.
22. D Kanjijal, Curr. Sci. 80, (2001) 1560.
23. C Trautmann, S Klaumünzer, and H Trinkaus, Phys. Rev. Lett. 85, (2000) 648.
24. P Kluth, C S Schnohr, O H Pakarinen, F Djurabekova, D J Sprouster, R Giulian, M C Ridgway, A P Byrne, C Trautmann, D J Cookson, K Nordlund, and M Toulemonde, Phys. Rev. Lett. 101, (2008) 175503.
25. A Meftah, F Brisard, J M Costantini, E Dooryhee, M Hage-Ali, M Hervieu, J P Stoquert, F Studer, and M Toulemonde, Phys. Rev. B 49, (1994) 12457.
26. T Diaz de la Rubia, R S Averback, R Benedek, and W E King, Phys. Rev. Lett. 59, (1987) 1930; 60, (1988) 76(E).
27. S E Donnelly and R C Birtcher, Phys. Rev. B 56, (1997) 13599.

28. A Meldrum, S J Zinkle, L A Boatner, and R C Ewing, *Nature London* 395, (1998) 56.
29. A E Stuchbery and E Bezakova, *Phys. Rev. Lett.* 82, (1999) 3637.
30. R M Papaléo, L D de Oliveira, L S Farenzena, M A de Araújo, and R P Livi, *Phys. Rev. B* 62, 11 273 (2000)
31. R E Johnson and W L Brown, *Nucl. Instrum. Methods Phys. Res.* 198, 103 (1982)
32. P K Haff, *Appl. Phys. Lett.* 29, 443 (1976)
33. T Schenkel, A V Hamza, A V Barnes, D H Schneider, J C Banks, and B L Doyle, *Phys. Rev. Lett.* 81, 2590 (1998)
34. D Lesueur and A Dunlop, *Radiat. Eff. Defects Solids* 126, 123 (1993); 126, 163 (1993)
35. K Izui, *J. Phys. Soc. Jpn.* 20, 915 (1965)
36. F Seitz, *Discuss. Faraday Soc.* 5, 271 (1949)
37. H P Maruska and J Tietjen, *J. Appl. Phys. Lett.* 15, 327 (1969)
38. M. Stupca, M. Alsalhi, T. Al Saud, A. Almuhanha, and M. H. Nayfeh, *Appl. Phys. Lett.*, 91, 063107 (2007).
39. δ Si and Ge nanocrystals for future memory devicesö C. Bonafosa, Carradaa, G. Benassayag, S Schamm-Chardon, J Groenen, V Paillard, B Pecassou, A Claverie, P Dimitrakis, E Kapetanakis, V Ioannou-Sougleridis, P Normand, B Sahu, A Slaoui *Materials Science in Semiconductor Processing* 15 (2012) 615.
40. Conibeer G et al, *Silicon nanostructures for third generation photovoltaic solar cells Thin Solid Films* 511/512, (2006) 654.
41. Choi K, Chim W K, Heng C L, Teo L W, Ho V, Ng V, Antoniadis D A and Fitzgerald E A *Appl. Phys. Lett.* 80 (2002) 2014.

- Maeda Y, Tsukamoto N, Yazawa Y, Kanemitsu Y and Masumoto Y Appl. Phys. Lett. 59 (1991) 3168.
42. Cullis A G, Canham L T and Calcott P D J J. Appl. Phys. 82 (1997) 909.
- L Pavesi, L Dal Negro, C Mazzoleni, G Franzò & F Priolo Nature 408 (2000) 440.
43. C D Orleans, J P Stoquert, C Estournes, C Cerruti, J J Grob, J L Guille, F Haas, D Muller and M Richard-Plouet Phys. Rev. B 67 (2003) 220101(R).
44. A Oliver, J A Reyes-Esqueda, J C Cheang-Wong, C E Román-Velázquez, A Crespo-Sosa, L Rodríguez-Fernández, J A Seman, and Cecilia Noguez Phys. Rev. B 74 (2006) 245425.
45. S Roorda, T V Dillen, A Polman, C Graf, A V Blaaderen and B J Kooi Adv. Mater. 16 (2004) 235.
46. J J Penninkhof, T van Dillen, S Roorda, C Graf, A van Blaaderen, A M Vredenberg, A Polman Nucl. Instr. and Meth. B 242 (2006) 523.
47. K Awazu, X Wang, M Fujimaki, J Tominaga, H Aiba, Y Ohki and T Komatsubara Phys. Rev. B 78 (2008) 054102.
48. R Giulian, P Kluth, L L Araujo, D J Sprouster, A P Byrne, D J Cookson and M C Ridgway Phys. Rev. B 78 (2008) 125413.
49. B Schmidt, K H Heinig, A Mücklich, C Akhmadaliev Nucl. Instrum. Methods Phys. Res. B 267 (2009) 1345.
50. B Schmidt, A Mücklich, L Rontzsch, K H Heinig Nucl. Instrum. Methods Phys. Res. B 257 (2007) 30.
51. I V Antonova, V A Skuratov, V A Volodin, S A Smagulova, D M Marin, A Janse van Vuuren, J Neethling, J Jedrzejewski and I Balberg J. Phys. D: Appl. Phys. 45 (2012) 285302.

52. L L Araujo, R Giulian, D J Sprouster, C S Schnohr, D J Llewellyn, B Johannessen, A P Byrne and M C Ridgway Phys. Rev. B 85, (2012) 235417.
53. Y Batra, D Kabiraj, S Kumar and D Kanjilal, Surface Coatings and Tech. 203 (2009) 2415. & J. Phys. D: Appl. Phys. 40 (2007) 4568
54. K Vijayarangamuthu, S Rath, D Kabiraj, D K Avasthi, P K Kulriya, V N Singh and B R Mehta, J. Vac. Sci. Technol. A 27 (2009) 731.
55. N Saxena, A Agarwal, D M Phase, R J Choudhary, D Kanjilal Physica E 42, 2190 (2010)
56. N Saxena, A Agarwal, D Kanjilal Nucl. Inst. and Meth. In Phys Res B 269, (2011) 3233.
57. P S Chaudhari, T M Bhawe, R Pasricha, F Singh, D Kanjilal and S V Bhoraskar Nucl. Inst. and Meth. In Phys Res B 239 (2005) 185.
58. P S Chaudhari, T M Bhawe, D Kanjilal and S V Bhaoraskar, J. Appl. Phys. 93 (2003) 3486.
59. Ion beam irradiation effects on Ge nanocrystals synthesized by using RF sputtering followed by RTA V Saikiran, N Srinivasa Rao, G Devaraju, G S Chang and AP Pathak (in press Nucl. Inst. Meth B 2013).
60. Formation of Ge nanocrystals from ion-irradiated GeO₂ nanocrystals by swift Ni ion beam V Saikiran, N Srinivasa Rao, G Devaraju, G S Chang and A P Pathak (Submitted to NIMB).
61. N Srinivasa Rao, A P Pathak, G Devaraju, V Saikiran, et.al, Solid State Communications 150, (2010) 2122.
62. Eyeru A, Leifeld O, Muller E, Stutz S, Sigg H and Grutzmacher D Thin Solid Films 380, (2000) 246

63. F Boscherini, G Capellini, L Di Gaspare, M De Seta, F Rosei, A Sgarlata, N Motta and S Mobilio Thin Solid Films 380, (2000) 173.
64. U V Desnicaa, M Buljana, P Dubceka, Z Siketica, I Bogdanovic Radovica, S Bernstorffb, U Serincanc, R Turanc Nucl. Inst. and Meth. In Res. B 249, (2006) 843.

Chapter 2

Experimental Methods

2.1 Introduction

This chapter gives all the details of experimental methods that have been used for sample preparation, subsequent treatment (annealing / heavy ion irradiation) and characterization. The in-house available RF magnetron sputtering facility was effectively used to grow the Ge+SiO₂, GeO₂, HfO₂/Ge/HfO₂ thin films. The Ge implantation into SiO₂ was done at Indira Gandhi Centre for Atomic Research (IGCAR), Kalpakkam. High energy irradiation work has been carried out at Inter University Accelerator Center (IUAC), New Delhi. Pristine, annealed and heavy ion irradiated samples have been characterized by various in house characterization techniques such as X-ray Diffraction (XRD), Micro-Raman spectroscopy, Atomic Force Microscopy (AFM), Field Emission Scanning Electron Microscopy (FESEM) and Transmission Electron Microscopy (TEM). Rutherford Backscattering Spectrometry (RBS) facilities available at IGCAR, Kalpakkam and IUAC, New Delhi have been used to estimate the composition in the as deposited composite thin films. The detailed description of the facilities and their usage is given in this chapter.

2.2 Samples Growth methods

The various samples used for the investigations in this thesis have been grown using the following techniques.

1. Radio Frequency Magnetron Sputtering
2. Ion Implantation
3. Laser ablation

The details of the samples are given briefly in table 2.1.

Table 2.1: Description of the samples

S. No	Sample details	Post-deposition treatment	Irradiation details	Characterizations used
1	Ge NCs embedded in SiO ₂ [Ge + SiO ₂]	RTA 700 & 800°C	80 MeV Ni (1E13, 3E13 & 1E14 ions/cm ²) 120 MeV Ag (1E13 & 3E13 ions/cm ²)	RBS, XRD, Raman, TEM
2	Ge + SiO ₂ by 1 MeV Ge implantation into SiO ₂ (1E16 to 1E17 ions/cm ²)	RTA @ 700 & 800°C	---	RBS, XRD, Raman
3	GeO ₂ NCs	-----	80 MeV Ni (5E12, 1E13, 2E13, 5E13 & 1E14 ions/cm ²)	RBS, XRD, Raman, AFM, FESEM, TEM
4	Ge NCs embedded in HfO ₂ [HfO ₂ /Ge/HfO ₂]	RTA 700 & 800°C and 150 MeV Au & 80 MeV Ni irradiation (3E13 ions/cm ²)	-----	RBS, XRD, Raman
5	Si NCs by picosecond laser ablation	-----	150 MeV Au (1E13, 3E13 & 1E14 ions/cm ²)	Raman, FESEM, TEM

2.3 Radio Frequency Magnetron Sputtering (RF sputtering)

The thin films described in this dissertation work were prepared using a process called RF sputtering deposition method. Sputtering is extensively used in the semiconductor industry to deposit thin films of various materials in integrated circuits processing. The thin anti-reflection coatings on glass which are useful for optical applications are normally deposited by sputtering. Because of the low substrate temperature used, sputtering is an ideal method to deposit contact metals for thin film transistors. This technique is also used to fabricate thin film sensors, photovoltaic thin films (solar cells), metal cantilevers and interconnects, etc. With the use of multi target facility, it is easier to fabricate multilayer structures of different dielectric materials. In the present work, we have demonstrated that radio frequency magnetron sputtering technique is a suitable technique for the deposition of thin films of Ge nanocrystals embedded in dielectric matrix and it is a cheap and versatile technique to deposit alternating layers of different materials with controlled thickness.

Sputter deposition is a physical vapour deposition process for depositing thin films. Sputtering means ejection of material from a target and depositing it on a substrate such as a silicon wafer/glass/quartz. The target is the source material. Targets and substrates are placed in a vacuum chamber and the chamber is pumped down to a prescribed pressure. Sputtering starts when a negative voltage is applied to the target causing a plasma or glow discharge. Positively charged gas ions generated in the plasma region are attracted to the negatively biased target plate at a very high speed. This collision creates a momentum transfer and ejects atomic size particles from the target. These particles are deposited as a thin film onto the surface of the substrate.

Sputtering can be done either in DC or RF modes. DC sputtering is done with conducting materials. If the target is a nonconducting material, the positive charge will build up on the material and it will stop sputtering. RF sputtering can be done for both conducting and nonconducting materials. This technology uses powerful magnets to confine the glow discharge plasma to the region closest to the target plate. That vastly improves the deposition rate by maintaining a higher density of ions, which makes the electron/gas molecule collision process much more efficient.

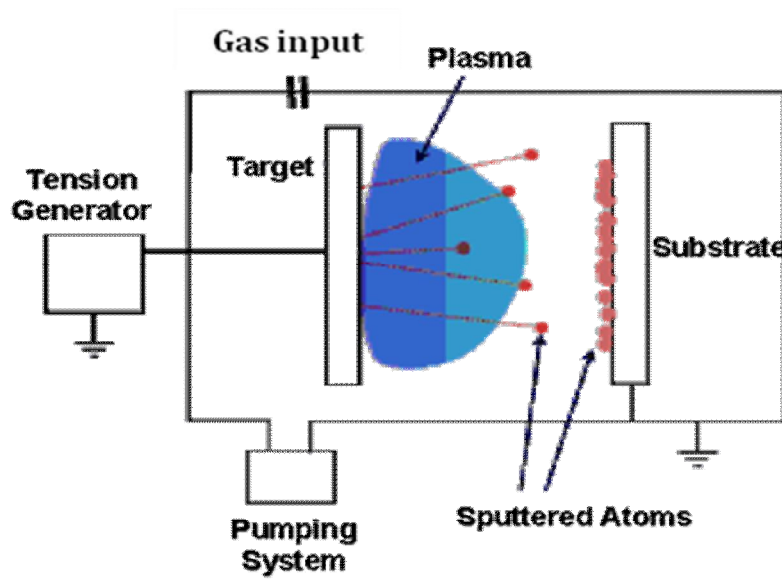


Fig 2.1: Schematic diagram for RF sputtering process.

A Radio Frequency magnetron sputtering (RFMS) system consists of a vacuum chamber, a target (cathode) and a substrate holder (anode) as shown in Figure 2.1. A radio frequency oscillating voltage is applied between the target and substrate. During the sputtering process plasma is created in the chamber and ions (Argon ions in the present case) out of plasma are accelerated towards a target consisting of the material to be deposited. Material is detached (sputtered) from the target and afterwards deposited on a substrate in the vicinity. The process is realized in a closed chamber, which is pumped down to a vacuum base pressure before deposition starts.

2.3.1 Sputtering Yield

The sputter yield S is defined as the mean number of atoms removed from the surface of a material (target) per incident ion. The sputtering yield is dependent on the following parameters.

- i) Density of target material
- ii) Energy of incident ion
- iii) Incident angle of ions

- iv) Crystal structure of target surface

Sputtering is classified into different types depending on the nature of target material (conducting, semiconducting or insulating); process used for ionization of the sputtering gas single or mixed gas sputtering atmosphere and the number of layers or elemental components in the thin films.

2.4 Accelerator facilities

2.4.1 Pelletron details

Swift heavy ion irradiation work has been carried out using 15MV tandem accelerator facility available at IUAC, New Delhi [1]. This pelletron is a heavy ion tandem type of electrostatic accelerator. The ion source produces negative ions which are pre-accelerated to ~300 keV and then injected into an accelerator tank filled in with SF₆ (insulating gas). At the centre of the tank, a terminal shell is maintained at a high voltage (~15 MV). Inside the terminal, a stripper uses a gas (usually N₂ or Ar) or a thin carbon which, upon collision removes electrons from the incoming negative ions. Then the positively charged ions experience a second boost of acceleration (thus the name "tandem" accelerator) as they exit the terminal and travel down the acceleration tube to ground at the high- energy end of the machine (Fig.2.2). The primary benefits of the tandem configuration are:

- a) The final beam energy is approximately $(q+1)$ times the terminal voltage, where q is the charge state to which the ions are stripped in the terminal.
- b) Upon exiting from the tank, the ions are bent into horizontal plane by analyzing magnet, which selects a particular type of beam. The switching magnet diverts the high energy ion beams into various beam lines into different experimental areas of the beam hall.

The entire machine is computer controlled and is operated from a separate control room.

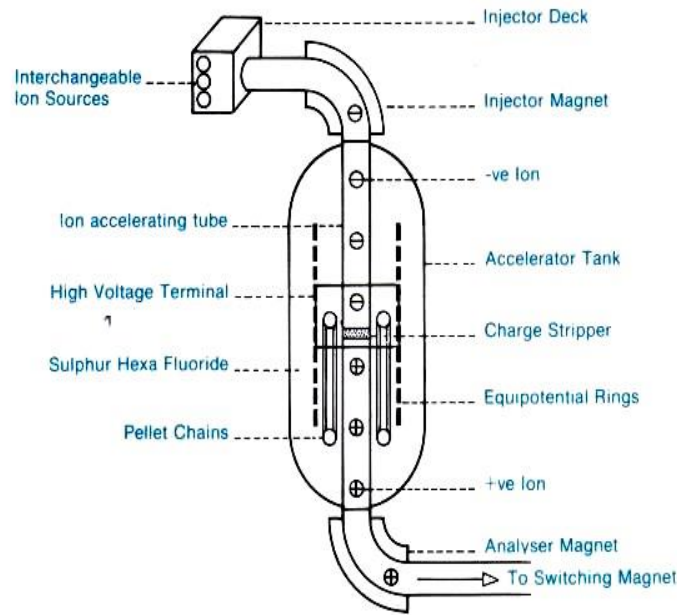


Fig 2.2: Schematic of 15MV pelletron accelerator

All the Irradiation experiments have been performed in high vacuum irradiation chamber as shown in Fig.2.3. We have used 150 MeV Au, 120 MeV Ag and 80 MeV Ni ions at various fluences such as 5×10^{12} , 1×10^{13} , 2×10^{13} , 3×10^{13} , 5×10^{13} and 1×10^{14} ions/cm². Necessary precautions were taken during irradiation to minimize heating of samples and channeling of ions by maintaining low beam currents and orienting samples to 5° with respect to beam axis, respectively.

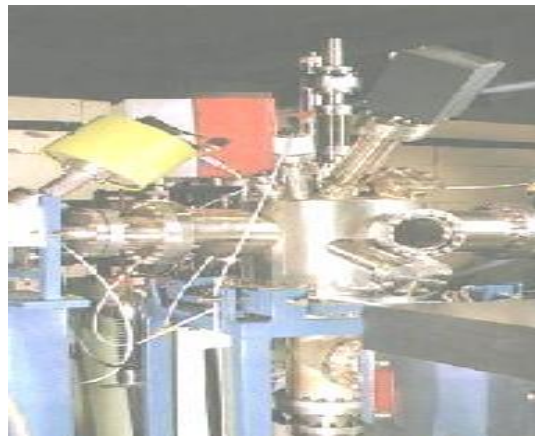


Fig 2.3: Materials science high vacuum irradiation chamber

2.4.2 Tandem accelerator at IGCAR

Ion beam characterization work presented in this thesis has been carried out using the RBS facility at IGCAR, Kalpakkam. The tandem accelerator has dual source (i) Duo-plasmatron (for H and He ions) and (ii) SNICS (Source of Negative Ions by Cesium Sputtering for almost all other elements in the periodic table. The terminal potential can be varied between 0.1 and 1.7MV (see Fig.2.4) to vary the energy of the projectile ions. The central feature of the Tandetron concept is a state-of-the-art and SF₆ insulated parallel fed Cockcroft-Walton type HV power supply characterized by high reliability, extremely low noise level, high voltage stability and low ripple. A high RF driving frequency, special RC-filtering and feedback circuits eliminate hum, drift and jitter provide a high terminal voltage stability and low terminal voltage ripple without the need for slit stabilization.

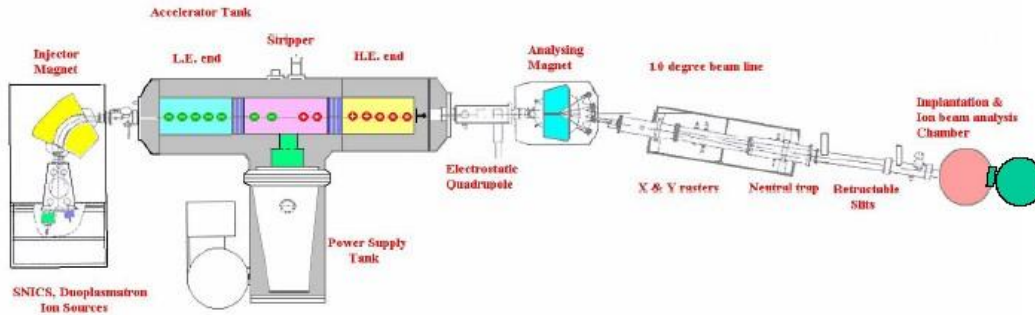


Fig 2.4: Schematic of 1.7MV tandetron accelerator

As a result there are no vibrations, which might result in terminal voltage fluctuations. Also, the ripple and stability values and dynamic behaviour are stable over many years of operation. A Generating Voltmeter (GVM) is used for measuring the terminal voltage. Stripper gas (N₂) at 7 kg/cm² is provided in the high voltage terminal by means of a plastic tube running through the column from outside the pressure tank to a metering valve feeding the gas to the stripper canal. The plastic tube is of sufficient length to withstand the high voltage. It is kept as a coil mounted inside a teflon tube. A turbo molecular pump is provided in the terminal to pump out and re-circulate the stripper gas so as to maintain a gas pressure of 50–100 microns in the stripper canal and 10⁻⁷ mbar in the accelerating tubes. The negative ions accelerated in the lower energy side are made positive by stripping of the electrons with N₂ gas. They are further accelerated by the high energy accelerating tube.

We have used this tandem accelerator facility for ion beam analysis (Rutherford Backscattering Spectroscopy) and for Ge ion implantation into SiO₂ (1 MeV Ge⁺ ions).

2.4.2.1 Duoplasmatron ion Source

This source can provide H⁺ and He⁺ ions. Positive ion beam from the duoplasmatron ion source is accelerated by anode voltage of 100V into a charge exchange canal. Lithium vapour introduced into the charge exchange canal converts 1-2% of the positive ions to negative ions. The negative ion beam is pre-accelerated by a gap lens to 10-20 keV and focused at the entrance of the 90° mass analysing magnet.

2.4.2.2 Negative sputter ion source

This source (SNICS) can provide ions of almost all elements, which can form negative ions. The target material in solid form, necessary for producing the ion beam, is packed in a copper target holder and mounted in the source and 3 to 10 kV voltage is applied. Cesium ions, produced by thermal ionization of Cesium vapour sputter the target material. The sputtered atoms pass through a thin layer of Cesium on the target and negative ions are produced. They are pre-accelerated to 20 to 30 keV and focused at the entrance of the 90° mass analyzing magnet.

2.4.3 RBS facility

The setup at IGCAR has some major parts which have been discussed elsewhere [2]. The RBS facility has been automated using virtual instrument automation software. Corresponding RBS schematic diagram is shown in Fig.2.5. The dual axis Intelligent Motion controller (IMC) which accepts simple ASCII commands from the PC and controls the tilt angular rotation(θ) to a resolution of 0.01° over 360° and the azimuthal angular rotation (ϕ) over 0 to 360° to a resolution of 0.001°.

In this RBS, the source generates a beam of collimated and monoenergetic particles of energy E_0 . A typical case is a beam current 10-100 nA of 2 MeV He⁺ ions in a 1 mm² area. Such ions impinge on the sample object to be analyzed. Almost all of the incident particles come to rest within the sample.

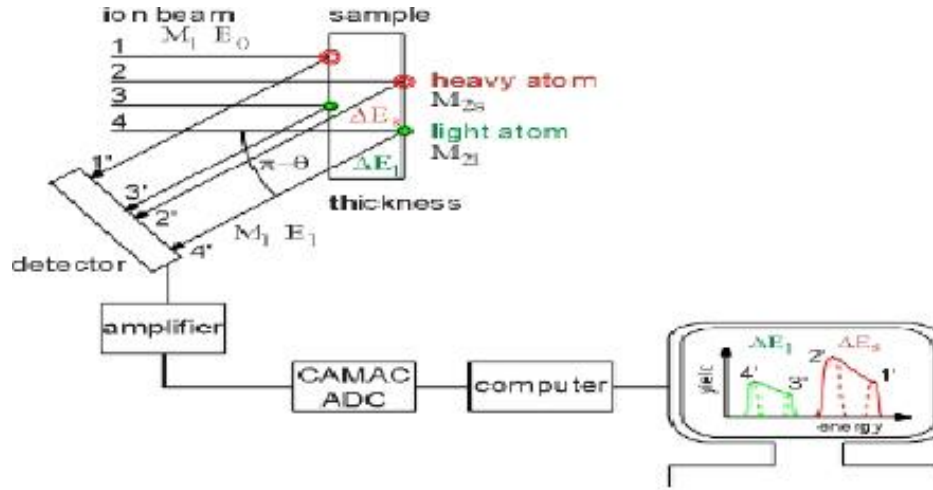


Fig 2.5: Schematic diagram of RBS setup

A very few ions scattered back from the sample, are detected using semiconductor detector which produces an analog signal proportional to the energy of backscattered particle. The output analog signal is processed by a multichannel analyzer, which subdivides its magnitude into series of equal increments. Each increment is numbered and referred to as a channel. An event whose magnitude falls within a particular channel is registered there as a count. At the end of the experiment each channel has registered a certain number of counts. The output of the multi-channel analyzer is thus a series of counts contained in the various channels. The analog signal generated by the analyzer contains quantitative information on one particular parameter of the detected particle. Correspondingly, a spectrum obtained with such a detector is a backscattering energy spectrum.



Fig 2.6: *Photograph of RBS Facility*

We have also used the RBS facility made available recently at IUAC, New Delhi for the analysis of few samples. The photograph of the RBS facility available at IUAC is shown in Fig.2.6.

The RBS data is analyzed by a simulation program SIMNRA to find out the elemental composition, film thickness and depth profile.

Ideal applications of RBS analysis are,

- Thin film composition/thickness
- Areal concentrations (atom/cm^2)
- Film density (when thickness is known)
- Ion beam mixing in two or more layers of the film

Advantages of RBS analysis are,

- Non-destructive compositional analysis
- Quantitative without standards
- Whole wafer analysis
- Hydrogen measurements (HFS mode)
- Low-Z element sensitivity (NRA mode)

Limitations of RBS analysis are,

- Large analysis area (~2 mm)
- Useful information limited to top ~1 μm of samples
- Cannot distinguish two elements which have the low mass number difference

2.4.4 Ion implantation

Ion implantation is a material engineering process by which ions of a material can be implanted into another solid, thereby changing the physical properties of the solid. Ion implantation is used in semiconductor device fabrication and in metal finishing, as well as various applications in materials science research. The ions introduce both a chemical change and a structural change in the target.

Ion implantation equipment typically consists of an ionization chamber, where ions of the desired material are produced; an accelerator, where the ions are electrostatically accelerated to a high energy; and a target chamber, where the ions impinge (implanted into) on a target.

The two key and important parameters defining the final implant profile are dose (usually given in atoms/cm²) and energy (in keV). The dose is related to the beam current i by the relation,

$$D = It/q_i A \quad (1)$$

where t indicates implantation time, A is beam area and q_i is the charge per ion. Typical beam currents and implantation doses range from $1\mu\text{A}$ to 30mA and 10^{11} to 10^{16} atoms/cm²,

respectively. The lowest energies used start at the sub keV area for ultra shallow junctions to the MeV range for deep wells. When the ions enter the substrate they continuously lose the energy and change directions with the target atoms. Due to the random nature of the collisions the total distance travelled (range) and its projection on the direction parallel to the ion beam (projected range) are random variables. R_p denotes the projected range, the depth where most of the ions stop. When the implanted ion enters the target material there are two main effects that cause an energy loss are

- Elastic collisions with the atoms of the target material
- Inelastic collisions with the electrons

In semiconductor technology, ion implantation is now an indispensable part of the integrated circuit fabrication process. One of the emerging fields where ion implantation is used extensively is the synthesis of nanocrystals, by a process called *ion beam synthesis*.

In this present thesis work, 1 MeV Ge^+ ions were implanted at different fluences ranging from 1×10^{16} to 1×10^{17} ions/cm² into 4 μm thick SiO_2 on p type Si wafers. Complete details of this implantation and the results are given the chapter 3.

2.5 Rapid thermal annealing (RTA)

RTA is faster than furnace annealing because the ramping and cooling cycle takes place within few minutes compared to hours in furnace annealing. The special arrangements in RTA can significantly reduce wafer emissivity variation and temperature non-uniformities. RTA process involving higher heating rates have long been used in the semiconductor industry as an alternative to the conventional furnace annealing. High temperature/short time annealing is of interest in the processing of thin films in order to reduce unwanted diffusion during annealing and to minimize interaction between film and substrate.

The RTA system consists of array of tungsten-halogen lamps, symmetrically placed above and below the chamber, in order to uniformly heat the wafer. In the present experiments, samples were placed in a graphite susceptor during annealing and the flow rate of ambient N_2 was 1500 sccm. A pair of thermocouples monitored the temperature during annealing. Ramp up rates of about 30°C/sec were applied to rise the temperature from ambient to the required annealing temperatures. Fig.2.7 shows the typical RTA cycle with a controlled cooling phase.

In this case, the ramp down rate was programmed to have slower rates with a holding step at different temperatures in order to minimize slip formation.

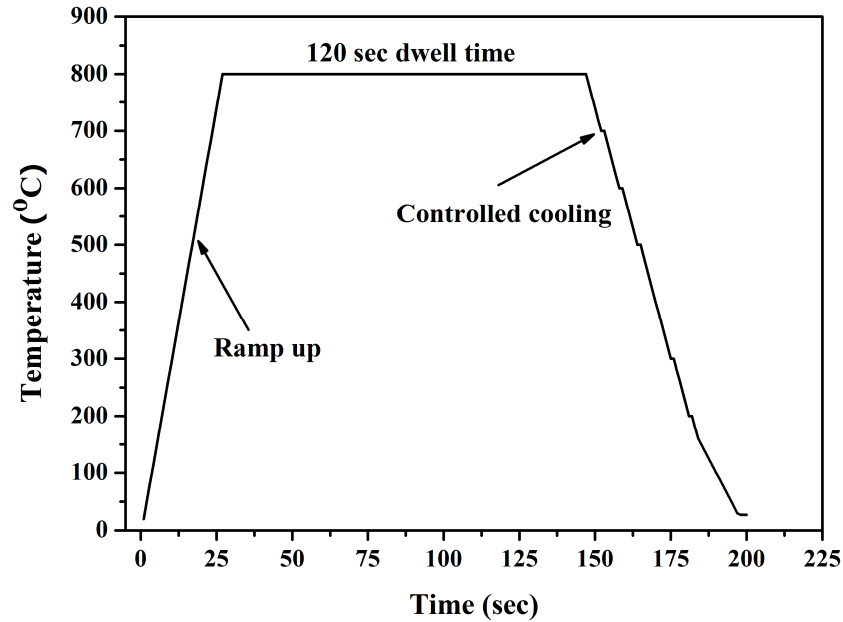


Fig 2.7: Typical annealing profile of RTA

RTA has been shown to be very efficient method to synthesize nanocrystals of Si and Ge compared to the conventional furnace annealing [3, 4]. The as-deposited samples were subjected to RTA in order to synthesize Ge NCs in Ge+SiO₂ composite thin films prepared by RF co-sputtering. As grown samples were annealed using RTA at different temperatures such as 700°C and 800°C. The details of various results have been presented in respective chapters.

2.6 Structural characterization – X-ray Diffraction (XRD)

X-ray diffraction is a well-known technique for characterizing the crystal structure of materials. X-rays have a wavelength of the order of Angstroms (10^{-10} m), which is comparable to the inter-atomic spacing in crystalline solids. Therefore, a diffraction pattern can be observed when a beam of x-rays is directed on a crystalline material (where the atoms are arranged periodically). This diffraction pattern is directly related to the crystal structure of the material under observation. The schematic of the XRD is shown in Fig.2.8.

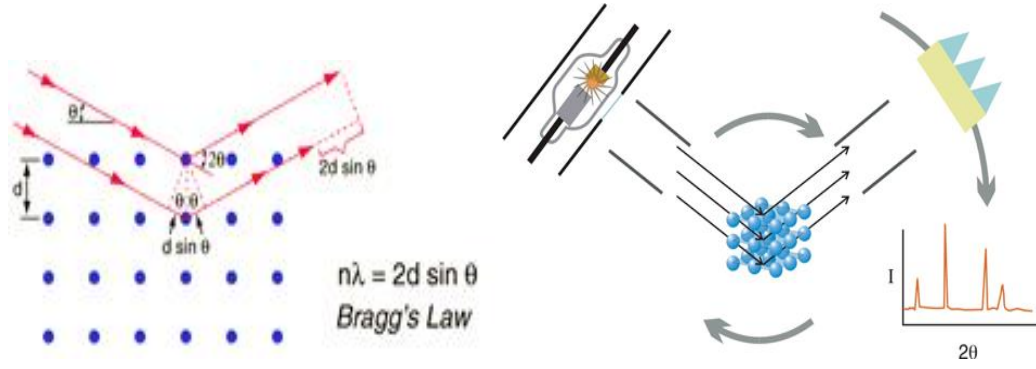


Fig 2.8: Schematic diagram of XRD

The crystal structure of Ge NC thin films was determined using XRD. X-ray diffractometer equipped with Co K ($\lambda = 1.5405 \text{ \AA}$) radiation is used for the experiments in grazing-incident x-ray diffractometer (Bruker D8 Discover). The GI-XRD pattern was obtained with a grazing angle of 1° . Calibration using a Si standard was done to account for the instrumental line broadening and the value was approximately 0.10° for Bruker diffractometer. The XRD patterns of all films were indexed using joint committee on powder diffraction standards (JCPDS) [5]. These results gave important information regarding the variation in film orientation, lattice constant, crystallite size and strain as a function of irradiation.

2.6.1 Crystallite size and lattice parameter calculation

The crystallite sizes of the films were calculated by a line profile analysis of the peak broadening. The crystallite size D was estimated using the below Scherrer equation

$$D = \frac{0.94 \lambda}{\beta \cos \theta_\beta} \quad (2)$$

Here λ is the x-ray wavelength (Cu-K radiation, $\lambda = 1.5405 \text{ \AA}$), β is full width at half-maximum of the XRD peak and θ_β is the Bragg diffraction angle.

The lattice parameter was calculated using 2 peak position from the relation

$$d_{hkl} = \frac{a}{\sqrt{h^2 + k^2 + l^2}} \quad (3)$$

where a is the lattice constant, d is spacing between the planes and h, k, l are miller indices.

2.7 Micro-Raman spectroscopy

The unique advantage of Raman spectroscopy is that it can be used to selectively excite a needed portion of the molecule by changing the excitation wavelength. Raman spectroscopy is also a convenient probe for the vibrational energy levels within a molecule which easily provide molecular fingerprints. Also it doesn't require any sample preparation, and samples are not destroyed during characterizations. The vibrational bands of water molecules are usually small and easily subtracted and Raman spectra contain sharp bands that are characteristic of the specific molecular bonds in the sample. The intensity of the bands in a Raman spectrum is proportional to the concentration of the corresponding molecules and thus can be used for quantitative analysis. In the present work, we have investigated Raman peaks of Ge nanocrystals samples using HR 800 Horiba Jobin Yvon confocal micro-Raman spectrometer as shown in figure 2.9. It consists of three excitation laser sources. He:Ne laser which provides 632 nm wavelength, Argon ion laser which provides 514 nm, and diode laser which provides 785 nm wavelength. The detecting system is CCD. A notch filter is used in the HR 800 for the rejection of the exciting line. It is specific for one wavelength and it is changed when excitation wavelength source is changed. A silicon test sample which shows Raman characteristic spectrum at 521 cm^{-1} is provided to check for Raman signal before collecting any Raman signals for specimen. A joy stick is provided to position the sample exactly under the illumination spot. Also the sample holder is placed on a XY stage so that Raman mapping can be carried out for different samples.

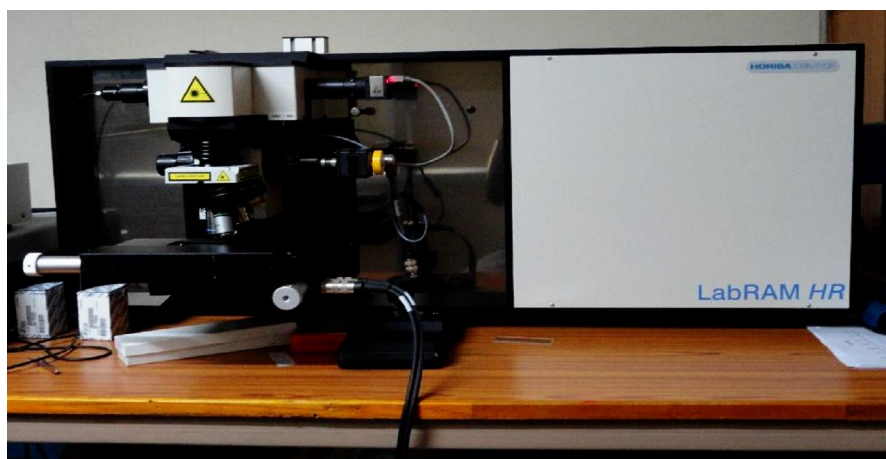


Fig 2.9: HR 800 Horiba Jobin Yvon confocal micro-Raman spectrometer

Raman scattering spectra of the as-deposited, annealed and SHI irradiated samples were obtained in back scattering configuration with HR 800 Horiba Jobin Yvon micro raman spectrometer using 514.5 nm laser excitation source. Shift in the peak position and asymmetrical broadening of the Raman peak with the spectrum of the bulk Ge have been discussed. The presence of Ge/Si NCs was observed from the Raman spectra and the results are discussed in respective chapters.

2.8 Field Emission-Scanning Electron Microscopy (FE-SEM)

A scanning electron microscope (SEM) is a type of electron microscope that images a sample by scanning it with a high-energy beam of electrons in a raster scan pattern. The electrons interact with the atoms that make up the sample producing signals which contain information about the sample's surface topography, composition and other properties such as conductivity. The types of signals produced by SEM/FESEM include secondary electrons, back-scattered electrons (BSE), characteristic X-rays, light (cathode-luminescence), specimen current and transmitted electrons. Secondary electron detectors are common in all SEMs, but it is rare that a single machine would have detectors for all possible signals. The signals result from interactions of the electron beam with atoms at or near the surface of the sample.

A field-emission SEM provides narrower probing beams at low as well as high electron energy, resulting in both improved spatial resolution and minimized sample charging and damage. There are two classes of emission source: thermionic emitter and field emitter. Emitter type is the main difference between the Scanning Electron Microscope (SEM) and the Field Emission Scanning Electron Microscope (FESEM). Thermionic Emitters use electrical current to heat up a filament; the two most common materials used for filaments are Tungsten (W) and Lanthanum Hexaboride (LaB_6). When the heat is enough to overcome the work function of the filament material, the electrons can escape from the material itself. Thermionic sources have relatively low brightness, evaporation of cathode material and thermal drift during operation. Field Emission is one way of generating electrons that avoids these problems. A Field Emission Gun (FEG); also called a cold cathode field emitter, does not heat the filament. The emission is reached by placing the filament in a huge electrical potential gradient. The FEG is usually a wire of Tungsten (W) fashioned into a sharp point. The significance of the small tip radius (~ 100 nm) is that a high electric field can be

concentrated in a small area, so that the work function of the material is lowered and electrons can leave the cathode. FESEM uses Field Emission Gun producing a cleaner image, less electrostatic distortions and spatial resolution $< 2\text{nm}$ (that means 3 or 6 times better than SEM).

Figure 2.10 shows a schematic diagram of FESEM. To cause field electron emission, a sharply pointed Schottky-type emitter is held at several kilovolts relative to nearby electrode which results in sufficient potential gradient at the emitter surface. Thermionic emission is enhanced by barrier lowering in the presence of high electric field for Schottky type emitter which is a thermal field emitter (TFE) cathode. A layer of zirconium oxide is coated on a tungsten tip to make a Schottky emitter. A high energy (typically 10-30 keV) electron beam, emitted from a tungsten tip is focused to a spot size of 1 to 5 nm by the condenser magnetic lenses and thereby it passes through a pair of scanning coils, which raster the beam across the surface.

Generation of low energy secondary electrons takes place when these focused electrons are incident on the specimen, which are detected by a scintillator-photomultiplier device and the resulting signal is rendered into a two-dimensional intensity distribution that can be viewed and saved as a digital image. The most common imaging mode monitors low energy ($<50\text{ eV}$) secondary electrons which originate within a few nanometers from the surface. Back scattered electrons are those high-energy electrons which are elastically scattered and possess the same energy as the incident electrons. The probability of backscattering increases with the atomic number Z of the sample material. Back scatter electrons are used to detect contrast between areas with different chemical compositions. Because these electrons are emitted from a depth in the sample, the resolution in the image is not as good as for secondary electrons.

Figure 2.11 shows a Photograph of the Field emission-scanning electron microscope (model: Carl ZEISS, FEG, Ultra 55) which is used in this thesis. Also, it has got EDS attachment where one can find out the percentage composition of various elements. The details are mentioned in the next section. We have used FESEM to image surface micro structures.

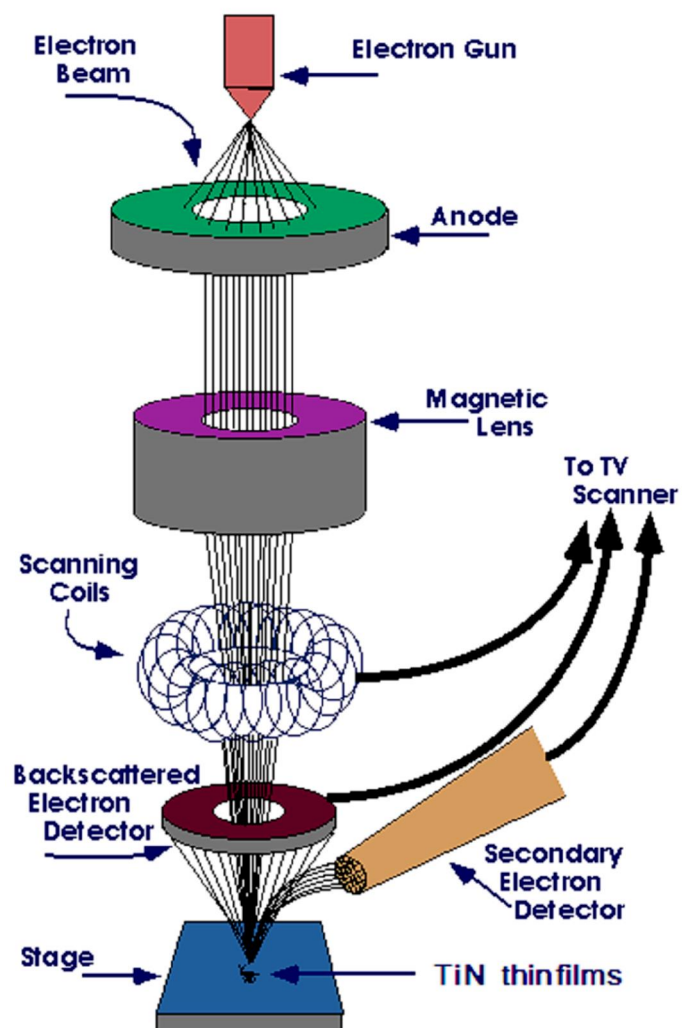


Fig 2.10: Schematic diagram of field emission scanning electron microscopy



Fig 2.11: Photograph of the Field emission-scanning electron microscope (model: Carl ZEISS, FEG, Ultra 55).

2.9 Energy dispersive x-ray absorption spectroscopy (EDS)

Energy Dispersive X-Ray Spectroscopy (EDS) is a chemical analysis technique used in conjunction with scanning electron microscopy (SEM). The EDS technique detects x-rays emitted from the sample during bombardment by an electron beam to characterize the elemental composition of the analysed volume. Features as small as 1 μm or less can be analysed. The process of x-ray emission from the sample surface is depicted in figure 2.12. When the sample is hit by the electron beam from SEM, electrons are ejected from the atoms comprising the sample's surface. The resulting electron vacancies are filled by electrons from a higher state, and an x-ray is emitted to balance the energy difference. The x-ray energy is characteristic of the element from which it is emitted. The EDS X-ray detector measures the relative abundance of emitted x-rays versus their energy. The detector is made up of lithium-drifted silicon, a solid-state device. A charge pulse that is proportional to the energy of X ray

is created when x-rays strike the detector. Using a charge sensitive preamplifier, the charge pulse is converted to a voltage pulse. This signal is then sent to a multichannel analyzer where the pulses are sorted by voltage. The energy, as determined from the voltage measurement, for each incident x-ray is sent to a computer for display and further evaluation. The spectrum of x-ray energy versus counts is evaluated to determine the elemental composition of the sampled volume. In the thesis, the chemical composition of the few thin films is determined using EDS analysis. EDS spectrum is obtained from FESEM using an INCA EDX system, which is equipped with an Oxford Instruments. The operating voltage for EDS measurement is 20 kV.

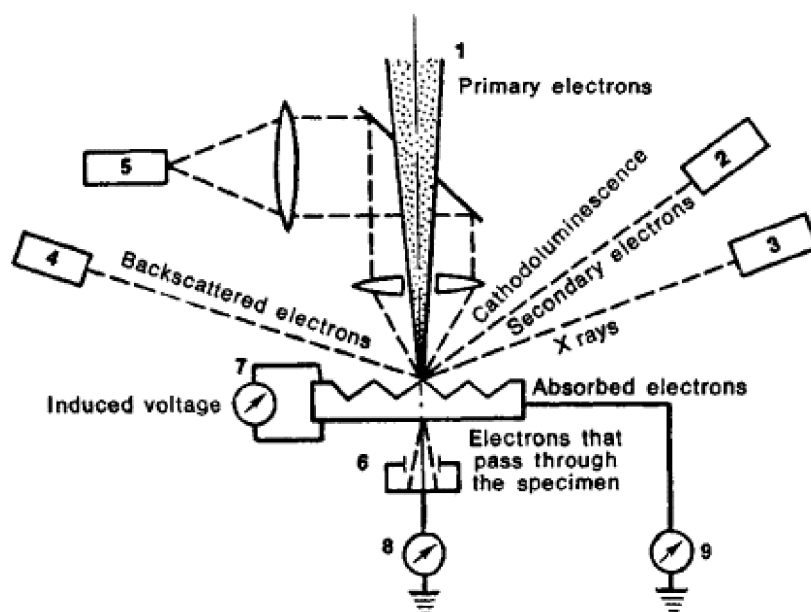


Fig 2.12: X-ray emission from the sample, when charged electron beam hits the sample surface.

2.10 Transmission Electron Microscopy (TEM)

Since, the wavelength of electron is much smaller than that of light, the optimal resolution attainable for TEM image is several orders of magnitude higher than that for a optical microscope. In transmission electron microscopy (TEM), the specimen is bombarded with an electron beam. Few electrons are transmitted through the sample, some are also scattered or diffracted. The scattered and diffracted electrons form the image contrast appears as darker areas in the image because the denser or thicker parts of the sample scatter as well as absorb more electrons [7, 8]. The imaging system of a TEM consists of at least three lenses, the objective lens, the intermediate lens (or lenses), and the projector lens. The intermediate lens can magnify the first intermediate image, which is formed just in front of this lens, or the first diffraction pattern, which is formed in the focal plane of the objective lens, by reducing the excitation [7]. Objective apertures α_o between 5 and 20 mrad, can be produced using the bright-field mode (BF) with a centered objective diaphragm which is the typical TEM mode, with which scattering contrast and diffraction contrast can be enhanced. For high-resolution phase contrast, the aperture should be relatively large ($\alpha_o \times 20$ mrad) to transfer high spatial frequencies. The purpose of the diaphragm is to decrease the background by absorbing electrons scattered at very large angles. The resolution is limited by the attenuation of the contrast-transfer function (CTF) caused by chromatic aberration and not by the objective aperture α_o . Normally, the specimen is irradiated with small illumination apertures $\alpha_i \approx 1$ mrad. For high resolution, an even smaller aperture $\alpha_i \approx 0.1$ mrad is necessary to avoid additional attenuation of the CTF by partial spatial coherence.

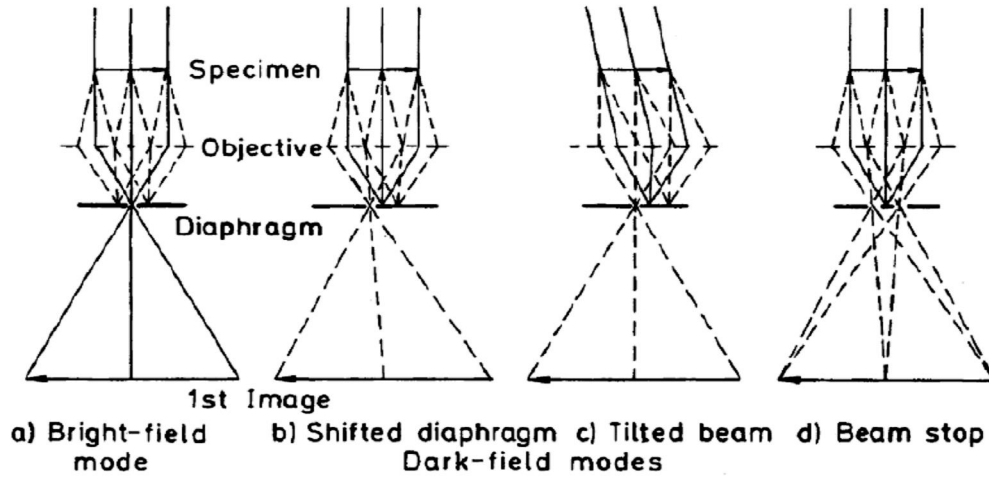


Fig 2.13: (a) Bright-field mode with a centered objective diaphragm and production of a darkfield mode by (b) a shifted diaphragm, (c) a tilted beam, and (d) a central beam stop.

In the dark-field mode (DF), the primary beam is intercepted in the focal plane of the objective lens. Different ways of producing dark-field conditions are in use. The shifted-diaphragm method as shown in figure 2.13 (b) has the disadvantage which worsens the chromatic aberration as scattered electrons pass through the objective lens on off-axis trajectories. To incorporate the chromatic aberration, the most common mode is that in which the primary beam is tilted as shown in figure 2.13 (c) so that the axis strikes the centered diaphragm. The image is produced by electrons scattered into an on-axis cone of aperture α_0 . This mode has the advantage that off-axis aberrations are avoided. Thus, there is no increase of chromatic error. Asymmetries in the dark-field image can be avoided by using a central beam stopper that intercepts the primary beam in the back focal plane by employing a thin wire stretched across a circular diaphragm as shown in figure 2.13 (d). As there are fewer scattered electrons, DF micrographs need a longer exposure time. For high resolution, the contrast-transfer function (CTF) of DF is nonlinear, whereas the CTF of the BF mode is linear for weak-phase specimens. In the present thesis, we have used Transmission electron microscope as shown in figure 2.14 (model: Tecnai 20 G2 STwin, FEI electron microscope operated at 200 kV using Gatan CCD camera) to investigate the sizes of nanoparticles.



Fig 2.14: Photograph of the TEM facility available at UoH

2.11 Atomic force microscopy

Atomic force microscopy (AFM) is a very high-resolution type of scanning probe microscopy (SPM). SPM images are obtained by scanning a sharp probe across a surface while monitoring and compiling the tip-sample interactions to provide an image. The measurement of local physical properties of the material is extremely important for semiconductor fabrication. Using the SPM technique one can study the local physical properties of the materials down the atomic scale. The resolution obtained by this technique can resolve the single atom and the map of the real 3-D images of the surface.

Conductive-Atomic Force Microscopy (C-AFM) is a mode of atomic force microscopy in which a conductive tip is scanned in contact with the conductive sample surface, while a voltage is applied between the tip and the sample, generating a current image. Using (C-AFM) one can probe the local variations in the conductivity of a material (crystal or thin film) with microstructure and thus examine the local variation of current at grain and grain boundaries.

Surface morphology of the samples has been characterized in the present investigations using SPA 400 of SPI 3800 probe station of Seiko Instruments, Japan. Photograph of AFM is

shown in Fig. 2.15. Images have been taken in contact mode using silicon nitride probe having spring constant of 0.58 N/m. A phase image, typically collected simultaneously with a topographical image, maps the local changes in material physical or mechanical properties [9]. Though phase images have been recorded but discussions are confined to the topographical images. In NC-AFM mode, the system monitors the resonant frequency or vibrational amplitude of the cantilever and keeps it constant with the aid of a feedback system that moves the scanner up and down. By keeping the resonant frequency or amplitude constant, the system also keeps the average tip-to-sample distance constant. As with contact AFM (in constant-force mode), the motion of the scanner is used to generate the data set. NC-AFM does not suffer from the tip or sample degradation effects that are sometimes observed after taking numerous scans with contact AFM. As mentioned above, NC-AFM is also preferable to contact AFM for measuring soft samples. In the case of rigid samples, contact and non-contact images may look the same. However, if a few monolayers of condensed water are lying on the surface of a rigid sample, for instance, the images may look quite different.



Fig 2.15: Photograph of the SPA-400 atomic force microscopy used in the present study

2.12 Thickness measurement: Surface profilometer

The thickness of the samples was measured using stylus profiler (also known as profilometer) (Model XP-1, Ambios Technology, USA). Surface profilometry is a direct, simple and fast measurement technique for determining the physical thickness of thin films. The only requirement is the existence of a step as shown in figure 2.16. Diamond stylus (tip) was used to determine the thickness of co sputtered Ge+SiO₂ thin films.

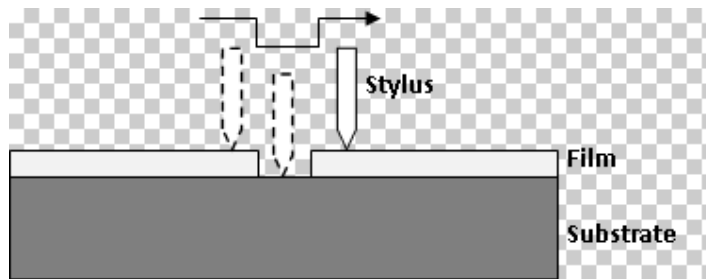


Fig 2.16: Illustration of stylus profilometer measure of film thickness

2.13 Conclusions

This chapter has described all the experimental facilities that have been utilized for the work reported in this thesis. These include the Swift Heavy ion irradiation (SHI) facilities, and those used for the synthesis and characterization of the pristine and irradiated samples. Further details of the relevant facilities have been discussed in the following chapters wherever required.

2.14 References

1. D Kanjilal, S Chopra, M M Narayanan, I S Iyer, V Jha, R Joshi and S K Datta, Nucl. Instr. and Meth. A 238, (1993) 97.
2. K Suresh, B Sundaravel, B K Panigrahi, K G M Nair and B Viswanathan, Rev. Sci. Instrum. 75, (2004) 4891.
3. F Rooxboom_Ed¹ Advances in Rapid thermal and Integrated Processing, Kluwar Academic Publisher, 1996.
4. O Adeoya, M Hage Ali, J C Muller, P Siffert Appl. Phys. Lett. 50 (1987) 1736
5. JCPDS card # 04-0545 (for Ge) JCPDS card # 83-0544 (for GeO₂)
6. B D Cullity, Elements of X-ray Diffraction, second ed., Addison-Wesley, Reading, MA, 1978, 102.
7. L Reimer H Kohl, Transmission Electron Microscopy Physics of Image Formation, 5th Ed, Springer, New York, 10013, USA (2008).
8. Z L Wang, Transmission Electron Microscopy of Shape-Controlled Nanocrystals and Their Assemblies, J. Phys. Chem. B, 104, 1153-1175, 2000.
9. S N Magonov, V Elings and M -H Whangbo, Sur. Sci. Lett. 375, L385 (1997)

Chapter 3

Synthesis and Characterization of Ge NCs embedded in SiO₂ and the effects of heavy ion irradiation on these NCs

3.1 Introduction

The low dimensional semiconductor (Ge & Si) nanocrystals (NCs) are very important from basic and applied research point of view [1-3]. The structural, optical and electronic properties of these low dimensional, indirect band gap materials have been investigated extensively over the past few years [4, 5]. The NCs of these materials embedded in an insulating matrix have attracted a large number of researchers due to their potential applications in optoelectronic and memory devices [6]. Although porous Si is expected to be the most promising Si-based light emitting material, Ge NCs embedded in Silica have their own advantages [7]. It was reported, based on comparison of Si and Ge effective masses and energy differences between the indirect gaps, that it should be easier to modify the electronic structure around the band gap of Ge [8]. Out of the Ge and Si NCs embedded in SiO₂ matrix, Ge NCs have more technological advantages over Si NCs. The exciton Bohr radius of Ge (24 nm) is much larger than that of Si (5 nm), which indicates that the quantum confinement effects are more prominent in Ge NCs [8]. Ge NCs have garnered great attention as a promising candidate for charge storage device applications as nonvolatile memory [9]. It is well reported that all these properties of embedded Ge NCs are governed by their size [10]. Hence the size control of the NCs plays an important role in their applications. There are several established methods for the synthesis of Ge NCs embedded in SiO₂ such as atom beam sputtering [11], molecular beam epitaxy [12], chemical vapor deposition [13] and ion implantation [14] followed by high temperature annealing. Rapid thermal annealing (RTA) among various annealing processes has advantages in reducing unwanted diffusion during annealing and minimizes the interaction between film and substrate due to faster timing [11].

It is very important to synthesize Ge NCs of relatively smaller size than their exciton Bohr radius in view of their applications depending on size. Although most of the common synthesis methods enable us to get Ge NCs with fixed average NC size, the size tuning and modification is not possible in these synthesis methods directly. Ion beams can act as a tool in the synthesis and modification of nanostructured materials. In particular, ion irradiation has been established to be one of the versatile techniques for the modification of materials at nano-scale [15, 16]. In many cases irradiation can lead to self-organization or self-assembly in nanostructures instead of ending by creating defects or damage. Schmidt *et.al* [17, 18]

reported that Ge NCs were flattened into an oblate shape when 38 MeV iodine ion beam was used to irradiate various sizes of Ge NCs embedded in SiO₂. It was shown that the medium-sized nanospheres become oblates and smaller ones shape into rod-like structures whereas large Ge nanospheres remain spherical under the same irradiation energy and fluences. On the other hand, Antonova *et.al* [19] more recently reported the formation of small Ge NCs and the modification of existing Ge NCs in the SiO₂ matrix by 480 MeV Xe ion irradiation followed by a post-annealing process. They demonstrated the ability of ion irradiation to modify and/or create new Ge NCs in Ge:SiO₂ films with variable Ge composition. A high concentration of Ge NCs with a size of 265 nm was observed in the irradiated and subsequently annealed (at 500 °C) films, while the relatively large Ge NCs of 8-15 nm are formed without ion irradiation.

The motivation of present work is to synthesize Ge NCs and then to investigate the effects of heavy ion irradiation at different fluences on the size and shape of Ge NCs. We have performed the ion irradiation by 120 MeV Ag ions and 80 MeV Ni ions at various fluences on the Ge NCs embedded in SiO₂, which were previously synthesized by RF magnetron co-sputtering followed by RTA. The Ge NCs samples were characterized by X-ray diffraction (XRD) and Raman spectroscopy before and after ion irradiation. The presence of Ge NCs in the RTA annealed sample and the modification of those embedded Ge NCs due to ion irradiation have been observed by transmission electron microscopy (TEM).

3.2 Experimental Details

Thin films of Ge and SiO₂ nanocomposites were prepared on Si and quartz substrates by co-sputtering of Ge and silica using a RF magnetron co-sputtering technique. We have varied the composition of Ge in SiO₂ by varying the area of the SiO₂ and Ge in the composite target. The details of the samples have been given in table 3.1. The substrates were cleaned with acetone, isopropyl alcohol and deionized water before loading into the deposition chamber. The sputtering was performed with an Ar gas. The base pressure was 5×10^{-6} torr and the working pressure was maintained at 4.2×10^{-3} torr during the deposition at room temperature. The average thickness of the deposited samples is 300 nm which was measured with surface stylus profilometer. The as-deposited samples were subjected to RTA using a rapid thermal process system at 700°C and 800°C for 120 s in N₂ atmosphere (1500 SCCM) to synthesize

Ge NCs. The annealed samples were then irradiated with 120 MeV Ag ions and 80 MeV Ni ions (different ions were used for different samples, the details are given in table 3.1). The fluences were varied from 1×10^{13} to 1×10^{14} ions/cm². The energy losses as well as the ranges of the incident ions inside Ge and SiO₂ systems were calculated using Stopping and Ranges of Ions in Matter (SRIM) simulation code, and the values are given in table 3.2. Irradiation was performed in a high vacuum chamber at the pressure $< 10^{-6}$ torr. The samples were scanned over 1cm x 1cm area with the ion beam and a constant current of 1 pA (particle nano-Amp) was maintained throughout the irradiation process. XRD measurements were carried in glancing angle incidence mode with an incidence angle of 1° using a Cu K source (1.5406 Å). The Raman scattering measurements were carried out at room temperature in backscattering mode using 514.5 nm line of an Ar laser as an excitation source. Existence and the modification of Ge NCs embedded in Silica matrix have been confirmed using a transmission electron microscopy with electron-accelerating voltage of 200 kV for the RTA annealed samples and the ion irradiated samples.

Table 3.1: Details of the samples used in this chapter (RF Sputtering and RTA)

S.No	Sample	Ge at%	RTA details	Ion irradiation details	
				Ion & energy	Fluences (ions/cm ²)
1	Set A	32 at%	800°C	120 MeV Ag	1×10^{13} & 3×10^{13}
2	Set B	40 at%	700 and 800°C	80 MeV Ni	1×10^{13} , 3×10^{13} & 1×10^{14}

Table 3.2: The values of energy losses and projected ranges of incident ions in Ge ($\rho = 5.35 \text{ g/cm}^3$) and SiO₂ ($\rho = 2.32 \text{ g/cm}^3$).

Incident ion	Energy (MeV)	Electronic energy loss (keV/nm)		Nuclear energy loss (keV/nm)		Range (μm)	
		SiO ₂	Ge	SiO ₂	Ge	SiO ₂	Ge
Ag	120	12.31	17.46	0.0519	0.087	16	13
Ni	80	7.62	10.95	0.0167	0.028	16	12

3.3 Results and discussion

3.3.1 RBS results

Figures 3.1 and 3.2 show the RBS spectra of as-deposited samples of set A and set B. The sample stoichiometry was estimated by the simulation of the spectrum using the SIMNRA code. The Ge composition in the as deposited composite films of Ge+SiO₂ is determined to be about 32 at% and 40 at% for set A and set B samples respectively. The corresponding Ge, Si and O edges in the spectra are marked.

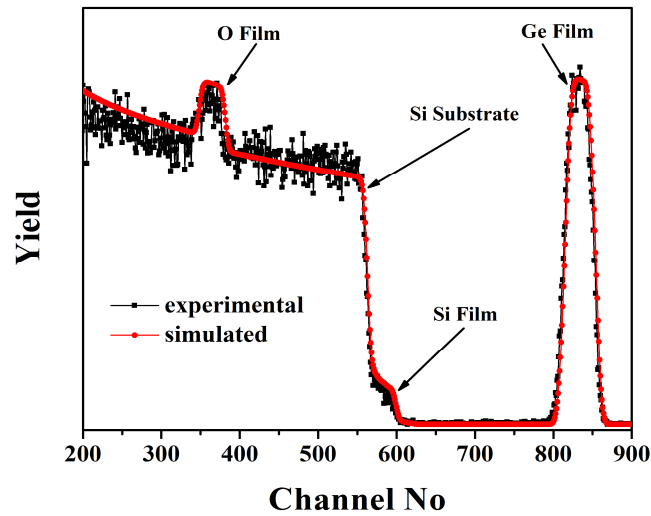


Fig 3.1: RBS spectrum of the as-deposited sample of set A

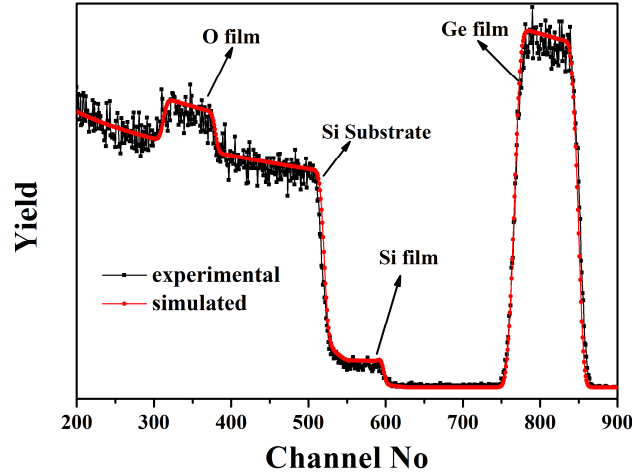


Fig 3.2: RBS spectrum of the as-deposited sample of set B

3.3.2 XRD results

The diffraction patterns of as-deposited, RTA treated and 120 MeV Ag irradiated samples of set A are presented in Fig 3.3. In case of the as-deposited sample, no noticeable peak is observed, whereas the RTA sample at 800 °C and the ion irradiated sample show three diffraction peaks corresponding to Ge (111), (220) and (311) planes. This indicates the formation of crystalline structure of Ge after annealing. The peak positions are matched with the respective JCPDS files [20]. The average size of the NCs is calculated using Scherrer's formula [21]. The crystallite size obtained from Ge (111) diffraction peak of the RTA sample is about 31 nm. During the RTA process at high temperature Ge atoms distributed in the as-deposited sample get higher mobility and crystallize by combining few or more atoms to form a bigger nanocrystal. These Ge NCs were formed by diffusion of Ge atoms or clusters inside SiO₂ matrix. At higher annealing temperature, the Ge atoms have higher mobility and Ge NCs are formed by diffusion of Ge atoms inside the silicon oxide matrix.

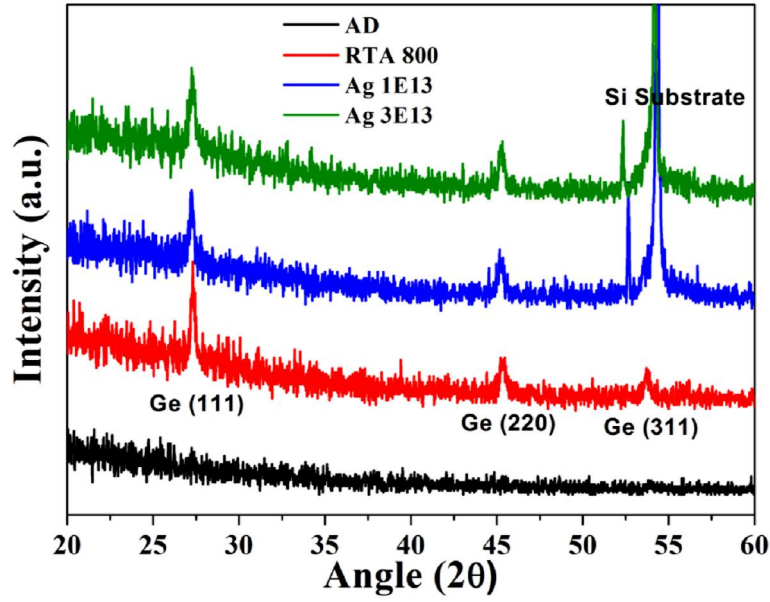


Fig 3.3: XRD patterns of set A as-deposited, RTA-treated, and 120 MeV Ag irradiated samples

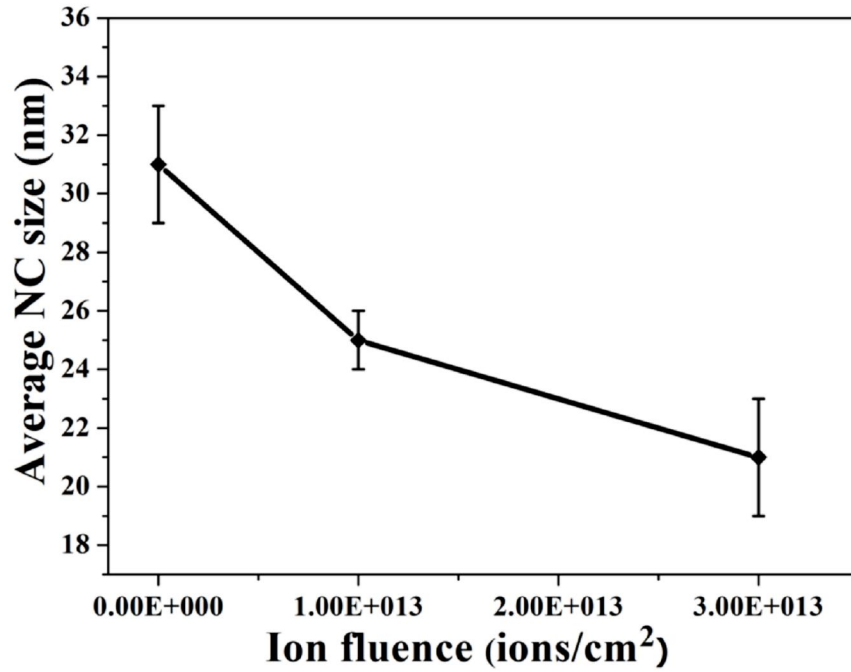


Fig 3.4: Variation of average NCs size with different irradiation fluences of 120 MeV Ag ions

Figure 3.4 shows the variation of the average size of Ge NCs with increase in the irradiation fluence. It is observed that the size of Ge NCs decreased with increased irradiation fluence. The NC sizes are determined from Ge (111) diffraction peak. The diffraction patterns of as-deposited and RTA treated samples of set B are shown in Fig 3.5. In the case of set B also; for as-deposited sample, no noticeable peak is observed, whereas the RTA sample at 700 and 800 °C show diffraction peaks corresponding to Ge (111) and (220) planes. This indicates the formation of crystalline structure of Ge NCs after annealing. As observed from the figure, XRD peak becomes sharper and the full width at half-maximum (FWHM) of the peak is reduced with the increase of annealing temperature. This indicates that the average size of nc-Ge increases with annealing temperature. The sizes measured using scherrer's formula for all the samples of set A and set B are given in table 3.3. It was observed that at a fixed RTA temperature 800°C the Ge NC size of annealed sample for set A is less than that of the respective set B sample i.e, the crystallite size is increased with an increase in Ge composition at a given annealing temperature 800°C. When the annealing temperature is higher, Ge atoms and small nanocrystals have higher mobility. Since the nc-Ge crystallization temperature is lower than the Ge melting temperature, Ge clusters and nanocrystals are formed by diffusion of Ge atoms or clusters inside the SiO₂ matrix. Therefore, an increase in annealing temperature leads to an increase of Ge crystallinity and crystallite size. Thus crystallinity improves with the annealing temperature as observed from the decrease in FWHM and an increase in intensity from the XRD peaks.

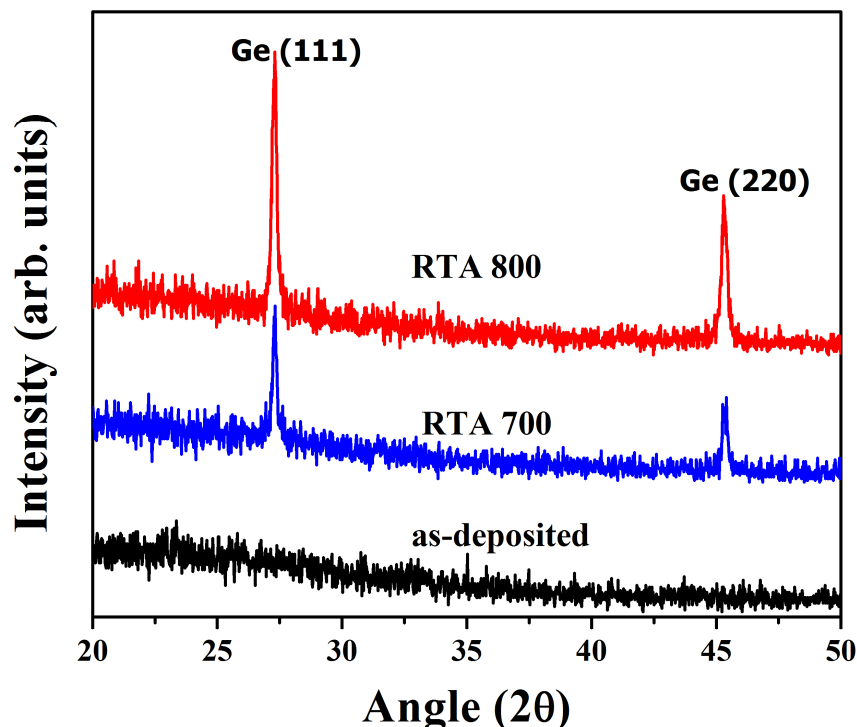


Fig 3.5: XRD patterns of set B as-deposited and RTA-treated samples

The 800°C RTA treated samples have been used for the ion irradiation studies. The 80 MeV Ni ions at various fluences have been employed to understand the effects of ion irradiation on the embedded Ge NCs. The diffraction patterns of 80 MeV Ni ions irradiated Ge NCs samples of set B at various fluences are presented in Fig 3.6. It was observed from the NC size measurements that the average size of the Ge NC decreases with the increase in fluence of irradiation. The FWHM of the Ge (111) peak has increased as shown in Fig 3.6(a), with the increase in fluence of irradiation and also the intensity of the peak has decreased.

The XRD pattern of the RTA annealed sample at 800°C of set B deposited on quartz substrate is shown in figure 3.7. It was observed that all the corresponding peaks of Ge NCs were present in the XRD pattern which indicates the formation of Ge NCs on quartz substrate as well. The average size of the Ge NCs was measured to be 40 nm for this sample. The formation of Ge NCs on quartz substrate suggests that the synthesized samples can be used in optoelectronic applications as quartz is a transparent substrate.

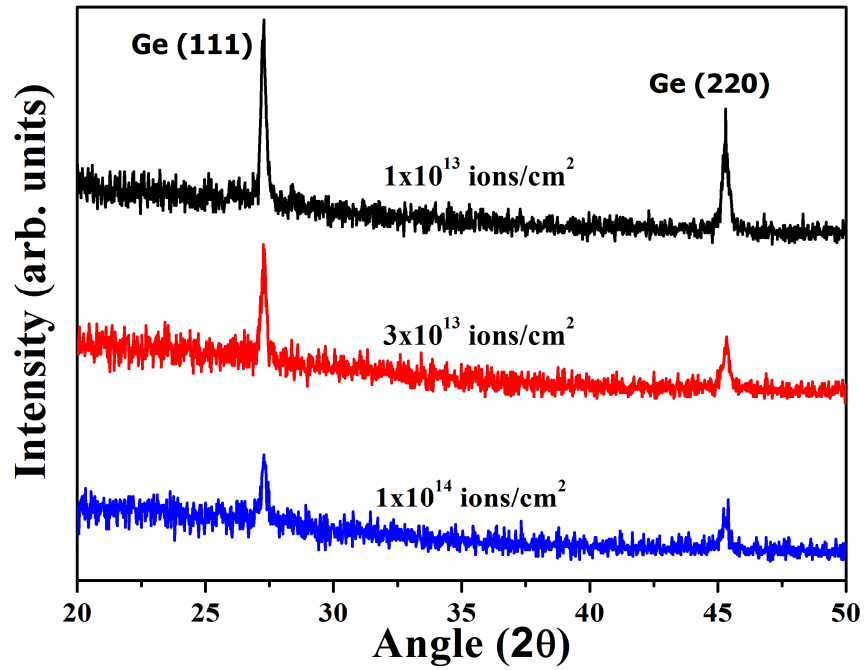


Fig 3.6: XRD patterns of set B (RTA 800°C) irradiated samples at various fluences

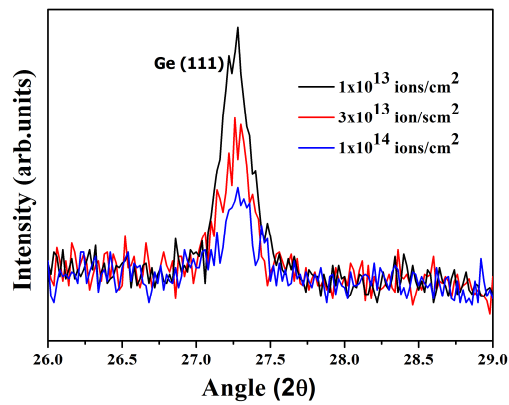


Fig 3.6 (a): Expanded view of the Ge (111) XRD peak of Fig 3.6

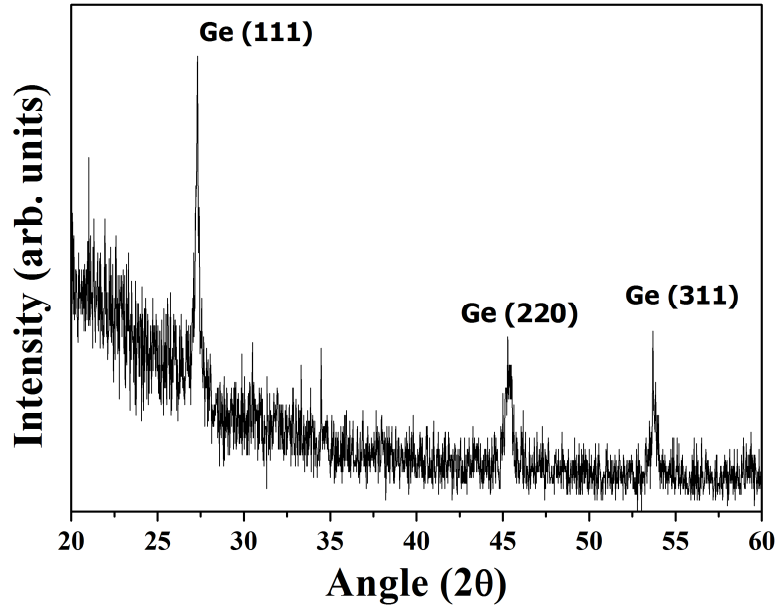


Fig 3.7: XRD pattern of set B RTA-treated sample deposited on quartz substrate

Table.3.3: Variation of Ge NC size of set A and set B samples

Sample	Ge NC size (in nm)	
	Set A	Set B
AD	0	0
RTA 700	-	32
RTA 800	31	40
Ag 1E13	26	-
Ag 3E13	21	-
Ni 1E13	-	34
Ni 3E13	-	29
Ni 1E14	-	22

3.3.3 Raman results

Raman spectra of as-deposited and RTA treated samples of set A and set B are shown in Fig 3.8 and 3.9 respectively. The as-deposited sample exhibits a broad Raman peak centered at 270 cm^{-1} , which corresponds to amorphous Ge. Raman spectrum of the annealed sample has a sharp peak centered around 302 cm^{-1} and this indicates the formation of Ge NCs upon annealing. Raman spectra of the annealed samples show a shift in the peak position and an asymmetrical broadening on the lower frequency side when compared with the spectrum of the bulk Ge sample. The shift of the Raman band in thin films can arise due to tensile or compressive strain and phonon confinement. The shift in the peak position is attributed to phonon confinement in NCs.

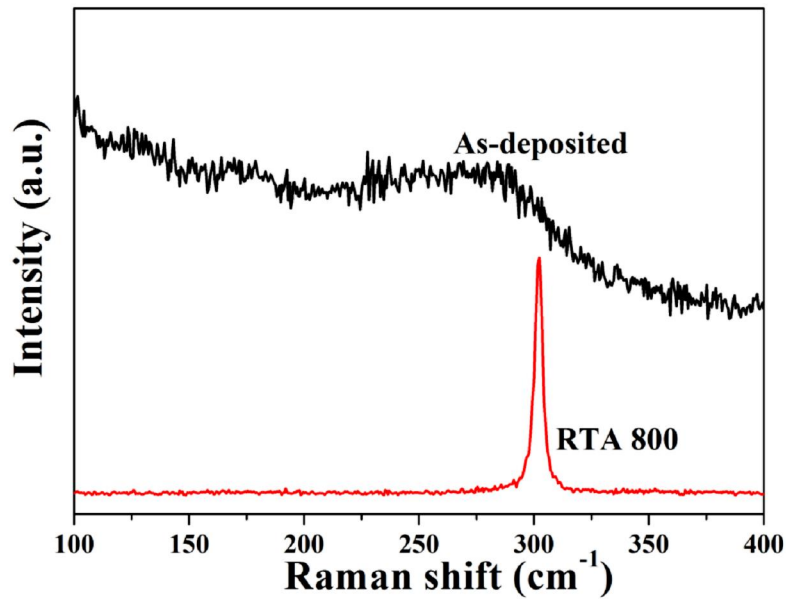


Fig.3.8: Raman spectra of set A as deposited and RTA treated samples

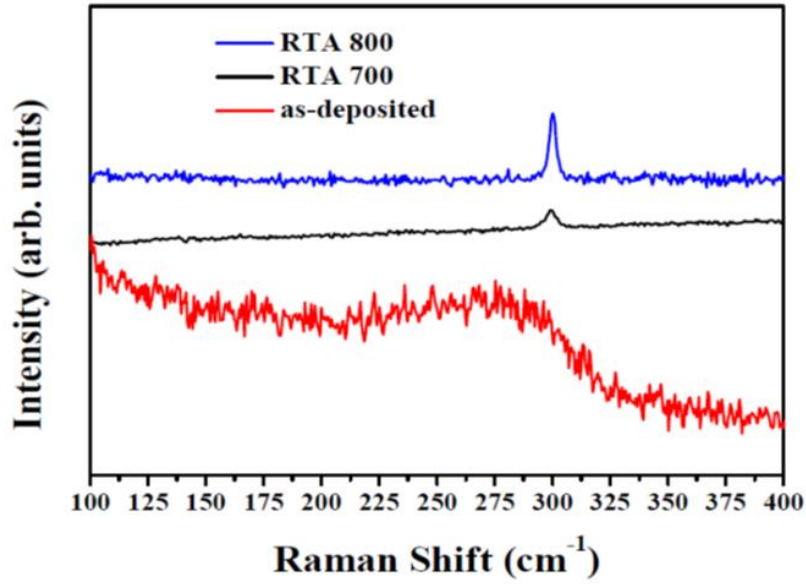


Fig 3.9: Raman spectra of set B as deposited and RTA treated samples

Figures 3.10 and 3.11 show the Raman spectra of the heavy ion irradiated set A and set B Ge NCs samples at different fluences. It can be seen that the peak position of Ge NCs corresponding to Ge-Ge optical phonons, shifts towards the lower wavenumber side as the irradiation fluence increases. Raman spectra of the irradiated samples also show an increase in the FWHM of the Ge NCs peak upon increase in irradiation fluence. This is a consequence of decrease in the average size of Ge NCs [21, 22]. This shift in the peak position indicates that a size reduction of the NCs due to the ion irradiation has taken place. The values of Ge NCs peak position, the shift of respective peaks, and change in the FWHM of the peak for various fluences of set A and set B irradiated samples are given in Table 3.4 (a) and (b) respectively.

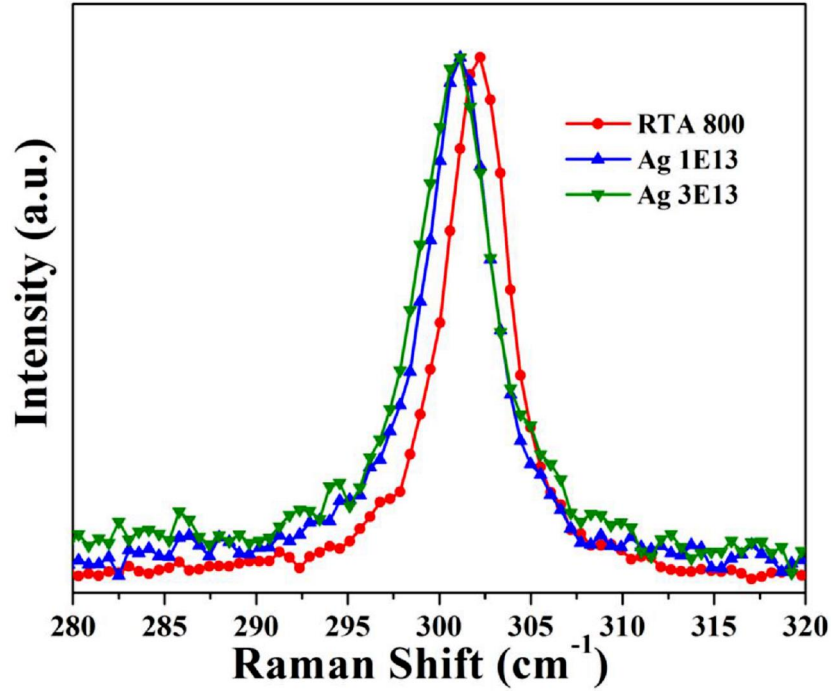


Fig 3.10: Raman spectra of the set A samples (RTA 800) irradiated with 120 MeV Ag ions and the RTA-treated sample without irradiation

Table 3.4 (a): Ge NCs peak position from Raman spectrum, its peak shift and change in FWHM of the peak for various fluences of ion irradiation (set A)

S.No	Sample with irradiation fluence	Ge NCs peak position (cm ⁻¹)	Shift in the peak position from its bulk value (cm ⁻¹)	FWHM of the Ge NCs peak (cm ⁻¹)
1	As deposited	270 (broad one)	-	-
2	RTA 800	302	-	4
3	120 MeV Ag 1E13	301	1	4.14
4	120 MeV Ag 3E13	299	3	4.57

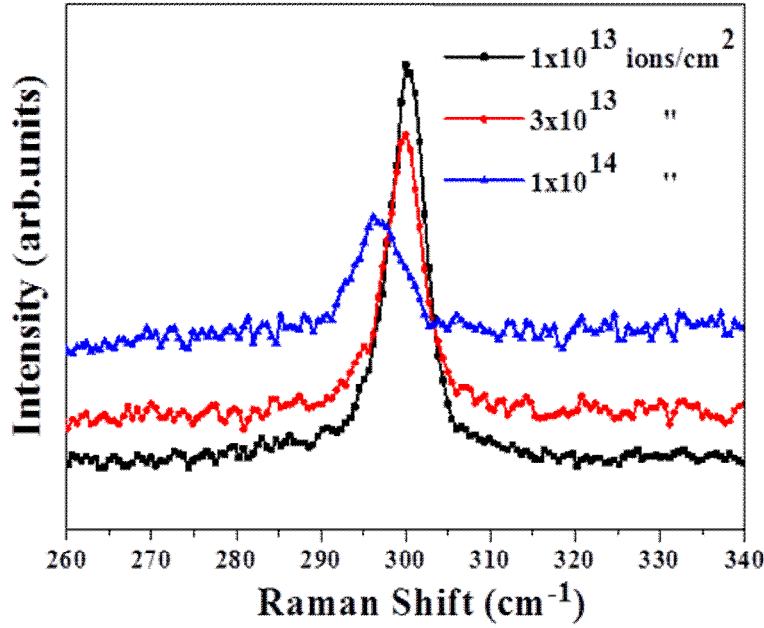


Fig 3.11: Raman spectra of the set B samples (RTA 800) irradiated with 80 MeV Ni ions

Table 3.4 (b): Ge NCs peak position from Raman spectrum, its peak shift and change in FWHM of the peak for various fluences of ion irradiation (set B)

S.No	Sample with irradiation fluence	Ge NCs peak position (cm ⁻¹)	Shift in the peak position from its bulk value (cm ⁻¹)	FWHM of the Ge NCs peak (cm ⁻¹)
1	As deposited	270 (broad one)	-	-
2	RTA 700	299	3	5.10
3	RTA 800	302	-	3.30
4	80 MeV Ni 1E13	300	2	4.74
5	80 MeV Ni 3E13	299	3	4.97
6	80 MeV Ni 1E14	296	6	5.11

Figure 3.12 shows the Raman spectra of the set B; RTA 800°C annealed sample with various laser powers of excited wavelength. It displays that with the increase in laser power no shift in the peak position is observed. The FWHM of the peak also has not changed much with the increase in laser power whereas only the intensity of the Raman peak is decreased. Hence it is confirmed that there is no shift in the peak position of Ge NCs with the increase in laser

power. Hence, the shift in the peak position and the broadening of the peak which is observed in the Ge NCs samples as a result of irradiation is due to the increase in the fluence of ion irradiation. So the Raman results also suggest a decrease in the average size of Ge NCs as result of irradiation.

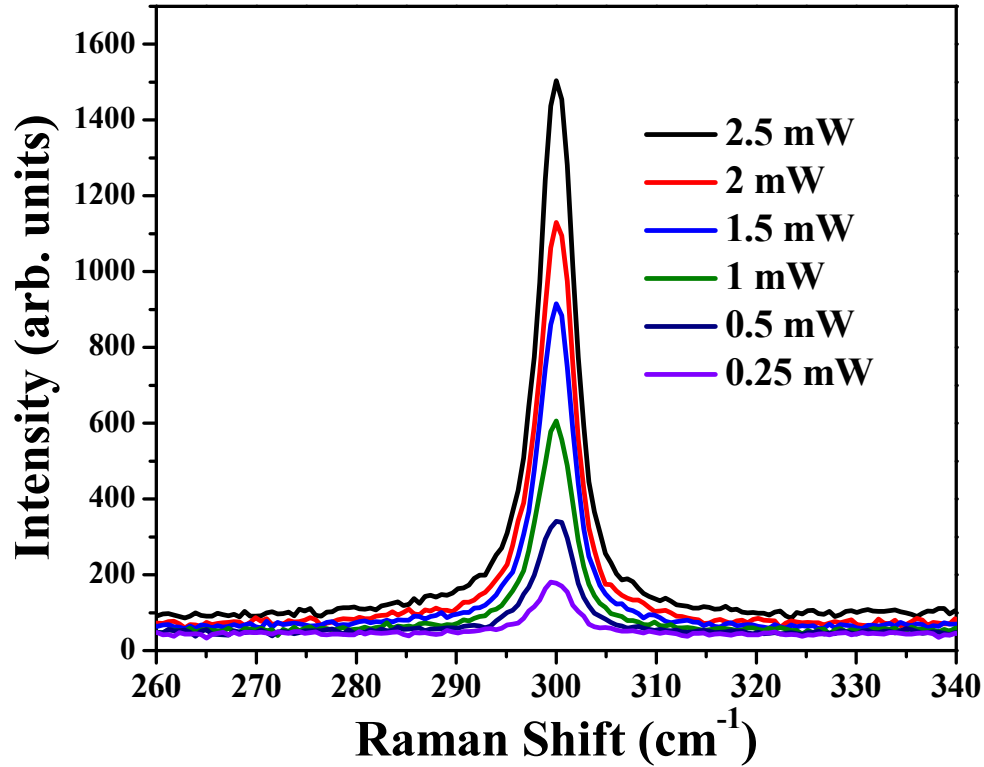


Fig 3.12: Raman spectra of the set B RTA 800 sample at various laser powers

3.3.4 TEM Results

The TEM images of typical Ge NCs obtained from the RTA 800°C annealed samples of set A and set B and the respective NC size distributions are shown in figures 3.13 and 3.14 respectively. One can clearly see the formation of Ge NCs as a result of annealing. The average NC size is found to be around 23 nm for set A and 28 nm for set B annealed samples.

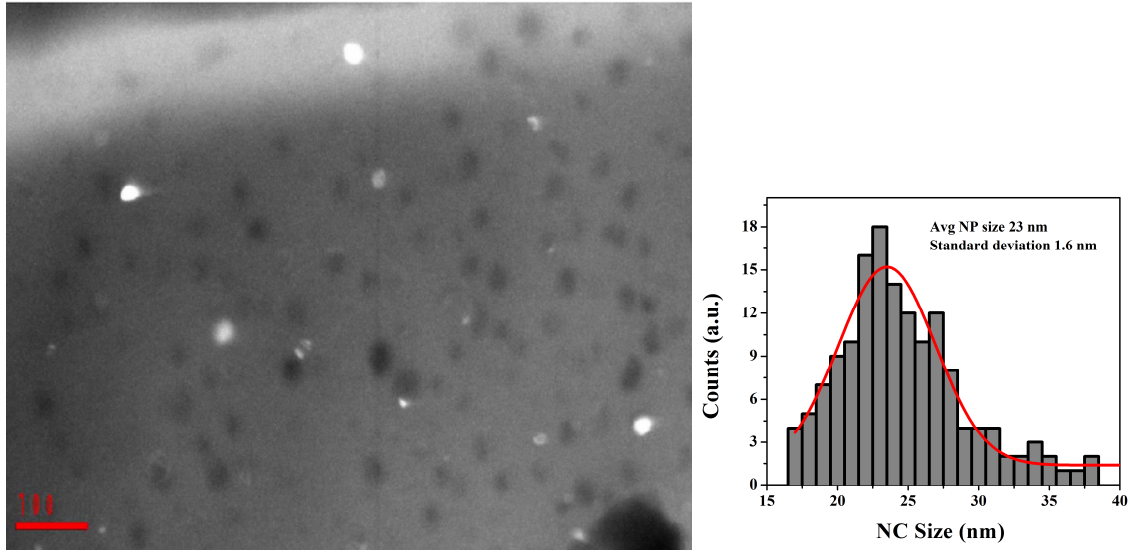


Fig 3.13: TEM image of Set A RTA 800°C sample and the NC size distribution

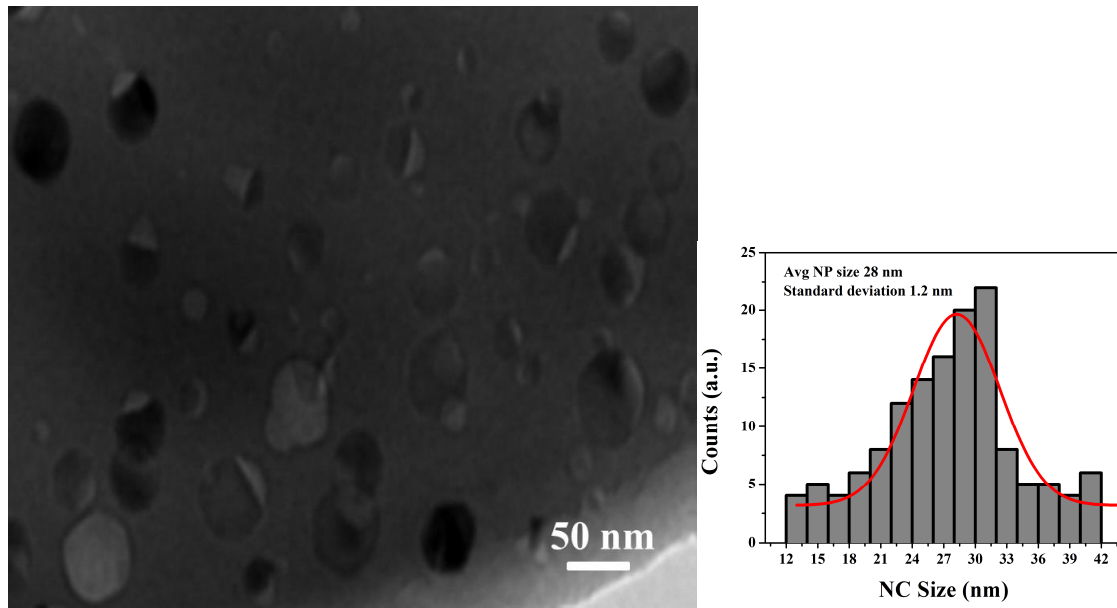


Fig 3.14: TEM image of Set B RTA 800°C sample and the NC size distribution

The TEM images of corresponding irradiated samples are depicted in figures 3.15 and 3.16 respectively for the set A and set B samples. It was observed that the average NC size reduces and a growth of small size NCs takes place, as a result of ion irradiation. It was also observed from the selective area electron beam diffraction pattern (Fig 3.15) that the NCs finally become partially amorphous as a result of irradiation.

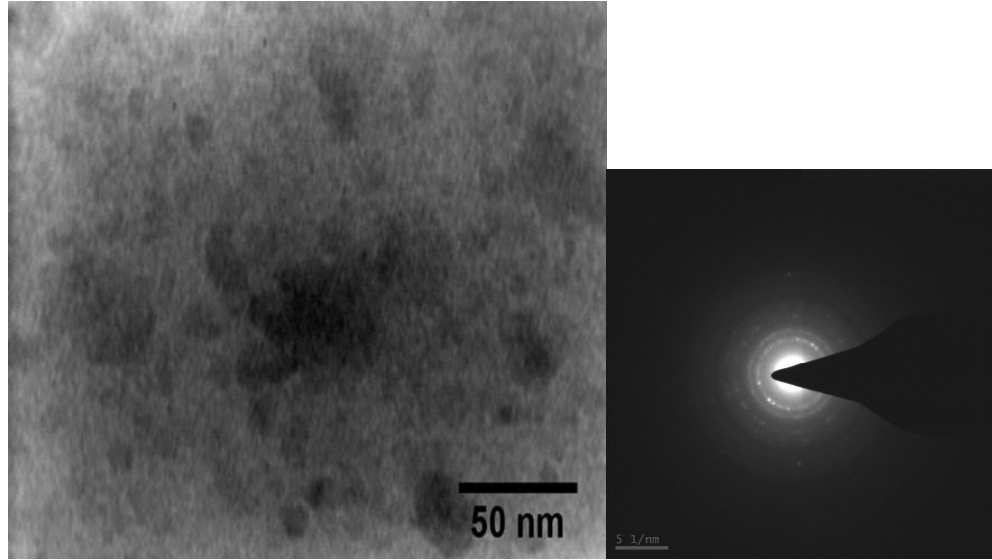


Fig 3.15: TEM image of Set A irradiated Ge NCs sample with 3×10^{13} ions/cm² fluence and the selective area electron diffraction pattern

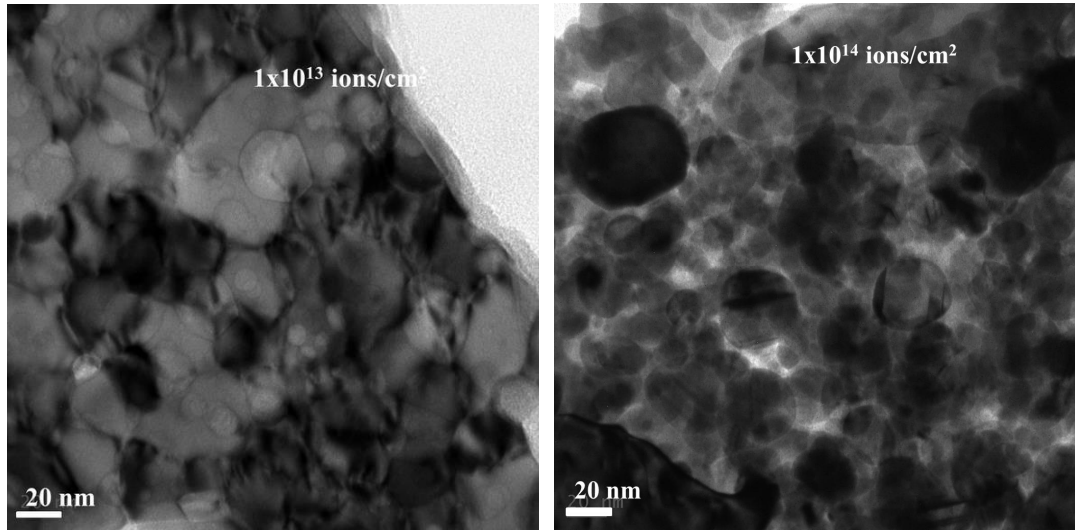


Fig 3.16: TEM image of Set B irradiated Ge NCs samples at 1×10^{13} and 1×10^{14} ions/cm² fluence

From the images of set B ion irradiated samples, it was observed that the Ge NCs are getting smaller in size and at very high fluence of 1×10^{14} ions/cm², the smaller NC density is increased and elongation of few NCs was also observed. Overall the TEM results suggests that the NC size is reducing with the increase in fluence of irradiation and ultimately the NC are becoming partially amorphous from the polycrystalline nature.

When the swift heavy ion traverses through the solid, it loses its energy mostly via electronic processes. The ion energy is deposited into the electronic system of the solid by excitation and ionization, leading to an increase in the local temperature along the ion path. According to SRIM calculations for 120 MeV Ag ions, the electronic energy losses resulting in the energy deposition into the target material are of the order of 17.5 and 12.3 keV/nm in Ge and SiO₂ respectively. Similarly for the 80 MeV Ni ions the S_e is 11 keV/nm and 7.6 keV/nm respectively in Ge and SiO₂. This means that more energy is deposited into Ge compared to SiO₂. The projected ranges of these ions are much greater than that of the film thickness (see Table 3.1). The irradiation leads to the ionization of atoms in the material and the energy is given to the target in the form of thermal energy resulting in heating the target material. This deposited energy will induce a local heating in the target material and the rise in temperature along the ion paths, which is in the time scale of pico seconds. This would be sufficient to break the inter-atomic bonds of atoms inside the Ge NCs during irradiation process [24]. Therefore, a part of Ge will diffuse out from the Ge NCs by breaking their bonds and this leads to a decrease in the size of Ge NCs. This explains why a reduction in size of the NCs is observed at an initial fluence and upon increasing the irradiation fluence a further reduction in the size of Ge NCs occurs as seen from XRD measurements. The shift in the peak position of Ge-Ge optical phonons towards the lower wave number side upon increasing the irradiation fluence also implies the same, that is, a decrease in average size of the NCs. This size reduction of Ge NCs embedded in SiO₂ once again displays the versatility of ion beam irradiation in nanostructuring of materials. From the model given in Ref [17], the critical diameter for the embedded spherical Ge NCs to be melted with the electronic energy loss (S_e) deposited by incident ion is given by the below formula,

$$R_{NP}^{\max} \leq \sqrt{\frac{3 \cdot dE_{NP}^{\text{el}}/dx}{2\pi \cdot H_{NP}^{\text{melting}} \cdot \rho_{NP}}}$$

where R_{NP} is the radius of the nanocrystal, H_{NP}^{melting} is the heat of melting (436 J/g for Ge), dE_{NP}^{el}/dx is the electronic stopping power of Ge NPs and ρ_{NP} is the density of the NC (5.32 g/cm³ for Ge). Therefore for a given electronic stopping power, a spherical nanoparticle melts when the above condition is satisfied. For the 120 MeV Ag and 80 MeV Ni ion irradiation the

critical diameters are estimated to be about 48 nm and 38 nm, respectively. Since the average size of the Ge NCs in Set A unirradiated sample is 31 nm, as seen in the table 3.3 is much smaller than the critical diameter, these NCs would be melted by the ion irradiation. On the other hand the size of Ge NCs in Set B unirradiated sample is 40 nm which is of the order of critical diameter so these NCs are also likely to melt. Actually, the size of the NCs observed from TEM images is even less than these critical diameters in both set A and set B, so the nanocrystals would be melted with the deposited energy. Hence the size reduction and more NCs of smaller sizes are expected and have been observed. The energy deposited by the incident ion must have been used both to heat up the Ge NCs and to melt them, resulting in strong diffusion of the liberated Ge atoms. Then, as the ion fluence increases, there is a chance for small Ge NCs to be nucleated in the vicinity of larger Ge NCs. Consequently, the size reduction of Ge NCs was observed with the increase of ion fluence (as confirmed by XRD and TEM results). The main reason for this is the interaction of tracks formed in SiO₂ during irradiation with the embedded Ge NCs during their melting process. Due to this interaction some of the Ge atoms have diffused from the larger Ge NCs and dissolved into SiO₂. During this process there may be a possibility of interaction of diffusing Ge atoms with the oxygen of SiO₂ to form Ge-O related bonds. Therefore, a further study of the irradiated samples employing X-ray absorption spectroscopy analysis like the one in Ref [25] would be desirable to confirm the presence of the intermixing of Ge NCs with SiO₂ (i.e., formation of any Ge-O bonds).

3.4 Crystallization of Ge implanted SiO₂ films

Ge NCs embedded in SiO₂ matrix have been synthesized by RTA of Ge implanted SiO₂ films. Here, 1 MeV Ge⁺ ions were implanted into thermally grown SiO₂ films with various doses from 1×10^{16} to 1×10^{17} ions/cm² at room temperature. The as-implanted samples were subjected to RTA using a rapid thermal process system at a fixed temperature 800°C for 5 min in N₂ atmosphere (1500 SCCM) to synthesize Ge NCs in SiO₂ matrix. These samples were subsequently characterized by XRD and Raman spectroscopy to understand the formation of Ge NCs in SiO₂ by ion beam synthesis. The XRD results confirm the presence of Ge crystallites in the annealed samples. Raman spectra show the crystalline nature of Ge after annealing. RBS has been used to quantify the concentration of Ge in the SiO₂ matrix.

RBS spectrum of the 1×10^{17} ions/cm² fluence Ge implanted SiO₂ pristine sample has been shown in Fig. 3.17. The spectrum indicates the presence of Si, O and Ge in the sample. The estimated concentration of Ge from the RBS spectrum is around 4at%.

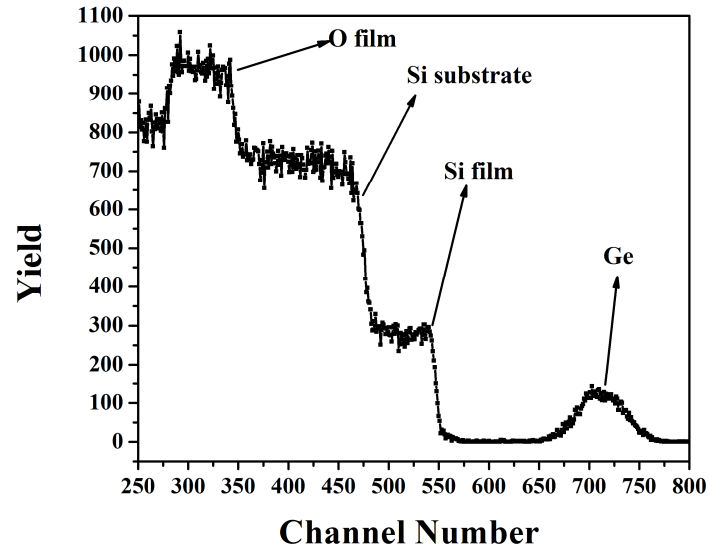


Fig 3.17: RBS spectrum of the Ge as-implanted (1×10^{17} fluence) sample

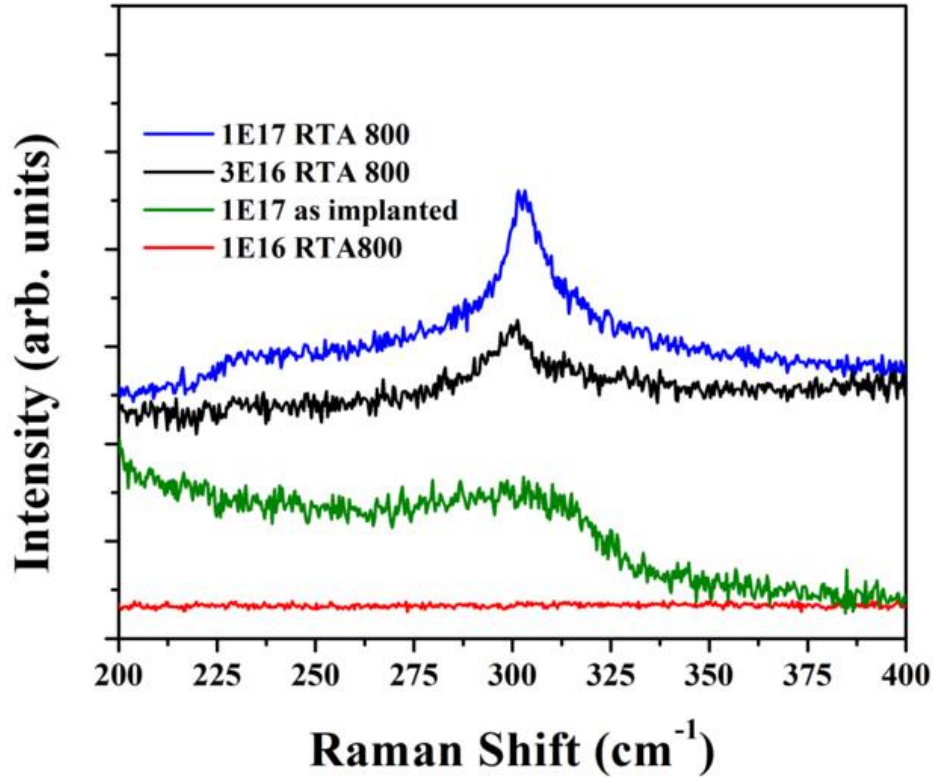


Fig 3.18: Raman spectra of the RTA annealed sample implanted with various fluences

Figure 3.18 shows the Raman spectra of the RTA annealed samples implanted with various fluences. The spectrum of the as implanted sample with fluence 1×10^{17} is also shown in the figure. The sample with this highest implanted fluence has a broad Raman peak corresponding to Ge-Ge optical phonon vibrations which indicates that the Ge is amorphous in the sample. After the annealing at 800°C the peak of Ge-Ge optical phonons becomes sharp and symmetric at 300 cm^{-1} , which indicates that the crystallization occurs and confirms the formation of Ge NCs in SiO₂. The similar kind of sharp peak is observed in the case of other 3×10^{16} fluence annealed sample also. As the implanted Ge was less in fluence compared to 1×10^{17} sample this sample has broad and less intense Raman peak whereas the 1×10^{16} fluence annealed sample did not show any peak before and after annealing. The reason may be that the fluence was not sufficient to form the Ge NCs and also the Ge distribution is broad as the atomic concentration of Ge is low at this fluence. Similar to the Raman analysis we have also performed XRD analysis to see the formation of Ge NCs due to annealing of Ge implanted samples. The XRD pattern of the annealed samples is shown in

figure 3.19. We have not observed any crystalline Ge peaks from the XRD pattern of the as implanted samples and also for the annealed samples of 1×10^{16} fluence implanted sample. The samples with higher fluence implantation after annealing show (101), (113) crystalline peaks of Ge, which indicates the formation of Ge NCs.

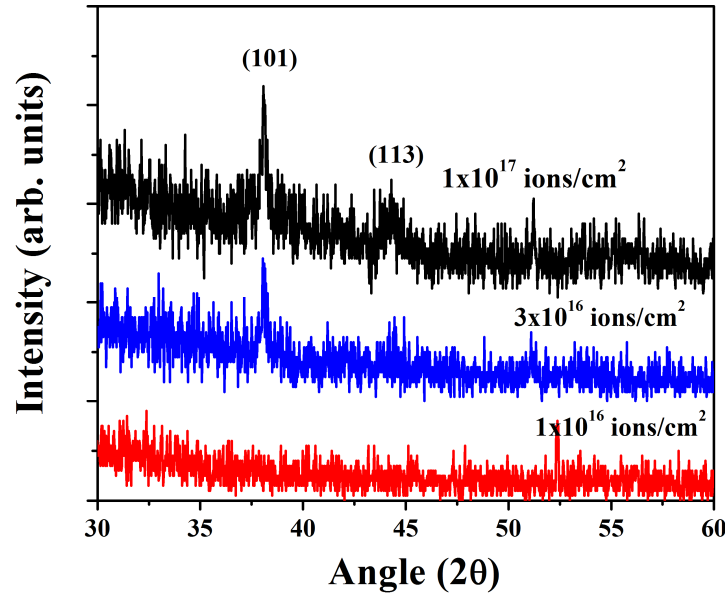


Fig 3.19: XRD pattern of the RTA annealed sample implanted with various fluences

It is observed from the above results that with the increase in implanted ion fluence the chances of formation of Ge NCs as a result of annealing is more and no NCs formation is observed in the low fluence implanted samples as result of RTA. The sharpening of Raman peak of the high fluence annealed sample indicates that Ge NC size in this sample is large in comparison with the medium fluence implanted sample. This increase in particle size happens due to higher diffusivity of Ge atoms at the annealing temperature and also the Ge atomic concentration in the high fluence implanted sample is large enough for the diffusion of Ge atoms in SiO₂ to form the Ge NCs. This mechanism of higher diffusivity results in nucleation of smaller clusters to eventually form bigger NCs. The diffusion of Ge atoms in SiO₂ matrix as a result of annealing leads to nucleation and the growth of Ge NCs. It has been observed that the size of these Ge NCs increases with an increase in implanted ion fluence. It can be possible to tune the size and properties of Ge NCs by choosing the appropriate ion implantation energy, fluence and the annealing temperature.

3.5 Conclusions

In conclusion, we have synthesized Ge nanocrystals embedded in SiO₂ matrix by RF co-sputtering and subsequent rapid thermal annealing process. The effects of 120 MeV Ag and 80 MeV Ni ion irradiation on the size of Ge NCs were investigated and we found that the average size of Ge NCs decreases with increase in irradiation fluence. This was confirmed by the XRD measurements of average size of Ge NCs. The Raman peak shift towards lower wavenumber side with increase in the fluence also suggests a decrease in size of Ge NCs. TEM images confirm the reduction of NC size and it also indicates the partial amorphization of NCs as a result of ion irradiation. The results have been explained using the ion-solid interaction concepts based on the electronic energy deposition by the incident ions inside the target material. This study indicates that the ion irradiation can be used as an interesting tool in nanostructuring various materials to modify their properties for many technologically important applications. Ge NCs have also been synthesized by the ion beam synthesis of 1 MeV Ge implantation into SiO₂ and followed by RTA.

3.6 References

1. H. Takagi, H. Ogawa, Y. Yamazaki, A. Ishizaki, and T. Nakagiri, Appl. Phys. Lett. 56 (1990) 2379.
2. S. Tiwari, F. Rana, H. Hanafi, E. F. Crabbe, and K. Chan, Appl. Phys. Lett. 68 (1996) 1377.
3. K S Zhuravlev, A M Gilinsky and A Yu Kobitsky, Appl. Phys. Lett. 73 (1998) 2962.
4. S H Choi and R G Elliman, Appl. Phys. Lett. 75 (1999) 968
5. L T Canham, Appl. Phys. Lett. 57 (1990) 1046
6. L. Pavesi, L. Dal Negro, C. Mazzoleni, G. Franzo, and F. Priolo, Nature (London) 408 (2000) 440.
7. A Singha, A Roy, D Kabiraj and D Kanjilal Semicond. Sci. Technol. 21, (2006) 1691
8. Y Maeda, Phys. Rev. B 5 (1995) 1658.
9. C J Park, K H Cho, W C Yang, H Y Cho, S H Choi, R G Elliman, J H Han, and C Kim, Appl. Phys. Lett. 88, (2006) 071916.
10. X Ma, W Shi, and B Li Semicond. Sci. Technol. 21, (2006) 713.
11. N Srinivasa Rao, A P Pathak, G Devaraju, V Saikiran, et.al, Solid State Communications 150, (2010) 2122.
12. Eyeru A, Leifeld O, Muller E, Stutz S, Sigg H and Grutzmacher D Thin Solid Films 380, (2000) 246
13. F Boscherini, G Capellini, L Di Gaspare, M De Seta, F Rosei, A Sgarlata, N Motta and S Mobilio Thin Solid Films 380, (2000) 173.
14. U V Desnicaa, M Buljana, P Dubceka, Z Siketica, I Bogdanovic Radovica, S Bernstorff, U Serincanc, R Turanc Nucl. Inst. and Meth. in Res. B 249, (2006) 843.
15. A V Krasheninnikov and K Nordlund J. Appl. Phys. 107, (2010) 071301.

16. A V Krasheninnikov and F Banhart *Nature Materials* 6, (2007) 723.
17. B Schmidt, K H Heinig, A Mücklich, C Akhmadaliev *Nucl. Instrum. Methods Phys. Res. B* 267 (2009) 1345.
18. B Schmidt, A Mücklich, L Rontzsch, K H Heinig *Nucl. Instrum. Methods Phys. Res. B* 257 (2007) 30.
19. I V Antonova, V A Skuratov, V A Volodin, S A Smagulova, D M Marin, A Janse van Vuuren, J Neethling, J Jedrzejewski and I Balberg *J. Phys. D: Appl. Phys.* 45 (2012) 285302.
20. JCPDS Card # 04-0545
21. B.D. Cullity, *Elements of X-ray Diffraction*, second ed., Addison-Wesley, Reading, MA, 1978, 102.
22. X L Wu, T Gao, X M Bao, F Yan, S S Jiang and D Feng *J. Appl. Phys.* 82, (1997) 2704.
23. W K Choi, V Ng, S P Ng, H H Thio, Z X Shen and W S Li *J. Appl. Phys.* 86, (1999) 1398.
24. A Meftah, F Brisard, J M Costantini, E Booryhee, M Hage Ali, M Herviev, J P Stoquert, F Studer and M Toulemonde *Phys. Rev. B* 49, (1994) 12457.
25. L L Araujo, R Giulian, D J Sprouster, C S Schnohr, D J Llewellyn, B Johannessen, A P Byrne and M C Ridgway *Phys. Rev. B* 85, (2012) 235417.

Chapter 4

Synthesis and Characterization of Ge NCs embedded in HfO₂

4.1 Introduction

IC technology is searching for potential materials to replace SiO₂ for further optimization of circuit components. The thickness of SiO₂ layer has reached its limiting values beyond which the leakage current does not allow the device operation. HfO₂ is one of the most promising materials for possible replacement of SiO₂ due to its achievable lower oxide thickness corresponding to the same capacitance value for a thinner SiO₂ dielectric layer [1, 2]. With a high-k dielectric constant, HfO₂ is progressing very effectively to attain capacitance values equivalent to those obtained with low dielectric materials such as SiO₂. This has also an advantage of low leakage current and degradation effects in devices used for flash memory applications. HfO₂ also provides larger current for charging operation in these devices. Thus, HfO₂ is a good candidate dielectric material to improve the device performance in memory applications [3, 4]. Nanocrystals embedded in a dielectric matrix have also potential applications in integrated flash memory devices. The uses of NCs as floating gate memories offer smaller operating voltages and faster write/erase speeds when compared to conventional flash memories [5-7]. Semiconductors as well as metals (Si [8], Ge [9], SiGe [10], Ni [11], Au [12] and Ag [13]) have been considered as capable materials for the charge storage nodes in nanocrystal based floating flash memory devices. Si and Ge NCs are considered to be ideal candidates for memory applications because of their smaller band-gap, high carrier mobilities and larger Bohr exciton radius in comparison with the metal NC based devices. Based on a comparison of Si and Ge effective masses and energy differences between the indirect gaps, the Ge NCs have more technological advantages over Si NCs [14]. The exciton Bohr radius of Ge (24 nm) is much larger than that of Si (5 nm), which indicates that the quantum confinement effects are more prominent in Ge NCs [15]. Also Ge has superior band offset values with longer retention time compared to Si. Thus Ge NCs based materials have garnered great attention as a promising candidate for charge storage device applications as nonvolatile memory [16]. If these NCs can be embedded in a high-k dielectric, it will be an added advantage for the performance of the devices. Hence in recent times Ge NCs embedded in HfO₂ dielectrics have been considered for the memory applications [17]. Ge NCs embedded in other dielectric matrices such as ZrO₂ [18], Al₂O₃ [19] are also studied. To develop the devices based on the Ge NCs in HfO₂, the crystallization kinetics of Ge NCs embedded in the dielectric matrix have to be understood. In general the formation of NCs

embedded in a dielectric matrix includes the deposition of thin films by a physical deposition method and then followed by high temperature annealing. The studies on the formation and growth of Ge NCs embedded in SiO₂ [20-22] are well known whereas the studies on Ge NCs embedded in HfO₂ are limited [23]. There are very few reports available on the formation and growth kinetics of Ge NCs in HfO₂ matrix [24]. The growth and formation of NCs in HfO₂ matrix and the interface effects of Ge/HfO₂ during the formation has to be understood. During the process of Ge NCs synthesis by annealing at high temperatures, the formation of GeO or HfGeO related phases maybe possible. So the understanding of the phenomena of growth and formation of Ge NCs is very important. Swift heavy Ion (SHI) beam irradiation is also an established method for the formation of Ge NCs in the as-deposited amorphous Ge samples by ion beam induced annealing [25]. It is well known that during SHI irradiation process, ion beam mixing in semiconductor and dielectric layers can occur and form a mixed state. Such studies are well known in metal semiconductor systems [26, 27]. However there are no reports available on the formation of HfGeO or HfGeO_x during SHI irradiation of Ge/HfO₂ layers.

Here our aim is to synthesize Ge NCs embedded in HfO₂ and to understand the formation and growth of Ge NCs in HfO₂ matrix. We have prepared trilayered HfO₂/Ge/HfO₂ films on Si substrate by RF sputtering. The as-deposited samples were annealed using RTA at various temperatures to synthesize Ge NCs in HfO₂. XRD and micro-Raman spectroscopy measurements have been employed to confirm the formation of Ge NCs in the annealed samples. SHI irradiation has been used as an alternative method for the formation of Ge NCs in the as-deposited samples. The formation of Ge NCs in HfO₂ matrix as a result of ion irradiation has been studied based on ion beam induced annealing.

4.2 Experimental details

Tri-layered HfO₂/Ge/HfO₂ thin films were fabricated on a p-type Si (100) substrate at room temperature by RF magnetron sputtering of 99.999 % purity HfO₂ and 99.999 % purity Ge targets. The Si substrates were cleaned with acetone, isopropyl alcohol and deionized water before loading into the deposition chamber. The sputtering was performed with an Ar gas. The base pressure during deposition was 5×10^{-6} torr and the working pressure was maintained

at 4.2×10^{-3} torr during the deposition. The schematic of the as deposited sample is shown in figure 4.1.



Fig 4.1: Schematic of the as deposited HfO₂/Ge/HfO₂ sample

The as-deposited samples were annealed through a rapid thermal annealing process at 700 and 800°C for 120 s in N₂ atmosphere (1500 SCCM) in order to form the Ge nanocrystals in HfO₂ dielectric matrix. On the other hand, the as-deposited samples were also irradiated with swift heavy ions of 150 MeV Au and 80 MeV Ni at a fixed fluence of 3×10^{13} ions/cm² as an alternative approach to induce the formation of Ge NCs through ion beam irradiation. The energy losses as well as the ranges of the incident ions inside Ge and HfO₂ systems were calculated using Stopping and Ranges of Ions in Matter (SRIM) simulation code, and the values are given in table 4.1. Irradiation was performed in a high vacuum chamber at the pressure $< 10^{-6}$ torr. The samples were scanned over 1 cm x 1 cm area with the ion beam and a constant current of 1 pA (particle nano-Amp) was maintained throughout the irradiation process. The formation and growth of Ge NCs was studied by using XRD and Raman scattering measurements. XRD measurements were carried out in glancing angle incidence mode with an incidence angle of 1° using a Cu K source (1.5406 Å). The Raman scattering measurements were carried out at room temperature in backscattering mode using 514.5 nm line of an Ar laser as an excitation source. RBS has been employed to estimate the composition of Ge and HfO₂ in the as-deposited sample.

Table 4.1: The values of energy losses and projected ranges of incident ions in Ge ($\rho = 5.35 \text{ g/cm}^3$) and HfO₂ ($\rho = 9.7 \text{ g/cm}^3$).

Incident ion	Energy (MeV)	Electronic energy loss (keV/nm)		Nuclear energy loss (keV/nm)		Range (μm)	
		HfO ₂	Ge	HfO ₂	Ge	HfO ₂	Ge
Au	150	31.8	22.22	0.272	0.492	9	13.6
Ni	80	15.77	10.95	0.024	0.042	8.2	12.4

4.3 Results and discussion

4.3.1 RBS results

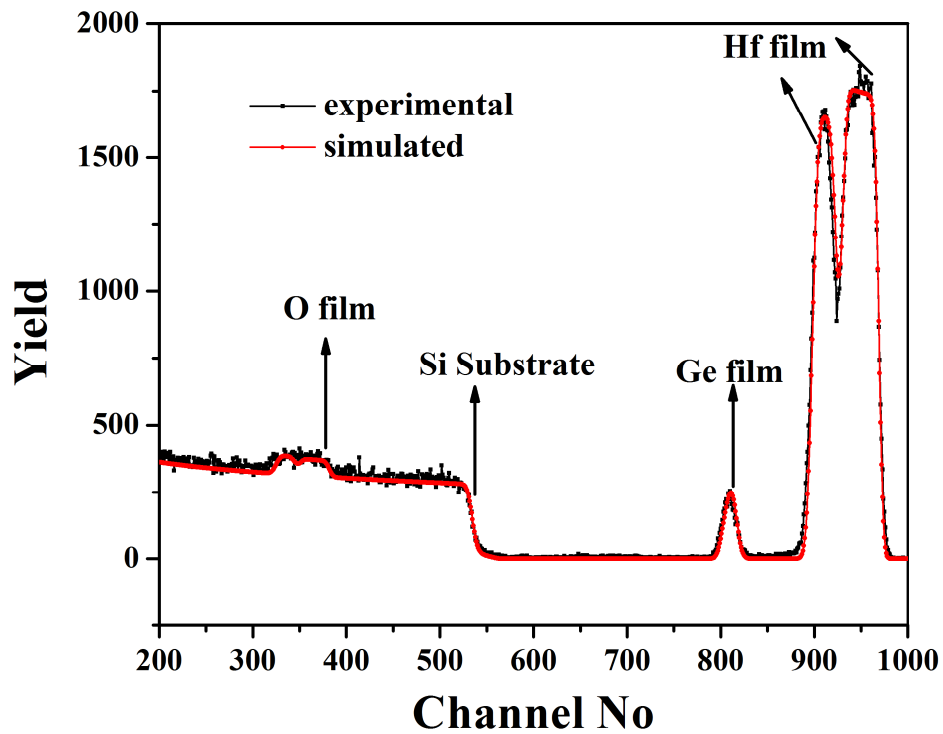


Fig 4.2: RBS spectrum of the as-deposited sample

Figure 4.2 shows the RBS spectrum of as-deposited sample. The sample stoichiometry was estimated by the simulation of the spectrum using the SIMNRA code. The Ge composition in

the as deposited sample is determined to be about 6 at%. The corresponding Ge, Hf and O edges in the spectra are marked.

4.3.2 XRD Results

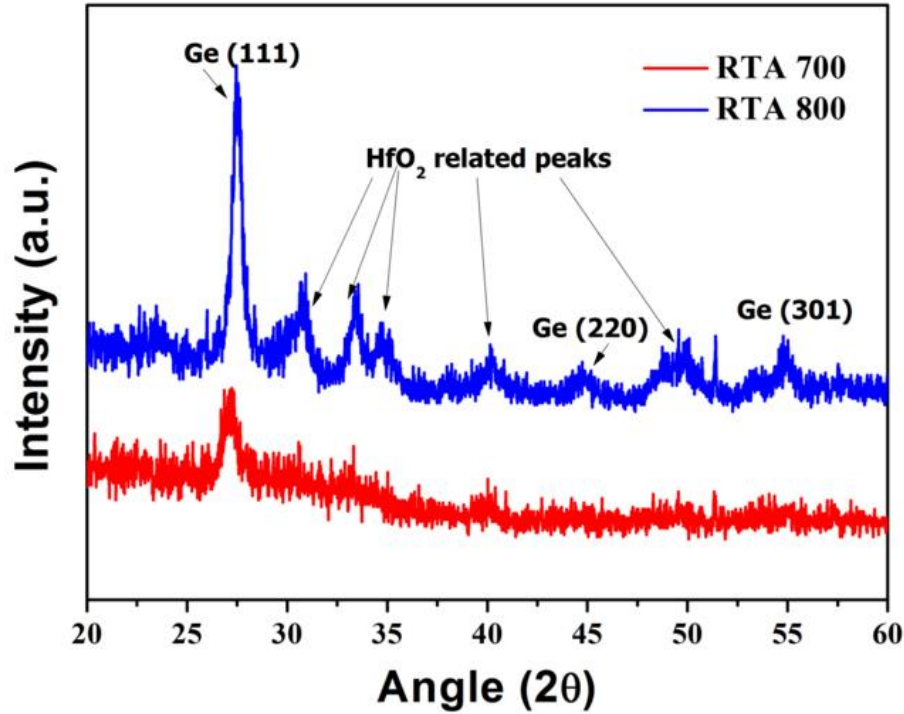


Fig 4.3: XRD pattern of the RTA treated samples

The diffraction patterns of as-deposited, RTA treated samples are presented in Fig 4.3. In case of the as-deposited sample, no noticeable peak is observed, whereas the RTA sample at 700°C and 800°C show various diffraction peaks corresponding to Ge (111), (220) and (311) planes. Apart from crystalline Ge peaks the pattern of RTA 800°C sample also has few more peaks at 2θ values 30.66°, 33.43°, 34.75°, 40.21° and 49.55°. This indicates that the HfO_2 also crystallizes partially due to annealing. The RTA 700°C sample also has few of these peaks, which means the crystallization initiated at that temperature. During the RTA process at high temperature, Ge atoms distributed in the as-deposited sample get higher mobility and crystallize by combining with few more atoms to form a bigger nanocrystal. These Ge NCs were formed by diffusion of Ge atoms or clusters. As observed from the figure, XRD peak

becomes sharper and the full width at half-maximum (FWHM) of the peak is also reduced with the increase of annealing temperature. This indicates that the average size of Ge NC increases with annealing temperature. The measured NC sizes using scherrer's formula are given in table 4.2. As the annealing temperature increases, it was observed that the size of NCs increases because with the increase of temperature, Ge atoms and small nanocrystals get higher mobility and diffuse through the dielectric matrix to form the bigger NCs by joining together. Therefore, an increase in annealing temperature leads to an increase of Ge crystallinity and crystallite size. Thus crystallinity improves with the increase of annealing temperature as seen from the decrease in FWHM and an increase in intensity of the XRD peaks.

The as-deposited samples were irradiated with swift heavy ions of 150 MeV Au and 80 MeV Ni at a fixed fluence of 3×10^{13} ions/cm² as an alternative approach to induce the formation of Ge NCs through ion beam irradiation. The XRD pattern of the SHI irradiated samples is presented in figure 4.4. It is observed that the SHI irradiated samples show diffraction peaks at 26° and 34.6°, which corresponds to crystalline Ge while the as-deposited sample is amorphous and has no peaks. It indicates that the SHI irradiation is inducing the formation of Ge NCs in HfO₂/Ge/HfO₂ trilayered samples. The NC sizes measured are given in table 4.2. The energy deposited by 150 MeV Au ions in both Ge and HfO₂ is larger than the energy deposited by 80 MeV Ni ions. Hence the crystallinity improves and the NC size also increases with the more deposited energy.

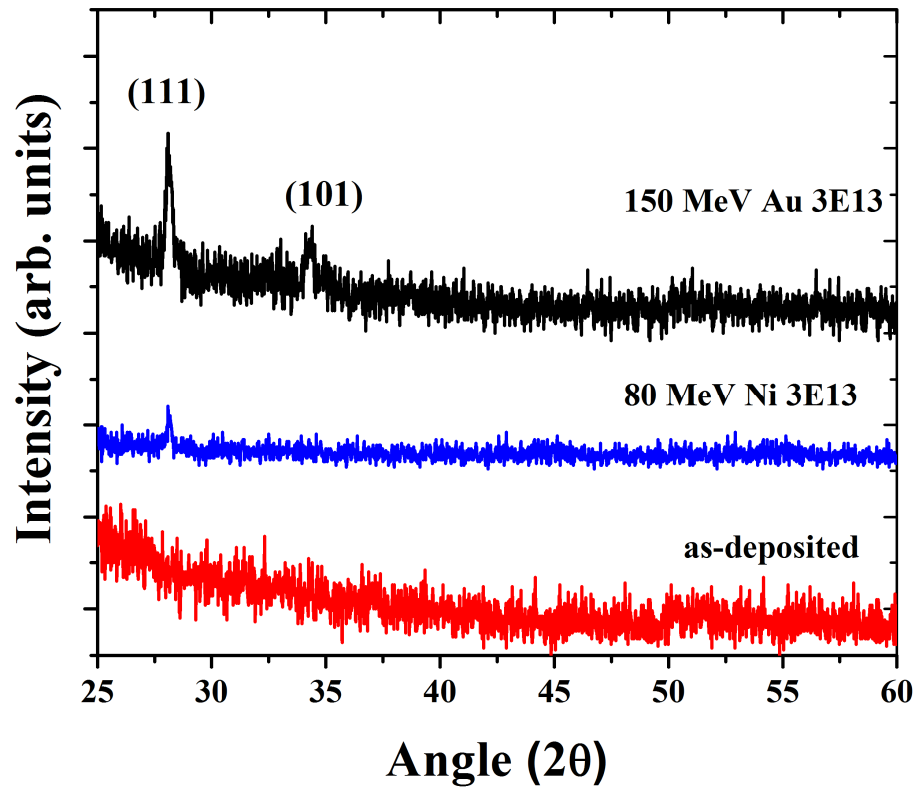


Fig 4.4: XRD pattern of the as-deposited and SHI irradiated samples

Table.4.2: Variation of Ge NC size for various samples

Sample	Ge NC size (nm)
AD	-
RTA 700	11
RTA 800	16
Au 3E13	12
Ni 3E13	9

4.3.3 Raman Results

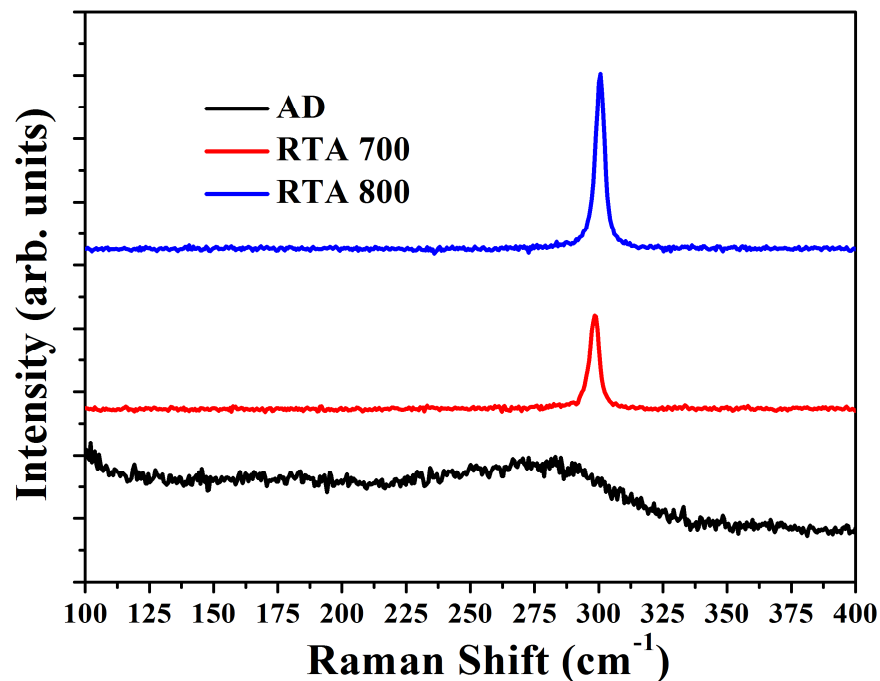


Fig 4.5: Raman spectra of the as-deposited and RTA treated samples

As a complementary technique, we performed Raman spectroscopy measurements to identify the presence of Ge-Ge bonds and their evolution with respect to annealing. Fig. 4.5 shows the Raman spectra for as grown and RTA treated samples. As expected Ge-Ge peak located at 300 cm^{-1} emerged in the spectra after annealing at 700°C and 800°C . We have observed that the peak intensity is low for the sample annealed at 700°C , and increases with increasing temperature. This is clearly a result of the increase in Ge crystallinity with the temperature. One further feature observed in the Raman spectra is the shift in the peak position: the RTA 700 sample has the Ge-Ge peak at 298 cm^{-1} whereas the RTA 800 sample had the peak centered at 300 cm^{-1} . This shift of peak position towards the lower wave number side of the sample annealed at 700°C has been attributed to quantum size effects. It confirms that the size of the NCs in RTA 700 sample is smaller than the size in RTA 800 sample i.e, with the increase in annealing temperature the NC size increases. The annealing temperature of 700°C is at lower end of the temperature range in which Ge crystallization occurs. We would then

expect the sample to have been partially crystallized at this temperature and have an improved crystallinity with increase in temperature. As the temperature increases the FWHM of the peak also decreases, which also indicates that the size of the NC increases with the annealing temperature.

Fig 4.6 shows the Raman spectra of the SHI irradiated samples. It is observed that after the SHI irradiation the Ge-Ge optical phonon peak becomes sharper whereas the un-irradiated sample has a broad peak at 270 cm^{-1} . It can also be seen that the peak position of Ge NCs, shifts towards the lower wavenumber side as the irradiation fluence increases. The values of Ge NCs peak position, the shift of respective peaks, and change in the FWHM of the peak for various fluences of all the samples are given in Table 4.3.

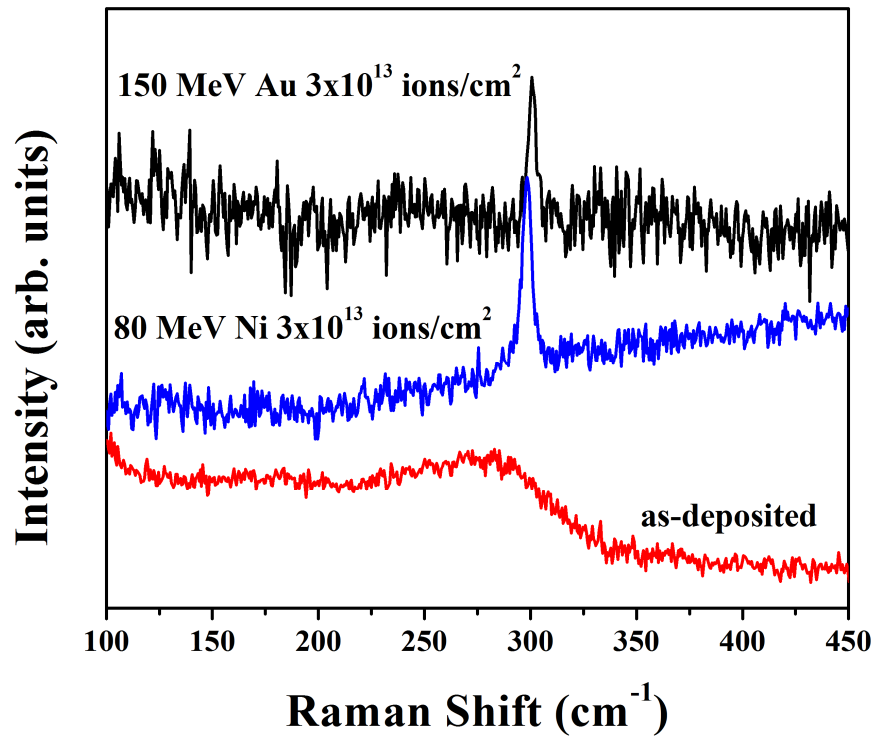


Fig 4.6: Raman spectra of the as-deposited and SHI irradiated samples

Table 4.2: Ge NCs peak position from Raman spectrum, its peak shift and change in FWHM of the peak for various samples

S.No	Sample Details	Ge NCs peak position (cm ⁻¹)	Shift in the peak position from its bulk value (cm ⁻¹)	FWHM of the Ge NCs peak (cm ⁻¹)
1	As deposited	270 (broad one)	-	-
2	RTA 700	298	3	4.2
3	RTA 800	300	1	3.8
4	150 MeV Au 3E13	300	1	3.2
5	80 MeV Ni 3E13	298	3	5.2

4.4 Ion irradiation effects

One can explain the basic mechanism of crystallization and formation of nanocrystals in these samples, under ion-irradiation with the help of thermal spike model [28]. When the swift heavy ion passes through the matter, it loses energy via electronic energy loss (S_e) and nuclear energy loss (S_n). The swift energy transfer makes the system excited and the region where the energy is deposited gets suddenly heated to a very high temperature. The material then, gets modified and transforms to the molten state for a short duration. Thus a large amount of energy is transferred to the target leading to an increase of the lattice temperature above its melting point along the ion path. Eventually, the energy is transferred to the target lattice via electron-phonon coupling. The passage of 150 MeV Au and 80 MeV Ni ions deposits the electronic energy (S_e) of the order of 31.8 keV/nm and 15.8 keV/nm in HfO₂ respectively and similarly 22 keV/nm and 11 keV/nm in Ge. This energy helps the amorphous Ge atoms in the films to combine by diffusion and result in crystallization of Ge. The diffusion of Ge atoms inside HfO₂ results in their agglomeration, leading to formation of Ge NCs. As the 150 MeV Au also deposits a reasonable amount of S_n in both HfO₂ and Ge, so the damage creation is also more in the Au irradiated samples compared to the Ni irradiated ones. The same has been observed in the Raman spectra of the Au irradiated sample which is seen as a shoulder peak at 240cm⁻¹. This is due to the vibrational motion of the oxygen related defects in HfO₂ [29] formed as a result of 150 Au ions irradiation. It has been observed that the size of the Ge NCs in 150 MeV Au irradiated sample is more than the

size of the ones in 80 MeV Ni irradiated at the same fluence, because the growth of the NCs is governed by the deposition of S_e and Au ions deposit more S_e than Ni ions. It will be interesting to see the effects of increase in ion fluence on the growth and modification of NCs. It may be possible to tune the size and properties of Ge NCs by choosing the appropriate energy and ion fluence.

4.5 Conclusions

Tri-layered HfO₂/Ge/HfO₂ thin films were fabricated on Si substrate and the as-deposited samples were annealed using RTA at various temperatures. XRD and micro-Raman spectroscopy measurements were carried out to confirm the formation of Ge NCs in the annealed samples. XRD results reveal the formation of crystalline structure in the annealed samples while the as-deposited samples are amorphous in nature. The average size of the Ge NCs is found to increase with increase in the annealing temperature. According to micro-Raman spectra, the annealed samples exhibit a shift in the peak corresponding to Ge-Ge optical phonon vibrations, which clearly indicates the formation of Ge NCs in HfO₂ matrix. SHI irradiation has been used as an alternative method for the formation of Ge NCs in the as-deposited samples and the XRD and micro-Raman Spectroscopy measurements suggest the presence of Ge NCs in the ion irradiated samples. The formation of Ge NCs in HfO₂ matrix as a result of ion irradiation has been understood based on the S_e deposited by incident ion. This process is also called as ion beam induced annealing.

4.6 References

1. B.Doyle, R. Arghavani, D.barlage, S. data, M. Doczy, J. Kavalieros, A. Murthy, and R. chau, Intel technology, J. 6, 41 (2002)
2. G. D. Wilk and R. M. Wallace, Appl. Phys. Lett. 74, 2854 (1999)
3. T.H. Ng, W.K. Chim, W.K. Choi, V. Ho, L.W. Teo, A.Y. Du, C.H. Tung, Appl. Phys. Lett. 84 (2004) 4385.
4. S. Wang, W. Liu, Appl. Phys. Lett. 86 (2005) 113105.
5. H I Hanafi, S Tiwari, I Khan IEEE Trans Electron Devices 43 (1996) 1553.
6. J K Kim, H J Cheong, Y Kim, J Y Yi, H J Park, Appl Phys Lett 82 (2003) 2527.
7. J Blauwe IEEE Trans Nanotechnol 1(2002) 72677
8. T Hori, T Ohzone, Y Odark, J Hirase IEEE IEDM Tech Dig 92 (1992) 469.
9. K Das, M N Goswami, R Mahapatra, G S Kar, A Dhar, H N Acharya, S Maikap, J H Lee, S K Ray Appl Phys Lett 84 (2004) 1386.
10. D W Kim, T Kim, S K Banerjee IEEE Trans Electron Devices 50 (2003) 1823.
11. Z Tan, S K Samanta, W J Yoo, S Lee Appl Phys Lett 86 (2007) 013107.
12. V. Mikhelashvili, B. Meyler, S. Yoffis, J. Salzman, M. Garbrecht, T. Cohen-Hyams, W. D. Kaplan, and G. Eisenstein Applied Physics Letters 95, (2009) 023104.
13. Q Wanga, Z T Songa, W L Liua, C L Lina, T H Wang Applied Surface Science, 235, (2004) 525.
14. A Singha, A Roy, D Kabiraj and D Kanjilal Semicond. Sci. Technol. 21, (2006) 1691.
15. Y Maeda, Phys. Rev. B 5 (1995) 1658.
16. C J Park, K H Cho, W C Yang, H Y Cho, S H Choi, R G Elliman, J H Han, and C Kim, Appl. Phys. Lett. 88, (2006) 071916.

17. S Das, K Das, R K Singha, A Dhar, S K Ray Appl Phys Lett 91 (2007) 233118.
18. Thin Solid Films 516 (2007) 4126416
19. I D Sharp, Q Xu, D O Yi, C W Yuan, J W Beeman, K M Yu, J W Ager, D C Chrzan, E E Haller J Appl Phys 100 (2006) 114317.
20. N Srinivasa Rao, A P Pathak, G Devaraju, V Saikiran, et.al, Solid State Communications 150, (2010) 2122.
21. Eyeru A, Leifeld O, Muller E, Stutz S, Sigg H and Grutzmacher D Thin Solid Films 380, (2000) 246
22. F Boscherini, G Capellini, L Di Gaspare, M De Seta, F Rosei, A Sgarlata, N Motta and S Mobilio Thin Solid Films 380, (2000) 173. U V Desnicaa, M Buljana, P Dubceka, Z Siketica, I Bogdanovic Radovica, S Bernstorff, U Serincanc, R Turanc Nucl. Inst. and Meth. in Res. B 249, (2006) 843.
23. S. Das, R K Singha, S Manna, S Gangopadhyay, A Dhar, S K Ray J Nanopart Res 13 (2011) 587.
24. S. Das, R K Singha, S Manna, S Gangopadhyay, A Dhar, S K Ray J. Appl. Phys. 108, (2010) 053510.
25. U Serincan, G Kartopu, A Guennes, T G Finstad, R Turan, Y Ekinici, S C Bayliss Semicond. Sc. Technol. 19, (2004) 247. S. Duguay, J. J. Grob, A. Slaoui, Y. Le Gall, and M. Amann-Liess J. Appl. Phys. 97, 104330 (2005).
26. T Som, B Satpati, F Prokert, V Cantelli and D Kabiraj Nanotechnology 17 (2006) 5248.
27. T Som, B Satpati, P V Satyam, D Kabiraj, Ajay Gupta, and N C Mishra Ind. J. Phys. 78 (2004) 815.
28. M. Toulemonde, C. Dufour, E. Paumier, Phys. Rev. B 46 (1992) 14362.
29. Rui Wu, Bo Zhou, Qian Li, ZhenYi Jiang, Wen Bo Wang, Wen Yan Ma and Xiao Dong Zhang J. Phys. D: Appl. Phys. 45 (2012) 125304.

Chapter 5

Synthesis, Characterization and the effects of heavy ion irradiation on Ge/GeO₂ NCs

5.1 Introduction

Ge and Si nanocrystals (NCs) embedded in dielectric matrices have attracted great attention from industry due to their applications in electronic and optoelectronic devices. The structural, optical and electronic properties of Ge and Si NCs have been investigated widely over the last decade [1,2]. Besides these semiconductor NCs, their respective sub-oxides such as SiO_x [3,4] and GeO_x [5] have also attracted enormous research interest because these sub-oxides have great tendency to separate into the semiconducting and oxide phases, and thus can be used to obtain corresponding semiconductor NCs by phase separation [6,7]. Many phase separation methods have been proposed to produce the semiconductor NCs, including thermal annealing [8], laser irradiation [9] and swift heavy ion irradiation [10, 11]. Among these, the ion irradiation has been found to be the most versatile technique for modifying materials at nano-scale [12]. A phase separation of Si NCs and SiO₂ from SiO_x matrix by a high-energy heavy-ion irradiation has been extensively investigated [10, 13-15]. There are also some reports on phase separation of GeO_x into Ge NCs and GeO₂ [16, 17].

In this study, we investigated effects of 80 MeV Ni ions irradiation on GeO₂ NC thin films at various ion fluences and, for the first time, observed the formation of Ge NCs in GeO₂ NCs induced by swift heavy ion irradiation. Grazing incidence X-ray diffraction (GIXRD) results indicate a decrease in average size of GeO₂ NCs with increase in the irradiation fluence. Micro-Raman spectra suggest that swift heavy-ion irradiation results in the formation of Ge semiconductor NCs in the GeO₂ NC thin film. The modifications in size and morphology due to ion irradiation have been clearly seen in the field-emission scanning electron microscopy (FESEM) images. Transmission electron microscopy (TEM) shows the reduction of GeO₂ NC size and the formation of smaller Ge NCs upon ion irradiation, which are consistent with the GIXRD and micro-Raman results.

5.2 Experimental Details

Thin films of GeO₂ NCs were deposited at room temperature on p-doped Si (100) substrates using a RF-magnetron sputtering technique with a target of 99.999% pure Ge (2 inches in diameter). The reactive sputtering was performed at 20 SCCM of argon flow and 20 SCCM of oxygen flow. The RF power was kept at 30W during deposition. Prior to deposition, the

substrates were thoroughly cleaned in an ultrasonic bath with acetone, ethyl alcohol and de-ionized water and then dipped in 10% HF solution to remove any native oxides present. The target to substrate distance during deposition was maintained at 5cm. The as-deposited samples were then irradiated with 80 MeV Ni ions at different fluences ranging from 5×10^{12} to 1×10^{14} ions/cm². The pressure in the irradiation chamber was maintained below 10^{-6} mbar. The ion beam was scanned over 1 cm² of the sample area at a constant beam current of 1 pA. The electronic energy loss (S_e), nuclear energy loss (S_n), and projected ranges of 80 MeV Ni ions in GeO₂ system were calculated by the Stopping and Range of Ions in Matter (SRIM) simulation code and the results are given in Table 1. RBS was used to estimate the composition of Ge and O in the as-deposited samples. GIXRD measurements were performed using Bruker D8 Advance diffractometer with Cu $K\alpha$ source ($\lambda = 0.154$ nm) at an incident angle of 1°. Micro-Raman spectra were obtained using a high resolution confocal micro-Raman spectrometer. The 514.5 nm line of an Ar ion laser was used as an excitation source. The structural morphology was investigated employing FESEM and TEM. Surface morphology of the samples before and after irradiation was also studied using AFM. All measurements were carried out at room temperature.

Table 4.1: The values of energy losses and projected ranges of 80 MeV Ni ions in Ge ($\rho = 5.35$ g/cm³) and GeO₂ ($\rho = 4.25$ g/cm³).

Incident ion	Energy (MeV)	Electronic energy loss (keV/nm)		Nuclear energy loss (keV/nm)		Range (μm)	
		GeO ₂	Ge	GeO ₂	Ge	GeO ₂	Ge
Ni	80	10.62	10.95	0.024	0.042	12	12.4

5.3 Results and discussion

5.3.1 RBS results

Figure 5.1 shows the RBS spectrum of the as-deposited GeO₂ sample. The sample stoichiometry was estimated by the simulation of spectrum using the SIMNRA code [18]. The Ge composition was determined to be about 32 at.%, corresponding to the nominal composition of Ge:O = 1:2, the ratio of Ge to O at% is 0.47.

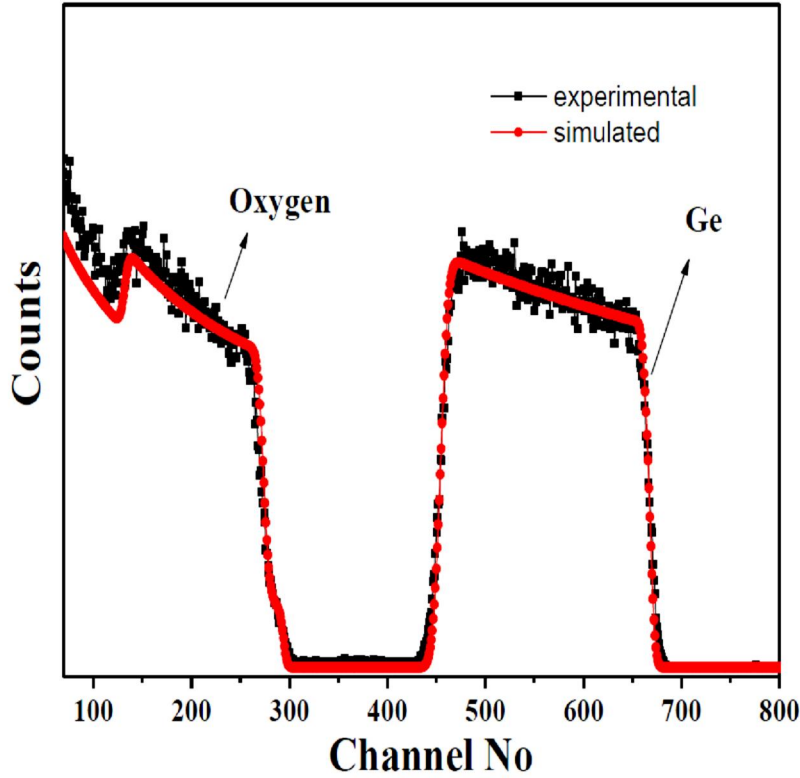


Fig 5.1: RBS spectrum of the as-deposited (unirradiated) sample. A simulated spectrum using the SIMNRA code is added to determine the Ge and O compositions.

5.3.2 XRD results

The presence of GeO₂ NCs in as-deposited sample and their change due to ion irradiation were investigated by GIXRD. The diffraction patterns of the as-deposited and the ion-irradiated samples are presented in Fig 5.2. The assigned diffraction peaks suggest that the GeO₂ samples have a hexagonal structure (JCPDS 04-0545). The average size of GeO₂ NCs was determined from the FWHM of GeO₂ (011) peak at $2\theta = 26^\circ$ by using Scherrer's formula [19] and found to be around 41 nm for as-deposited sample. All the corresponding peaks of hexagonal GeO₂ are not clearly seen in the irradiated samples at higher fluences. At higher fluence (1×10^{14} ions/cm²) only the most prominent peak of GeO₂ (011) at $2\theta = 26^\circ$ is observed. It is observed that the size of GeO₂ NCs decreased with increase in the irradiation fluence (Table 5.2).

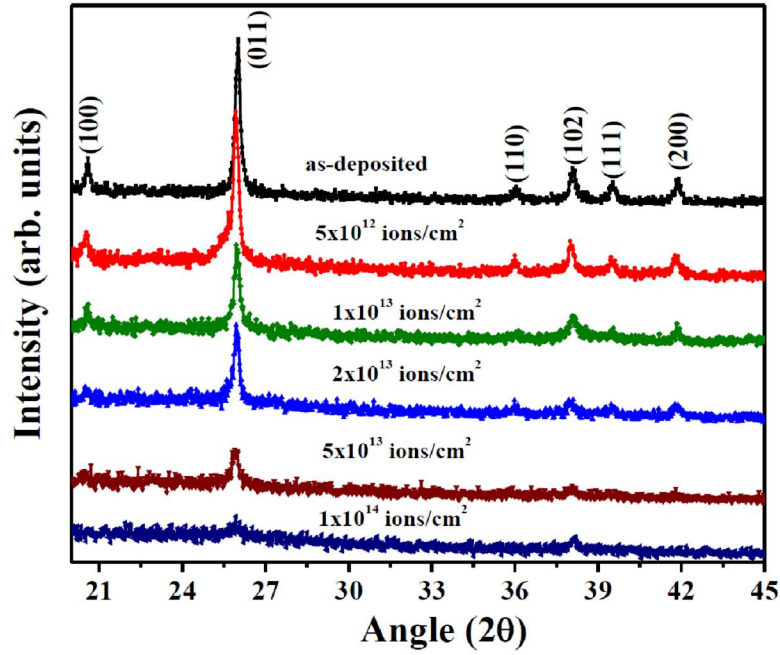


Fig 5.2: GIXRD patterns of the as-deposited and ion-irradiated samples at different fluences.

Table.5.2: Variation of GeO₂ NC size with irradiation fluence of 80 MeV Ni ions

Ion fluence (ions/cm ²)	GeO ₂ NC size (in nm)
0 (Pristine)	41
5×10 ¹²	36
1×10 ¹³	33
2×10 ¹³	28
5×10 ¹³	24
1×10 ¹⁴	20

5.3.3 Micro-Raman Spectroscopy

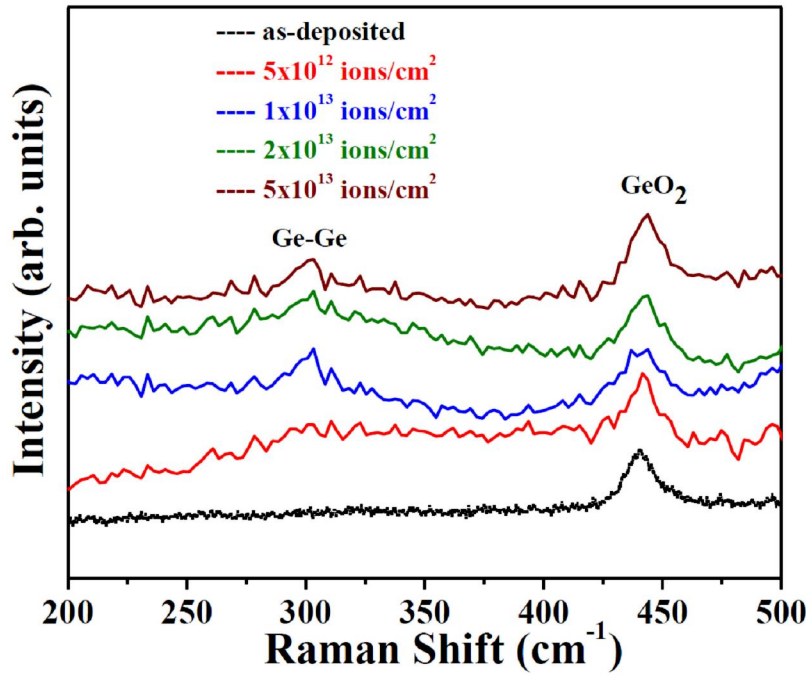


Fig 5.3: Raman spectra of the as-deposited and ion-irradiated samples.

Micro-Raman spectra, due to its sensitivity towards the identification of nanostructures, of the as-deposited and irradiated samples are shown in Fig 5.3. The as-deposited sample exhibits a Raman peak centered at 440 cm^{-1} , corresponding to the optical phonon vibrations of GeO₂ [20]. Interestingly, for the irradiated samples, we have observed an additional peak centered at 300 cm^{-1} (except for $5 \times 10^{12}\text{ ions/cm}^2$) apart from a 440 cm^{-1} peak. This new peak can be attributed to the vibrational modes of Ge-Ge optical phonons [21], reflecting the formation of Ge NCs as a result of ion irradiation. The absence of Ge NC peak at 300 cm^{-1} for $5 \times 10^{12}\text{ ions/cm}^2$ irradiated sample suggests that the GeO₂ NCs are reduced, but not significantly enough to form Ge NCs at this ion fluence. The continued presence of 440 cm^{-1} peak suggests that even after irradiation there exist GeO₂ NCs in addition to few smaller Ge NCs in the irradiated samples.

5.3.4 FESEM-EDS and TEM results

FESEM microstructure images of the as-deposited and ion-irradiated samples at various fluences are shown in Figs. 5.4(a) through 5.4(f). It is evident from the morphologies of the films that the microstructure of the films is strongly dependent on ion fluence. With increase in the irradiation fluence it is clearly observed that the NCs size is reduced. The as-deposited sample has bigger grains and overlap of many NCs is observed [see Fig 5.4(a)]. This is due to the overlapping of the NCs layers on the substrate during deposition at room temperature. Figures 5.4(b) and 5.4(c) for the samples irradiated at 5×10^{12} and 1×10^{13} ions/cm², respectively, show the presence of NCs that are not overlapping as in the case of as-deposited sample. Furthermore, the NC size decreases upon increasing the ion fluence. For the highest fluence irradiated sample at 1×10^{14} ions/cm² [Fig. 5.4(f)], high density of the NCs are observed joining at some regions. The joined particles form a chain-like structure. This feature is actually observed first in the 5×10^{13} ions/cm² sample [Fig. 5.4(e)], but less apparent. At high fluence, the chain formation is present throughout the entire sample. Figure 5.5 shows the energy dispersive X-ray spectroscopy (EDS) spectra obtained at different regions of the 1×10^{14} ions/cm² irradiated sample.

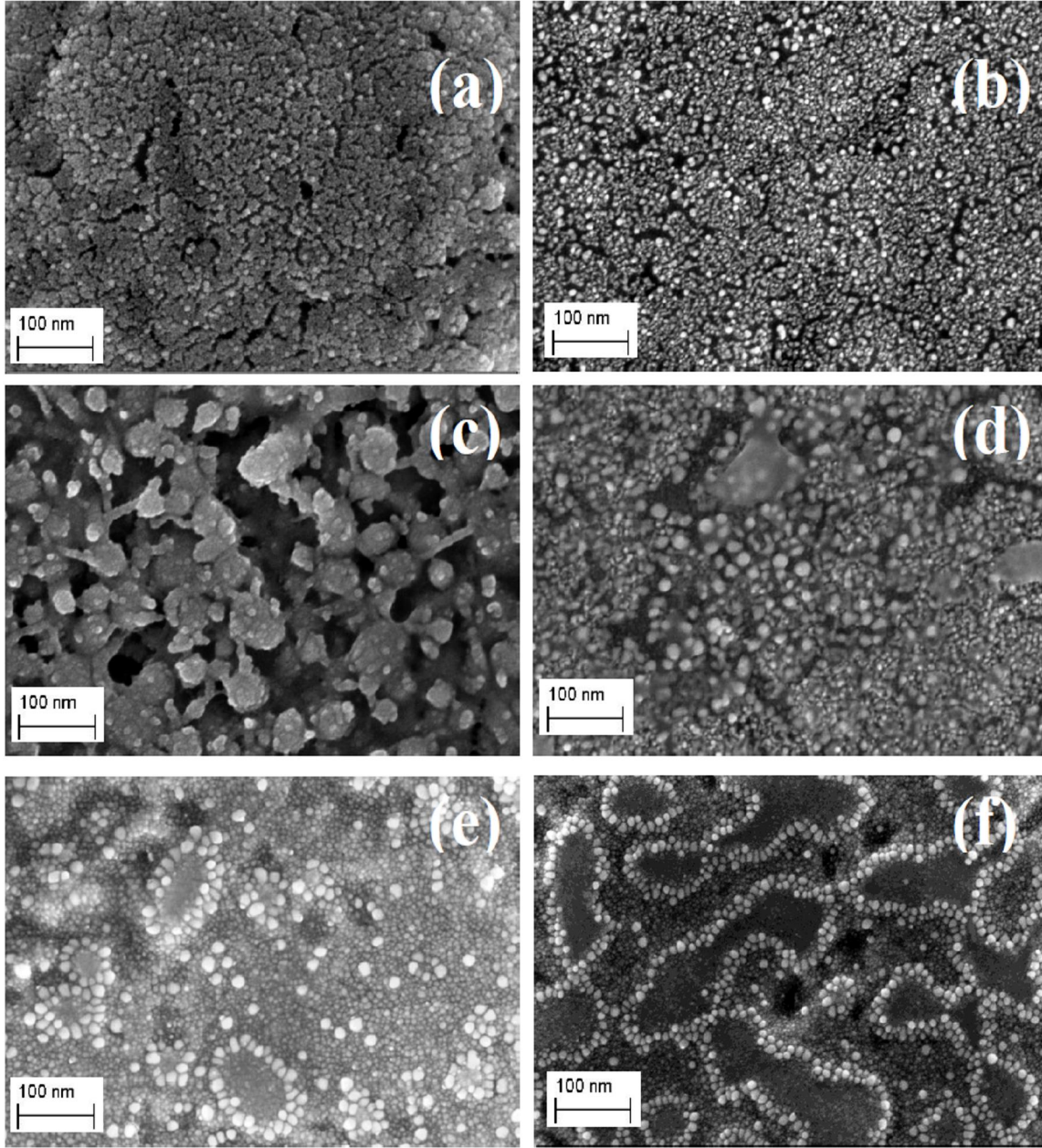


Fig 5.4: FESEM images of (a) as-deposited sample and ion-irradiated samples at (b) 5×10^{12} , (c) 1×10^{13} , (d) 2×10^{13} , (e) 5×10^{13} , and (f) 1×10^{14} ions/cm².

One can clearly see that the oxygen content is higher in the film area on the chain-like structure [Fig. 5.5(a)] than in the area inside the chain structure [Fig. 5.5(b)]. This indicates that the irradiation is creating oxygen deficient regions. The formation of oxygen rich regions has occurred at the rate and expense of oxygen deficient regions as a result of irradiation. The

Ge NCs are present in the oxygen deficient regions, which are formed as a result of ion irradiation. The similar kind of phase separation of Si and SiO₂ from SiO_x was recently reported [6] and the formation of Ge NCs by phase separation of Ge from GeO_x was also studied [11]. This kind of Ge NC formation in the nanocrystalline GeO₂ upon ion irradiation is first of its kind.

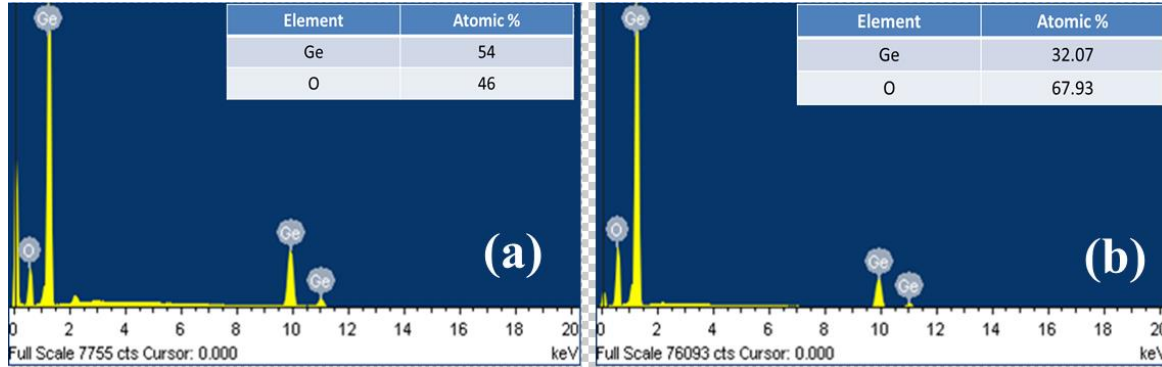


Fig 5.5: EDS spectra of 1×10^{14} ions/cm² irradiated sample (a) from the area inside the chain structure and (b) on the chain like structure.

The oxygen atoms attached to Ge can be transferred by diffusion from one position to another position. The transport of oxygen atoms by diffusion is an important phenomenon during the energy deposition process. This requires some amount of activation energy and the lowest energy required for the oxygen atom to diffuse in Ge for one single jump to a neighboring site is 2.02 eV [22]. When the swift heavy ion traverses through the solid, it loses its energy mostly via electronic energy loss. The ion energy is deposited into the electronic system of the solid through excitation and ionization, which leads to an increase in temperature along the ion path. The deposited electronic energy is sufficient to trigger the oxygen transfer. Because of the dissociation of oxygen from GeO₂, the oxygen deficient-regions are formed in the sample and the dissociated oxygen would reside in the interstitial and/or defect sites and be responsible for the oxygen-rich regions. Hence the oxygen rich regions have occurred at the expense of oxygen deficient regions as a result of diffusion of oxygen due to the huge amount of electronic energy deposited by irradiating ion. Free Ge atoms after the dissociation of oxygen will agglomerate together to nucleate the Ge NCs with the increase in irradiation

fluence. The schematic of Ge-Ge bond formation at the expense of Ge-O bond dissociation is depicted in Fig 5.6.

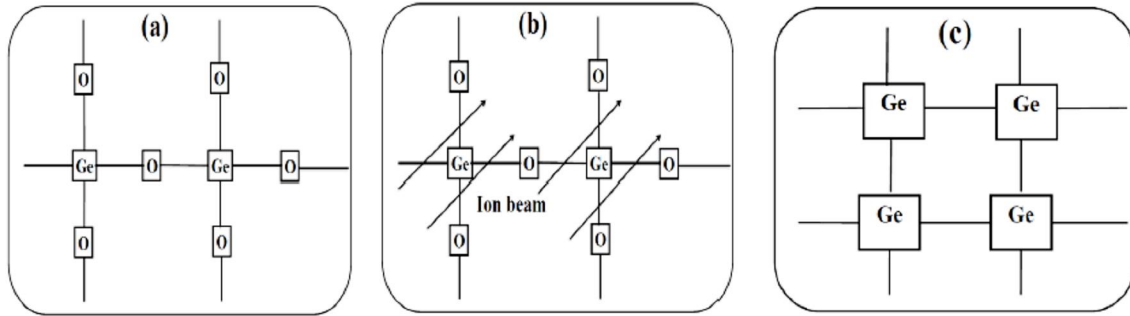


Fig 5.6: Schematic of the interaction between Ni ions and GeO₂ structure: (a) Ge-O bondings before ion irradiation, (b) oxygen removal due to energetic Ni ion beam, and (c) Ge-Ge formation at the expense of Ge-O upon ion irradiation.

It shows that as a result of irradiation in GeO₂ NCs layers, oxygen-deficient regions are generated and Ge NCs are formed within and surroundings of GeO₂. The deposited energy in the material causes the removal of oxygen and the transfer from one position to another position. This energy is sufficient to break the O-Ge-O bond and removes oxygen from GeO₂. The removed oxygen occupies an interstitial site and/or defect site and the Ge-Ge bond will form as replacement of Ge-O bond. This is similar to the work of Hosono *et.al* [23] who have reported the formation of Ge NCs by implantation of 1.5 MeV protons into GeO₂-SiO₂ glasses.

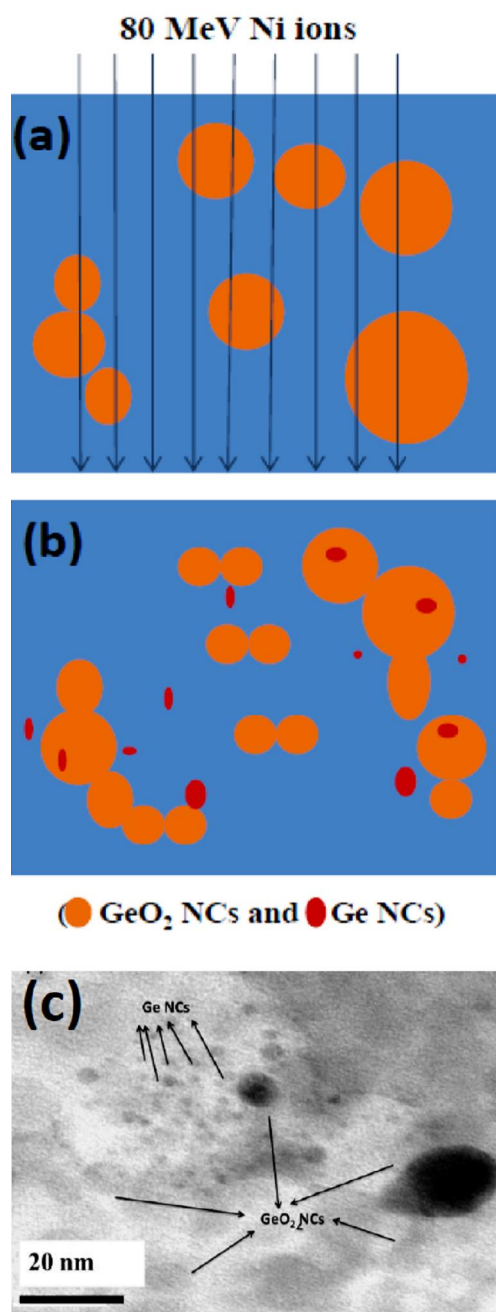


Fig 5.7: Schematic of the formation of Ge NCs from GeO₂ NCs upon ion irradiation: (a) GeO₂ NCs before ion irradiation, (b) size reduction of GeO₂ NCs and formation of Ge NCs after ion irradiation. (c) TEM image of 1×10^{14} ions/cm² irradiated sample shows few nm sized Ge NCs.

Indeed, when the swift heavy ions enter the target, a wealth of complex defects and/or charged configurations are generated along the collision cascade [24]. The defects and their interactions under swift heavy ion irradiation can largely influence the structural and physical properties of the target system. The precipitation mechanism of Ge NCs depends on the local density of electrons and holes created by the deposited electronic energy during irradiation and the subsequent diffusion of Ge atoms to form the Ge NCs. The deposited energy leads to the generation of electron-hole pairs and they interact with the structural defects or impurities. The diffusion of oxygen atoms also modifies the composition and leads to the formation of Ge NCs in the vicinities of GeO₂ NCs. The Figures 5.7(a) and 5.7(b) depicts the formation of Ge NCs in the ion irradiated nanocrystalline GeO₂ films. Thus the transfer of electronic energy to the target matrix by ion irradiation is large enough to induce a separation of Ge atoms through oxide and to allow the formation of Ge NCs by the agglomeration of Ge atoms. In this way the ion irradiation contributes to the growth of smaller size Ge nanocrystals within nanocrystalline GeO₂. Due to this separation, the size of GeO₂ nanocrystals decreases. This is consistent with the observed reduction in the average GeO₂ NC size from the XRD results. Figure 5.7(c) shows TEM image of the 1×10^{14} ions/cm² fluence irradiated sample, which gives a direct evidence of the presence of very small Ge NCs in the vicinity of GeO₂. The presence of such small NCs was not observed in the as-deposited sample. The formation of Ge NCs in GeO₂ layers irradiated at different fluences is revealed in the Raman spectra shown in Fig. 5.3, which is also confirmed from the TEM analysis discussed above. Hence combined Raman spectroscopy and TEM analysis confirms the existence of small Ge NCs in the surroundings of already existing GeO₂ NCs.

5.3.5 AFM results

Figure 5.8 shows the surface morphology of as deposited and irradiated GeO₂ NCs films using AFM. From these images only a small difference in surface roughness has been observed. However, a significant change in the particle size with increase in fluence of irradiation was observed.

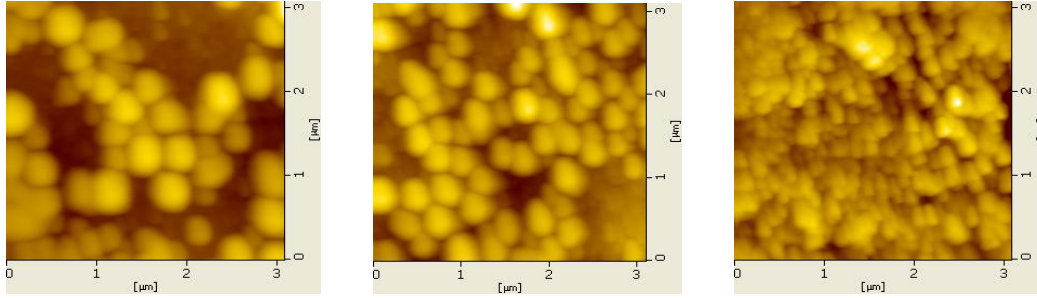


Fig 5.8: AFM images of unirradiated and irradiated (at fluences 1×10^{13} and 2×10^{13} ions/cm²) samples.

5.4 Conclusions

We have investigated the effects of 80 MeV Ni ion irradiation with different ion fluences on thin films of GeO₂ nanocrystals fabricated by a RF magnetron sputtering. The change in particle size with ion fluence has been discussed. The average size of GeO₂ NCs is found to decrease with increase in the irradiation fluence. A removal of oxygen and formation of smaller Ge NCs from GeO₂ takes place during ion irradiation and hence a decrease in the NC size has been observed due to irradiation. Surface morphology and modifications induced by ion irradiation was clearly understood from FESEM microstructures. Micro-Raman spectroscopy studies show clearly the formation of Ge NCs with the increase of irradiation fluence. From the combined micro-Raman and TEM observations of irradiated samples, we see the formation of Ge NCs close to the GeO₂ rich regions when irradiated with 80 MeV Ni ions. This observation leads to the conclusion that the deposition of electronic energy by irradiated ions plays an essential role in the formation of Ge NCs. As a result of irradiation, with the deposited electronic energy, some of the Ge-atoms lose their bonds with the oxide network and agglomerate to form the structure of Ge NCs. These results have been explained by the diffusion of oxygen in Ge with the electronic energy deposition by the incident ions.

5.5 References

1. K D Hirschmann, L Tsybeskov, S P Dattagupta and P M Fauchet, *Nature* 384 (1996) 338.
2. L Pavesi, L Negro, C Mazzoleni, G Franz`o and F Priolo, *Nature* 408, (2000) 440.
3. P Cuony, M Marending, D T L Alexander, M Boccard, G Bugnon, M Despeisse and C Ballif, *Appl. Phys. Lett.* 97, (2010) 213502.
4. P Buehlmann, J Bailat, D Dominé, A Billet, F Meillaud, A Feltrin and C Ballif, *Appl. Phys. Lett.* 91, (2007) 143505.
5. M Ardyanian, H Rinnert, X Devaux and M Vergnat, *Appl. Phys. Lett.* 89 (2006) 11902.
6. W M Arnoldbik, N Tomozelu, E D Van Hattum, R W Lof, A M Vredenberg and F Habriken, *Phys. Rev. B* 71 (2005) 125329.
7. Y Batra, D Kabiraj and D Kanjilal, *Solid State Commun.* 143, (2007) 213.
8. Y Batra, D kabiraj and D Kanjilal, *J. Nanosci, Nanotech.* 8 (2008) 4081.
9. A Janotta, Y Dikce, M Schmidt, C Eisele, M Stutzmann, M Luysberg and L Houben, *J. Appl. Phys.* 95 (2004) 4060.
10. P S Chaudhari, T M Bhave, D Kanjilal and S V Bhaoraskar, *J. Appl. Phys.* 93 (2003) 3486.
11. Y Batra, D Kabiraj, S Kumar and D Kanjilal, *J. Phys. D: Appl. Phys.* **40** (2007) 4568.
12. A V Krashenninnikov and K Nordlund, *J. Appl. Phys.* **107**, (2010) 071301.
13. D Rodichev, Ph Lavallard, E Doryhee, A Slaoui, J Perriere, M Gandias and Y Wang, *Nucl. Instrum. Methods. Phys. B* 107 (1996) 259
14. P S Chaudhari, T M Bhave, R Pasricha, F Singh, D Kanjilal and SV Bhoraskar, *Nucl. Instrum. Methods. Phys. B* 239 (2005) 185.
15. W M Arnoldbik, D Knoesenb, N Tomozeiua and F H P M Habrakena, *Nucl. Instrum. Methods. Phys. B* 258 (2007) 199.

16. Y Batra, D Kabiraj, S Kumar and D Kanjilal, Surface Coatings and Tech. 203 (2009) 2415.
17. K Vijayarangamuthu, S Rath, D Kabiraj, D K Avasthi, P K Kulriya, V N Singh and B R Mehta, J. Vac. Sci. Technol. A **27** (2009) 731.
18. O Adeoya, M H Ali, J C Muller and P Siffert, Appl. Phys. Lett. 50 (1987) 1736.
19. B D Cullity, Elements of X-ray Diffraction, 2nd Ed., Addison-Wesley, Reading, MA, 1978, 102.
20. T Sato and J Suda, J. Phys. Soc. Jap. 67 (1998) 3809.
21. M Fuji, S Hayashi and K Yamamoto, Jpn. J. Appl. Phys. 30 (1991) 687.
22. C Hass J. Phys. Chem. Solids. 15 (1960) 108.
23. H Hosono, K Kawamura, Y Kameshima, H Kawazoe, N Matsunami and K Muta, J. Appl. Phys. 82 (1997) 4232.
24. R E de Lamaestre, H Bea, H Bernas, J Belloni and J L Marignier Phys. Rev. B. 76 (2007) 205431.

Chapter 6

Swift heavy ion irradiation effects on Si nanoparticles

6.1 Introduction

Silicon is the second most commonly occurring element in the earth's crust, after oxygen. It is also the most widely used material for solar cell applications. As of today more than 90% of the world's solar photovoltaic modules are produced in silicon wafers. So studies on silicon became very important for various applications. Bulk silicon is a very standard material for semiconductor processing and devices. As it is an indirect band gap material, for a long time it has been considered as unsuitable for the applications in optoelectronics and photonics devices. More and more efforts are being concentrated on the studies of Si NCs based devices due to their photoluminescence properties observed in early nineties [1,2]. The research on Si nanoparticles (NPs) has received considerable attention due to their potential applications in many different fields [3, 4]. The use of embedded NPs or quantum dots in a matrix of silicon oxide [5], nitride, or carbide [6] has many potential applications in third generation tandem solar cell designs [7], optoelectronics, microelectronics and biomedical areas [8,9]. Various methods have been employed for the growth of Si NCs in a dielectric matrix, which include e-beam evaporation [10], Plasma Enhanced chemical vapor deposition [11], silicon rich oxide phase separation by sputtering [12], laser ablation [13], Si implantation into SiO₂ layers [14], Atom beam co-sputtering [15] and solution synthesis [16]. Laser ablation/irradiation has become one of the versatile methods to prepare nanoparticles from solid targets in either gas or liquid media [17]. The laser generated plasma formed during ablation and confined within the liquid media is an ideal environment to promote non-equilibrium processes, which in turn can facilitate the formation of nano-scale structures [18]. The size and shape of the NCs depend on the conditions of the laser ablation such as energy, time of ablation and the solvents used during process. Here we present a study on the formation of Si-NPs by picosecond laser ablation of Si wafer in acetone. The Si nanoparticles thus obtained by laser ablation of Si wafer were used to understand the effects of swift heavy ions irradiation at various fluences. G A Kachurin et.al, [19] have reported the growth of light emitting Si quantum dots in Silica layers by first low energy implantation and then followed by irradiation with swift heavy ions. P S Chaudari et.al, [20], have carried out studies of swift heavy ion induced growth of nanocrystalline silicon in silicon oxide. Both the above mentioned authors have reported the photoluminescence properties of nanocrystals in silicon oxide matrix. Rodichev et.al, [21] observed 2-3 nm size spots after irradiation with 575 MeV

Ni and 863 MeV Pb ions. The spots were attributed to Si NCs formed in the ion tracks of swift heavy ions. SiO_x phase separation into Si and SiO₂ was observed under 50 MeV Cu ion irradiation [22], 120 MeV Ni ion irradiation [23], and it was attributed to the phase separation in the ion tracks by the process of spinodal decomposition.

Here our aim is to study the effects of 150 MeV Au ions irradiation on the size and shape of Si NPs obtained by using laser ablation of Si wafer in acetone. The fluence dependence on the size and shape of the Si NPs was studied, which no one has elaborated in detail. The samples have been characterized by micro Raman spectroscopy, TEM and FESEM before and after 150 MeV Au ions irradiation for understanding the modifications induced by ion irradiation.

6.2 Experimental Details

This study has been performed using a chirped pulse amplified (CPA) Ti: sapphire laser system (LEGEND, Coherent) delivering nearly bandwidth limited laser pulses (~2 ps, 1 kHz repetition rate) at 800 nm as an excitation source. The target was placed into a Pyrex cell and covered by a layer of absolute liquid (acetone). The beam waist estimated (in air) at the focus was ~30 μ m. The targets were placed normal to the laser beam on a motorized X-Y stage which was controlled by ESP 300 motion controller. The motorized stages (Newport) were translated to write periodic line pattern on the substrates, at a separation of ~50 μ m. Pulse energies used were typically 120 μ J and the time of exposure was ~60 minutes. The wafer used in this study was p-type Si of resistivity 10 Ohm-cm oriented in (100) direction. The Raman measurements were carried out at room temperature using 514.5 nm line of an Ar ion laser as an excitation source. The morphology of the laser ablated wafer was studied using FESEM. The images of Si NCs have been obtained by using advanced TEM with electron-accelerating voltage of 200 kV. The ablated liquid was drop casted on to TEM grid and Si/glass substrate for TEM and FESEM measurements, respectively. FESEM measurements were also performed on the irradiated Si wafer. The laser ablated Si wafers and the drop casted TEM grids were directly used for SHI irradiation with 150 MeV Au ions, at room temperature. The fluence was varied from 1×10^{13} to 1×10^{14} ions/cm². The range and the electronic energy loss associated with the 150 MeV Au ions in Si/SiO₂ are calculated using a simulation code SRIM and listed in the table 6.1.

Table 6.1: The range and the electronic energy loss of 150 MeV ions in Si and SiO₂

Incident ion	Energy (MeV)	Electronic energy loss (keV/nm)		Nuclear energy loss (keV/nm)		Range (μm)	
		SiO ₂	Si	SiO ₂	Si	SiO ₂	Si
Au	150 MeV	16.31	14.43	0.182	0.179	17	18.5

6.3 Results and Discussion

6.3.1 Raman Results

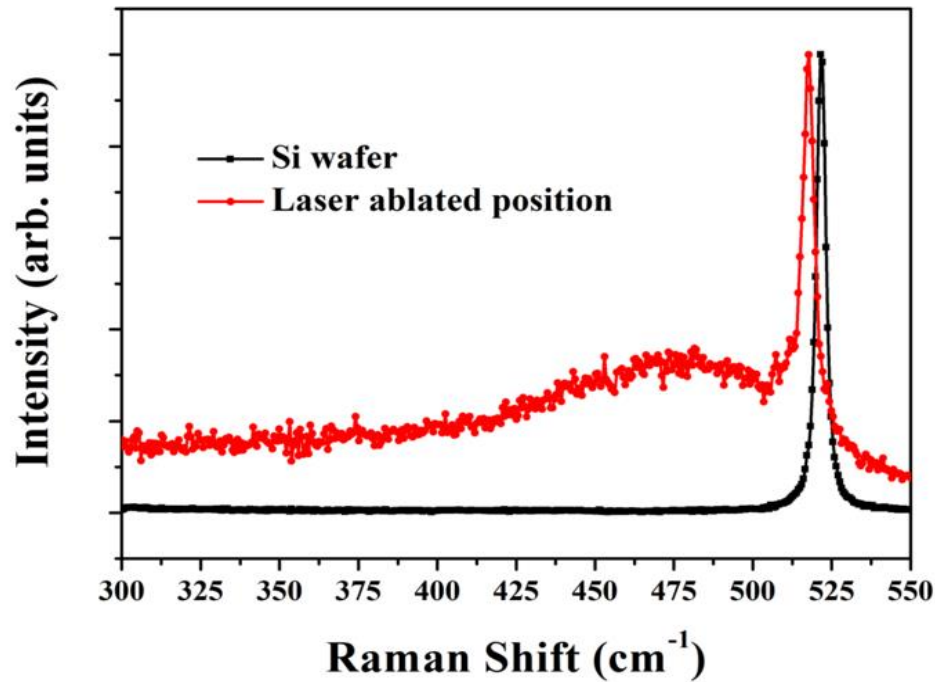


Fig 6.1: Microraman spectra of laser ablated Si wafer

Raman scattering measurements provide an evidence for the presence of Si NPs. Figure 6.1 shows the room temperature Raman spectra of the laser irradiated and un-irradiated Si wafer samples. The sharp peak at 521 cm⁻¹ corresponds to the bulk Si and it is due to the optical phonon modes of the Si substrate and it is symmetric near 521 cm⁻¹ [24]. However, the spectrum obtained from laser irradiated area has an asymmetric peak around 517 cm⁻¹. This peak is more asymmetric around its peak position towards lower wavenumber side.

According to the confinement effects of optical phonons in low dimensional structures the asymmetry in the peak position and the broadening towards the lower wavenumber side confirm the formation of NPs at the irradiated site. The broad peak centered around 480 cm^{-1} indicates the amorphous nature of the Si wafer at the laser ablated area [25]. This peak also corresponds to the SiO_2 vibrational modes. This also suggests that at the amorphized area of the Si wafer, the NPs are getting oxidized and there was a formation of SiO_2 . The size of the Si NPs can be estimated from the shift in the peak position from the bulk value and width of the peak. Figure 6.2 shows the Raman spectra of the Si NPs in acetone which strongly signifies the presence of the Si NPs in acetone after the laser ablation of Si wafer in acetone.

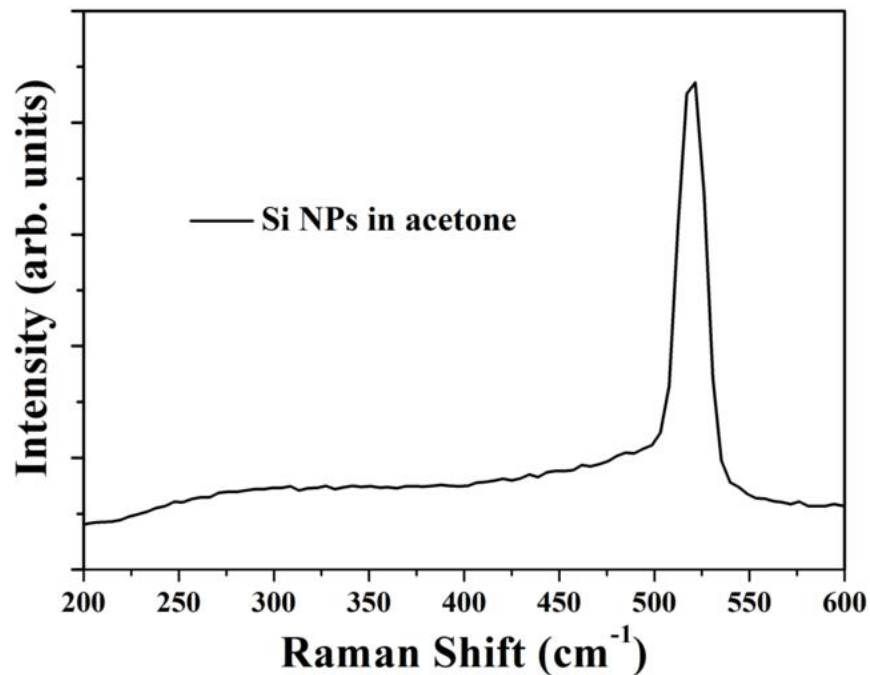


Fig 6.2: Micro raman spectra of the as prepared Si NPs in acetone (dropcasted on glass plate)

The Raman spectra of the 150 MeV Au ions irradiated samples at various fluences is shown in figure 6.3. It indicates that the Raman spectra is similar to the one obtained from the laser ablated area of Si wafer. All the spectra have the peak position centered at 517 cm^{-1} and a broad shoulder towards the lower wave number side. It was observed that, with the increase in irradiation fluence the full width at half maximum (FWHM) of the peak increases and it

signifies that the NP size decreases with the increase in fluence [26]. The broadening of the peak at 521 cm^{-1} after 150 MeV Au ion irradiation and the significant increase of the peak width at 480 cm^{-1} suggest that a further amorphization of the laser ablated Si wafer takes place upon ion irradiation. The values of peak position, shifts in the peak position from its bulk value and FWHM of the peak are given in table 6.2.

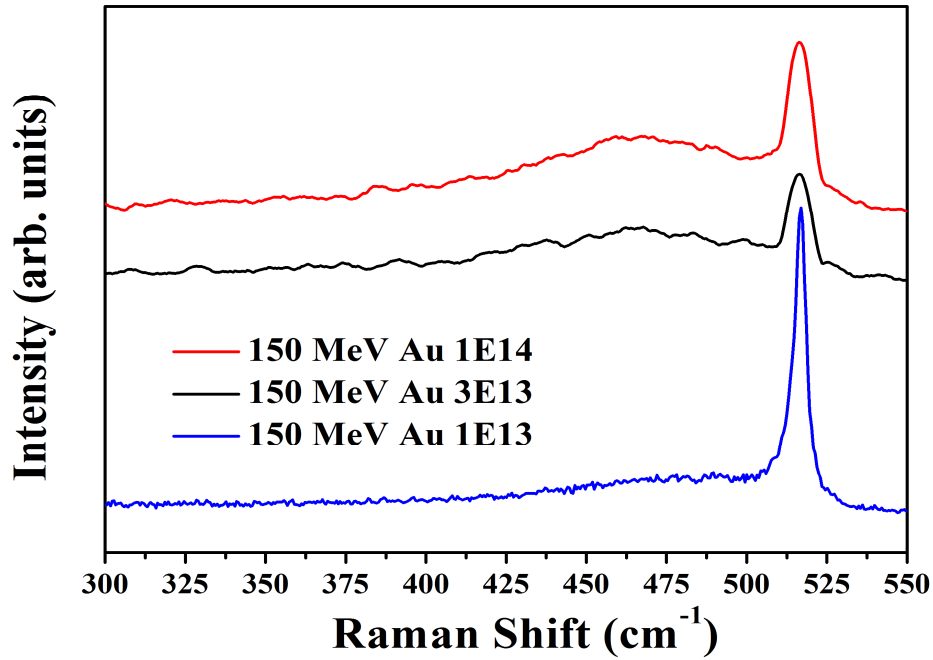


Fig 6.3: Microraman spectra of the as prepared and 150 MeV Au ions irradiated (at different fluences) Si NPs

Table 6.2: Si NPs peak position from Raman spectrum, its peak shift and change in FWHM of the peak for various fluences of 150 MeV Au ion irradiation.

S.No	Sample with irradiation fluence	peak position (cm^{-1})	Shift in the peak position from its bulk value (cm^{-1})	FWHM of the peak (cm^{-1})
1	Si wafer	521	---	3.31
2	Laser ablated Si	517.5	3.5	4.24
3	150 MeV Au 1E13	516.6	4.5	4.26
4	150 MeV Au 3E13	516	5	5.39
5	150 MeV Au 1E14	516	5	5.93

6.3.2 FESEM

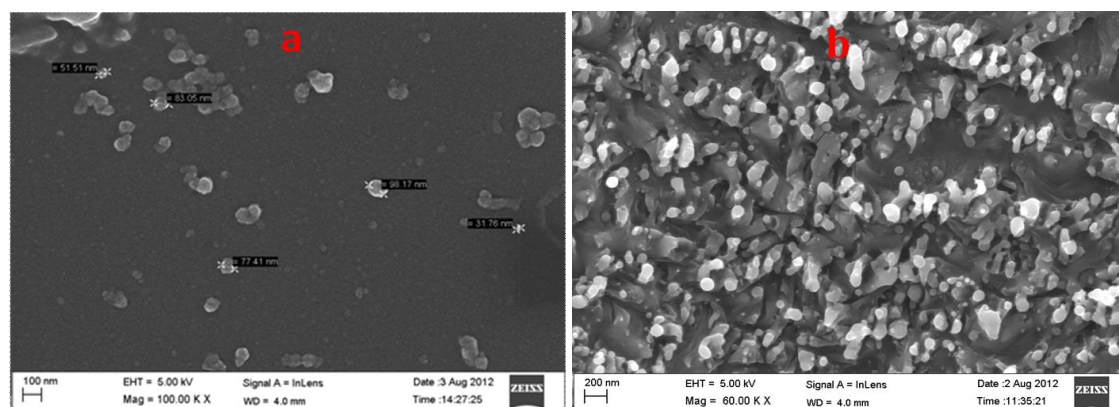


Fig 6.4: FESEM images of laser ablated Si (a) from the liquid deposited on glass plate (b) directly from ablated position of wafer.

Figure 6.4 shows the corresponding FESEM image of the dropcasted solution on glass plate [fig.6.4 (a)] and laser ablated spot of single crystalline Si wafer [fig.6.4 (b)]. It is evident from the image that there was formation of Si NPs at the laser irradiated area of the wafer and in the liquid. The same type of NPs were not observed in the unirradiated area. The density of these particles is also very high. Moreover, these particles were found to be self organized and aligned along the pattern formed in laser irradiation spot (similar to laser induced periodic surface structures) and in the direction of incident laser beam.

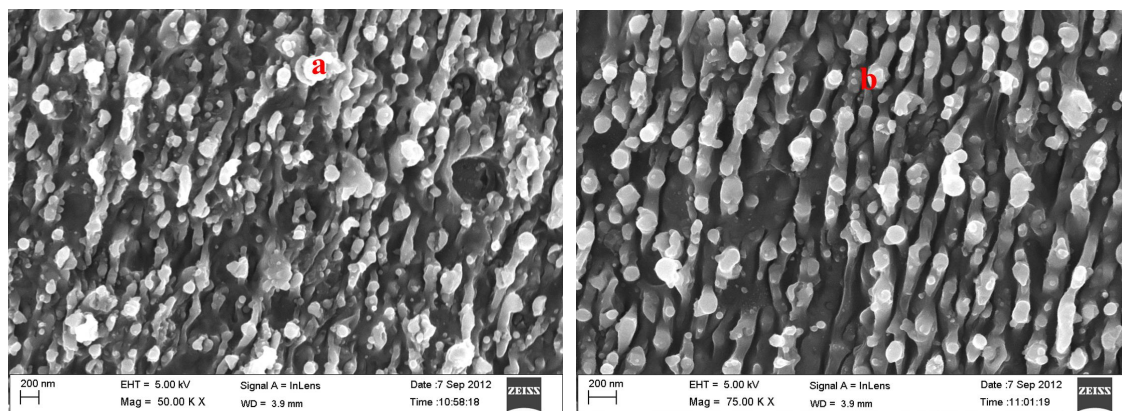


Fig 6.5: FESEM images of laser ablated Si wafer after 150 MeV Au ion irradiation with (a) 1×10^{13} and (b) 3×10^{13} ions/cm² fluence.

It may be seen from these images that the particle size varies from 40 to 100 nm in acetone. Similar kind of particle distribution was observed in other liquids such as water and methanol. However, the growth in different liquids is observed to be different. Spherical and isolated particles were observed in the sample prepared in acetone whereas the particles prepared in methanol and water were found to agglomerate over a period of time [27]. In the present investigations we focus mainly on the Si NPs synthesized by laser ablation of Si wafer in acetone. The Si NPs obtained were then irradiated with 150 MeV Au ions at different fluences. Fig 6.5 shows the FESEM surface microstructures of the 150 MeV Au irradiated Si wafer at 1×10^{13} and 3×10^{13} ions/cm² fluence. From these images, no significant changes were seen on the laser ablated area of Si wafers with the increase in fluence of ion irradiation, but the formation of smaller size Si NPs is evident from these images. The decrease in Si NP size was also visible from the images of irradiated samples.

6.3.3 TEM

Fig 6.6 depicts the TEM images of the Si NPs obtained by laser ablation of Si wafer in acetone. The solution was centrifuged on carbon coated copper grids and analyzed using TEM operated at 200 keV. These TEM images further confirm the formation of well dispersed spherical nanoparticles. The estimated size of these spherical nanoparticles was also in the same range as those observed using FESEM. The particles are observed to be clear and no smaller size NPs (6 to 9 nm) were observed in the surroundings of big NPs.

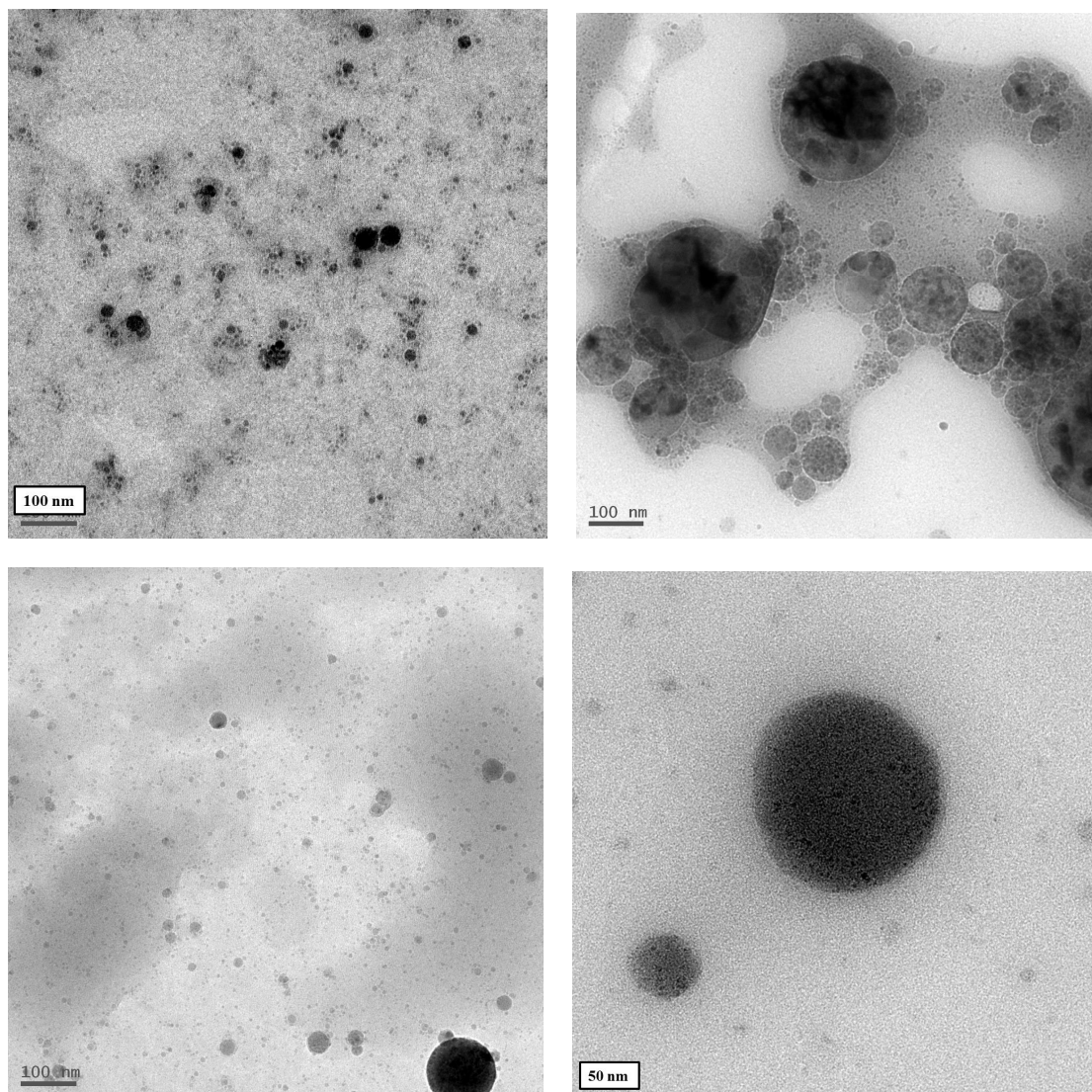


Fig 6.6: TEM images of the as prepared Si NPs in acetone by laser ablation of Si wafer (from different positions of the TEM grid).

Selective area electron diffraction patterns, shown in Figures 6.7, reveal the polycrystalline nature of the Si nanoparticles. The size distribution of the as-prepared Si NPs in acetone is given in Fig 6.8. It indicates that the average NP size in the as-prepared sample is of the order of 42 nm and there are almost no NPs in the size range 6 to 9 nm.

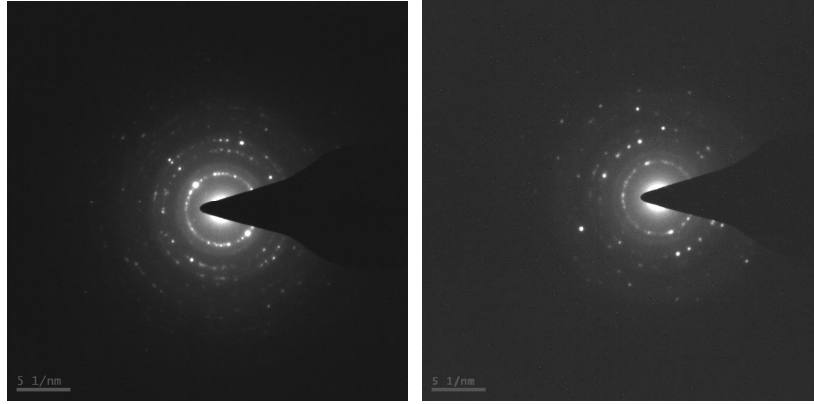


Fig 6.7: Depictions of selective area electron beam diffraction patterns from the as prepared Si nanoparticles

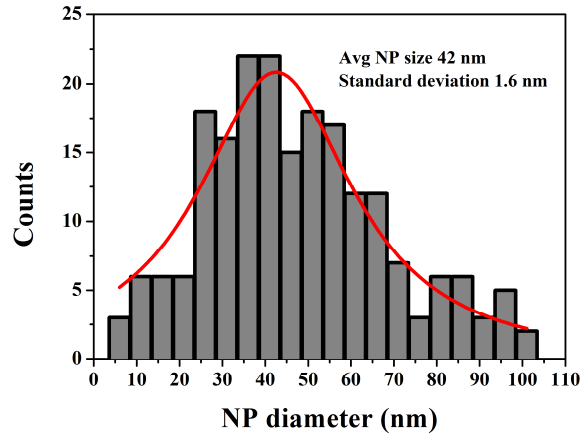


Fig 6.8: Typical size distribution histogram of the pristine Si NPs

The Si NPs on carbon coated Cu grids were directly used for 150 MeV Au ions irradiation at different fluences. Figs 6.9 (a)-(c) depict the TEM images of the 150 MeV Au irradiated Si NPs at fluences of (a) 1×10^{13} (b) 3×10^{13} and (c) 1×10^{14} ions/cm² respectively. It is clearly observed from the images that irradiation creates a hazy outline around the NPs and a growth of relatively small NPs are observed around the bigger NPs. With the increase in the fluence of irradiation the density of smaller NPs increases and from the selective area electron diffraction pattern, it is observed that the particles are getting amorphized due to heavy ion irradiation (see Fig 6.11). The size distributions of various fluence irradiated Si NPs are given in Fig 6.10. It indicates that the average NP size was reduced with the increase in fluence of irradiation. The average NP size measured from the TEM images of the various fluence

irradiated samples are given in table 6.3. With the increase in fluence of irradiation, a decrease in NP size is observed.

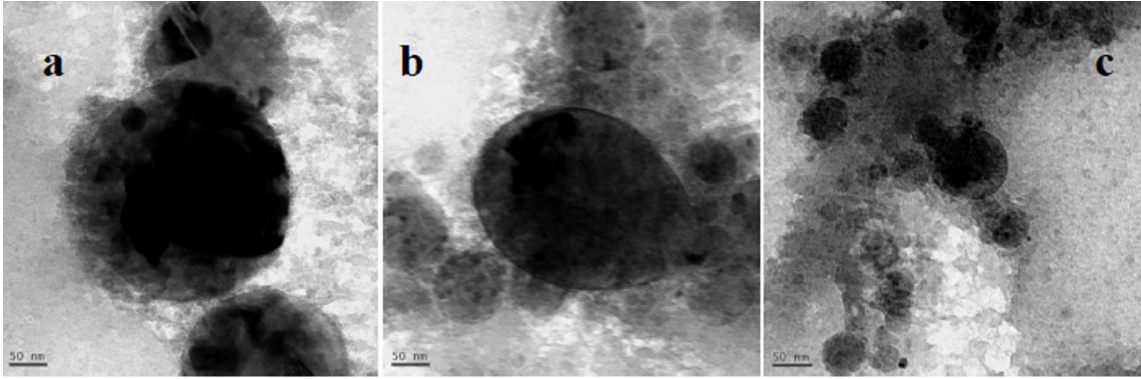


Fig 6.9: TEM images of the 150 MeV Au ions irradiated Si NPs at fluences (a) 1×10^{13} , (b) 3×10^{13} and (c) 1×10^{14} ions/cm²

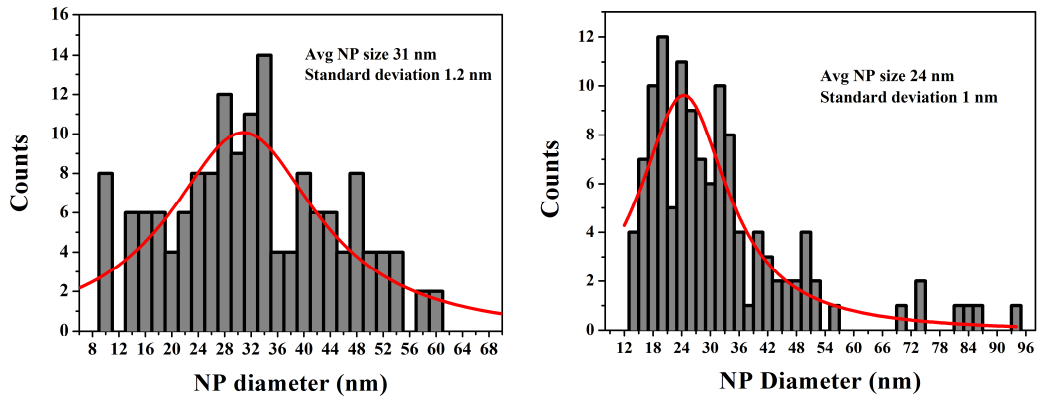


Fig 6.10: Typical size distribution histogram of the 150 MeV Au ions irradiated Si NPs at fluence (a) 3×10^{13} ions/cm² (b) 1×10^{14} ions/cm².

Table 6.3: Variation of Si NP size with ion irradiation fluence of 150 MeV Au ion irradiation.

S.No	Sample with irradiation fluence	Average NP diameter/size (nm)	Standard deviation (nm)
1	Si NPs pristine	42	1.6
3	150 MeV Au 1E13	38	1.2
4	150 MeV Au 3E13	31	1
5	150 MeV Au 1E14	24	1



Fig 6.11: Depictions of selective area electron beam diffraction patterns from the ion irradiated Si nanoparticles

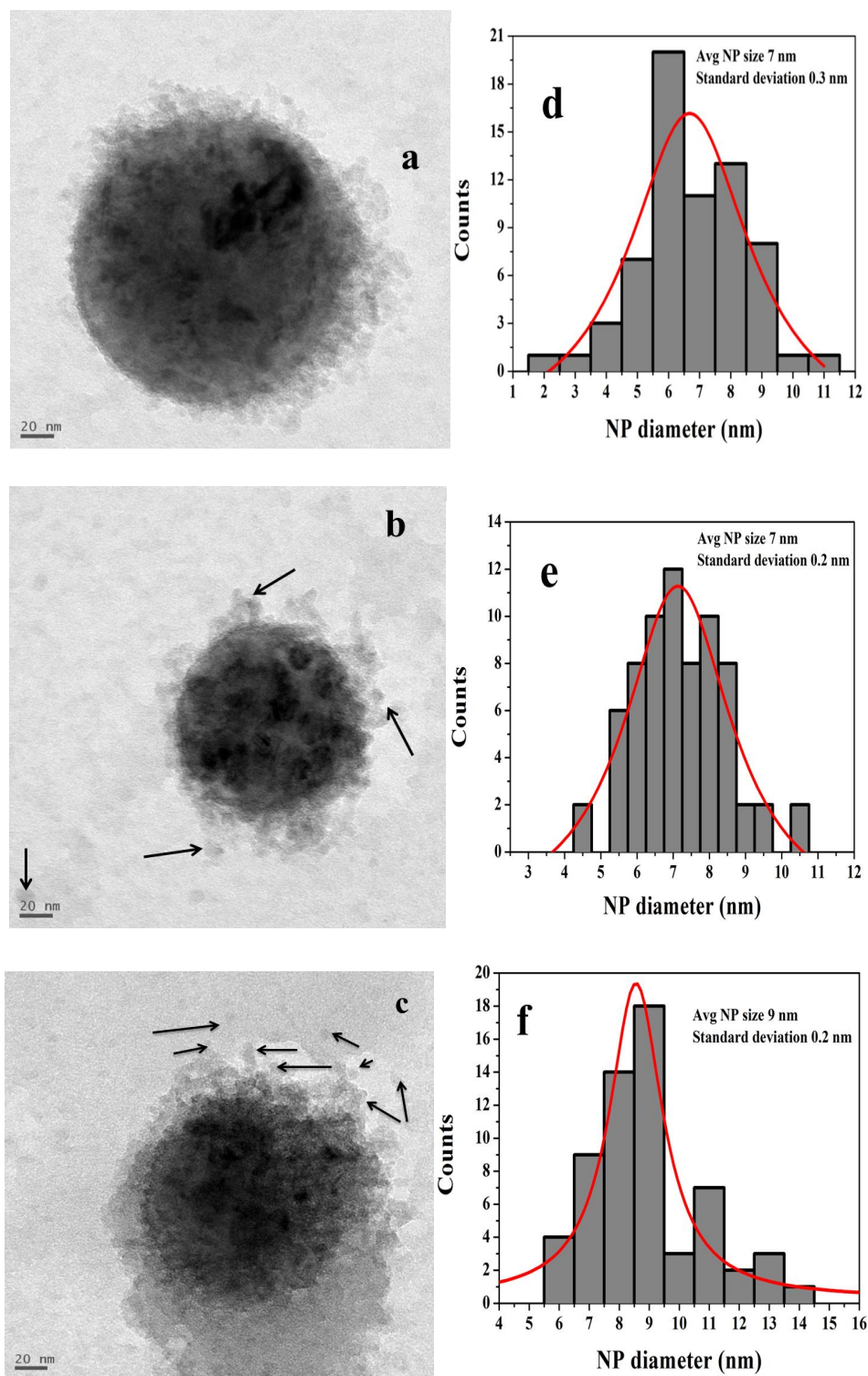


Fig 6.12: TEM image of the large Si NPs irradiated with 150 MeV Au ions at fluences (a) 1×10^{13} , (b) 3×10^{13} and (c) 1×10^{14} ions/cm² and (d)-(f) are the respective typical size distribution histograms.

Figure 6.12 shows the TEM images of bigger Si NP ($> \sim 100$ nm) irradiated with 150 MeV Au ions at 1×10^{13} , 3×10^{13} and 1×10^{14} ions/cm² fluences. It is observed that in the pristine sample (see Fig 6.6) such NPs are clear and there was no smaller size NPs in the surroundings of these big NPs. With the increase in fluence of irradiation, it was observed that smaller size NPs of the size 6 to 9 nm were formed around the big NPs. This is due to the breaking of Si atoms as a result of irradiation from the bonding and these separated Si atoms are getting agglomerated to form such type of Si NPs. This type of formation increases with the increasing fluence of irradiation. The same was observed from the TEM images and corresponding size distribution also shows the formation of these NPs of the order 6 to 9 nm with the fluence of irradiation. Furthermore the FWHM of the size distribution also decreases with the increase in irradiation fluence. It suggests that the formation of Si NPs around the surroundings of bigger NPs also increases. As indicated by Raman measurements the broad peak at 480 cm^{-1} is due to the amorphization and also due to the formation of SiO_2 . It indicates that as a result of ion irradiation, the edges of the bigger NPs which are already oxidized are getting modified with the deposited electronic energy and the Si atoms are getting removed from their bonding, get dissolved into the oxide matrix and form smaller NPs by agglomeration. The details of the smaller NPs and their FWHM of the size distribution are given in table 6.4.

Table 6.4: Formation of Si NPs with smaller size upon ion irradiation of bigger NPs at various fluences of 150 MeV Au ion irradiation.

S.No	Sample with irradiation fluence	Average NP diameter/size (nm)	Standard deviation (nm)	FWHM of size distribution (nm)
1	Si NPs pristine	--	--	--
3	150 MeV Au 1E13	7	0.3	4.76
4	150 MeV Au 3E13	7	0.2	3.63
5	150 MeV Au 1E14	9	0.2	2.15

The electronic energy loss of 150 MeV Au ions in silicon is 14.43 keV/nm (from SRIM calculation). The temperature during the irradiation will be of the order of 1500°C due to this deposited energy density. This temperature is sufficient for breaking the bonds between Si atoms to make them free and have the tendency of large displacements. With the increase in fluence of irradiation, these liberated atoms can join and form new bonds to initiate the growth of small NPs in the surroundings of the bigger NPs as a result of irradiation. During this process, amorphization of Si NPs also occurs. As the ion used for irradiation is a high energy ion there is a possibility of ion beam induced anisotropic plastic deformation of NPs which depends on the direction of incident ion beam. As a result, the NPs get elongated in the direction perpendicular to the incident ion beam and contract in the parallel direction. The amorphization of the Si nanocrystals is a well-known effect for higher doses of ions with lower energies [28, 29]. The models of thermal spike provide substantial understanding of these effects of irradiation and the thermal processes involved. Materials with large electron-phonon coupling constant are sensitive to electronic energy depositions. The effects of electron-phonon coupling play a significant role in the surface region to cause the melting followed by the amorphization. Thermal spike induced by intense electronic excitation causes the amorphization during irradiation. On the lines of the above discussion, one can conclude that the present direct observation may be interpreted as a confirmation of the occurrence of plastic flow and subsequent amorphization in swift heavy ion irradiation induced modification of these Si NPs. The fluence of the irradiating ion plays an important role in the

modification of NPs. The formation of smaller NPs in the vicinity of bigger NPs is due to the breaking of the bonding between Si atoms and the deposited energy density which is sufficient for the diffusion of the Si atoms to move in the oxidized network to form smaller Si NPs. These small NPs grow at the expense of larger ones. Therefore, the growth competition of NPs by diffusional interaction leads to a mono-disperse size distribution of NPs. This phenomenon is also called as inverse Ostwald ripening. From the TEM images it was observed that the mean NP diameter is 7 nm with a FWHM of 4.76 nm [see Fig. 6.12 (a) & (b)] after 150 MeV Au ion irradiation at 1×10^{13} ions/cm² fluence. With the increase in fluence it was observed that the evolution of the smaller NPs is more in the vicinity of bigger NPs. The mean size of Si NPs increases and the FWHM of the size distribution decreases with increasing fluences further to 3×10^{13} cm⁻² and 1×10^{14} cm⁻² [see Figs. 6.12 (b)-(f) and table 6.4].

6.4 Conclusions

We have synthesized Si-nanoparticles using pico-second laser ablation of single crystal silicon in acetone. The presence of Si-NPs in acetone and on the laser ablated area of the Si wafer is confirmed by Raman, TEM and FESEM measurements. The tuning of size and shape of these NCs using 150 MeV Au ion irradiation at various fluences was achieved and the results were understood on the basis of ion solid interaction mechanisms. With the increase in fluence it was observed that the particle size was reduced and a growth of 6 to 9 nm NPs in the surroundings of bigger NPs was observed. As a result of irradiation it was observed that the Si NPs are getting amorphized with the deposition of electronic energy by the irradiating ion. By tuning the ion irradiation parameters such as energy deposition, fluence of irradiation etc the shaping of the Si NPs can be achieved. Nonlinear optical and emission properties are being studied for these NCs. The NPs synthesized in other liquids such as water, methanol are also being used for modification of size and shape with SHI irradiation.

6.5 References

1. Y. Kanemitsu, Tetsuo Ogawa, Kenji Shiraishi, and Kyozauro Takeda Physical Review B 48 (1993) 4883.
2. L.T. Canham, Appl. Phys. Lett. 57 (1990) 1046.
3. V. Lehmann, U. Gosele, Appl. Phys. Lett. 58, (1991) 856.
4. M. Stupca, M. Alsalhi, T. Al Saud, A. Almuhanha, and M. H. Nayfeh, Appl. Phys. Lett., 91, (2007) 063107.
5. L. Ding, T. P. Chen, Y. Liu, C. Y. Ng, and S. Fung Physical Review B 72, (2005) 125419.
6. D Song, E C Cho, G Conibeer, C Flynn, Y Huang, M A Green Solar Energy Materials & Solar Cells 92 (2008) 4746481
7. Eun Chel Cho, M A Green, G Conibeer, D Song, Y Hyun Cho, G Scardera, S Huang, S Park, X J Hao, Y Huang, and Lap Van Dao Advances in optoelectronics, Volume 2007, ArticleID 68578K.
8. D. Hirschman, L. Tsybeskov, S.P. Duttagupta, P.M. Fauchet, Nature 384 (1996) 338.
9. N. Koshida, N. Matsumoto, Mater. Sci. Eng. R 40 (2003) 169.
10. Li Wei Long et al, Chin. Phys. Lett. Vol.26, No.4(2009) 046801
11. G. Vijaya Prakash, M. Cazzanelli, Z. Gaburro, L.Pavesi, F. Iacona, G. Franzò and F. Priolo, J.Appl. Phys., Vol91(7), (2002), 4607
12. Fabio Iacona, Giorgia Franzò, and Corrado Spinella Journal of Applied Physics, Vol 87, No3, (2000) 1295
13. G Kurumurthy, S Alee, D Narayana Rao Optics Communications 282 (2009) 3509.
14. G. H. Li, K. Ding, Y. Chen, H. X. Han, and Z. P. Wang Journal of Applied Physics, Vol 88, No3, (2000) 1439.

- L.pavesi, L. Dal Negro, C. Mazzoleni, G. Franzo & F. Priolo, *Nature*, Vol 408,(2000) 440.
15. N Saxena, P Kumar, D Kabiraj and D Kanjilal *Nanoscale Research Letters* 7 (2012), 547.
16. R. A. Bley and S. M. Kauzlarich, *Journal of the American Chemical Society*, vol. 118, no. 49, pp. 12461-12462, 1996.
17. P. P. Patil, D. M. Phase, S. A. Kulkarni, S. V. Ghaisas, S. K. Kulkarni, S.M. Kanetkar, S.B. Ogole and V.G. Bhide, *Phys. Rev. Lett.* 58, 238-241 (1987).
18. T. Cheung, *Pulsed laser deposition of thin films*, ed. D. B. Chrisey and G. K. Hubler (Wiley, New York, 1994), Chap-1.
19. G A Kachurin et al, *Appl Phys A* (2010) 98: 873-877
20. P S Chaudhari et al, *Journal of Applied Physics*, Vol 93, No6, (2003) 3486 P S Chaudhari et al, *Nuclear Instruments and Methods in Research B* 239 (2005) 185-190
21. D. Rodichev, Ph. Lavallard, E. Dooryhée, A. Slaoui, J. Perriere, M. Gandais, Y. Wang *Nuclear Instruments and Methods in Research B* 107 (1996) 259
22. W. M. Arnoldbik, N. Tomozeiu, E. D. van Hattum, R. W. Lof, A. M. Vredenberg, and F. H. P. M. Habraken *Phys. Rev. B* 71, (2005) 125329.
23. N Saxena, A Agarwal, D.M. Phase, R J Choudhary, D. Kanjilal, *Physica E: Low-dimensional Systems and Nanostructures* 42, Issue 9, (2010) 2190.
24. P. Mishra, K. P. Jain, *Phys. Rev. B* 62, (2000) 14790.
25. D. Nesheva, C. Raptis, A. Perakis, I. Bineva, Z. Aneva, Z. Levi, S. Alexandrova, and H. Hofmeister *J. Appl. Phys.* 92, (2002) 4678.
26. Y. Duan, J. F. Kong and W. Z. Shen *J. Raman Spectrosc.* 43, (2012) 7566-760.
27. R Brahma, S Hamad, S Venugopala Rao, S V S Nageswara Rao et.al, manuscript under preparation.

28. G F Cerofolini and L Meda Phys. Rev. B 36 (1987) 5131
29. W O Adekoya, M Hage, J C Muller and P Siffert Appl. Phys. Lett. 50 (1987) 1736

Chapter 7

Conclusions and Future Outlook

7.1 Summary of the results

In this thesis, we have presented the results on the synthesis, characterization and SHI induced modification of semiconductor (Ge & Si) NCs. Ge NCs embedded in SiO₂ matrix have been synthesized by RF sputtering followed by RTA at different temperatures. We have found that the NC size increases with the increase in annealing temperature and also with the increase of Ge composition in the Ge+SiO₂ composites the Ge NC size increased. The annealed samples have been used to study the effects of SHI irradiation on the Ge NCs. The effects of 120 MeV Ag and 80 MeV Ni ion irradiation on the size of Ge NCs have been investigated and we found that the average size of Ge NCs decreases with increase in irradiation fluence. This was confirmed by the XRD measurements of average size of Ge NCs. The Raman peak shift towards lower wavenumber side with increase in the fluence also suggests a decrease in size of Ge NCs. TEM images confirm the reduction of NC size and it also indicates the partial amorphization of NCs as a result of ion irradiation. The results have been explained using the ion-solid interaction concepts based on the electronic energy deposition by the incident ions inside both Ge and SiO₂. Ge NCs have also been synthesized by the 1 MeV Ge⁺ ions implantation into SiO₂ and followed by RTA.

Ge NCs embedded in high-k dielectric matrix HfO₂ have been synthesized by RF sputtering followed by RTA and heavy ion irradiation. Tri-layered HfO₂/Ge/HfO₂ thin films were fabricated on Si substrate and the as-deposited samples were annealed using RTA at various temperatures. XRD results reveal the formation of crystalline structure in the annealed samples while the as-deposited samples were amorphous in nature. The average size of the Ge NCs is found to increase with increase in the annealing temperature. According to micro-Raman spectra, the annealed samples exhibit a shift in the peak position which clearly indicates the formation of Ge NCs in HfO₂ matrix. SHI irradiation has been used as an alternative method for the formation of Ge NCs in HfO₂ and the XRD and micro-Raman spectroscopy measurements suggest the presence of Ge NCs in the ion irradiated samples. The formation of Ge NCs in HfO₂ matrix as a result of ion irradiation has been understood by a process called ion beam induced annealing based on the controlled electronic energy deposition by incident ions resulting in annealing and re-crystallization in the target material.

This process has advantage of a better control using the ion beam parameters (including spatial control) which is not possible in usual thermal annealing.

The GeO₂ NC thin films have been deposited by RF sputtering and the effects of 80 MeV Ni ions irradiation at various fluences on GeO₂ NCs was studied. The change in NC size with ion fluence has been discussed. The average size of GeO₂ NCs is found to decrease with increase in the irradiation fluence. A removal of oxygen and formation of smaller Ge NCs from GeO₂ takes place during ion irradiation and hence a decrease in the NC size has been observed due to irradiation. Surface morphology and modifications induced by ion irradiation was clearly understood from FESEM microstructures. Micro-Raman spectroscopy studies show clearly the formation of Ge NCs with the increase of irradiation fluence. From the combined micro-Raman, FESEM and TEM observations of irradiated samples, we see the formation of Ge NCs close to the regions of GeO₂ rich particles when irradiated with 80 MeV Ni ions. The results have been explained by the diffusion of oxygen from one position to another position with the electronic energy deposition by the incident ions.

Lastly we have studied the effects of SHI irradiation on Si nanoparticles synthesized by using pico-second laser ablation of single crystal silicon in acetone. The tuning of size and shape of these NPs using 150 MeV Au ion irradiation at various fluences was achieved and the results have been understood on the basis of ion solid interaction mechanisms. With the increase in fluence it is observed that the particle size reduces and a growth of 6 to 9 nm NPs in the surroundings of bigger NPs has been observed. As a result of irradiation the Si NPs are getting amorphized with the deposition of energy by the irradiating ion. By tuning the ion irradiation parameters such as energy deposition, fluence of irradiation etc the shaping of the Si NPs can be achieved.

7.2 Future Perspectives

Semiconductor (Ge & Si) NCs based materials have garnered great attention as a promising candidate for charge storage device applications as nonvolatile memory. The charge storage property of semiconductor NCs embedded in a dielectric matrix is currently under extensive investigation due to their potential applications in non-volatile memory applications. We have achieved the synthesis of Ge NCs embedded in SiO₂ as well as high-k dielectric HfO₂

matrices. We have studied the effects of heavy ion irradiation on the Ge NCs embedded in SiO₂ and observed the modification of size and shape of the NCs as a result of irradiation. Preliminary application related experiments are being initiated and those are in progress. To understand more about the irradiation induced effects such as formation of Ge-O bonds and the percentage of amorphization of Ge NCs, the samples will be analysed by using synchrotron based X-ray absorption and emission studies. The work on the Ge NCs embedded in HfO₂ has just started and the detailed study of the synthesis and characterization of Ge NCs in HfO₂ by co-sputtering and the effects of annealing atmosphere, type of annealing and the effects of heavy ion irradiation on Ge NCs embedded in HfO₂ will be planned for future. The extension of embedded Ge NCs synthesis to other dielectric matrices such as Al₂O₃, MgO, ZrO₂ etc. is also planned for future. Annealing of the ion irradiated GeO₂ NCs samples at a relatively low temperature to recover the crystalline state and to observe the growth of Ge NCs in the ion-beam modified GeO₂ NCs will be interesting and is planned for future. Nonlinear optical and emission properties are being studied for these Ge NCs. The effects of SHI irradiation with varied fluences on Si NPs, synthesized by laser ablation of Si wafer in acetone, have been studied and we will extend the same methodology to see the effects of electronic energy loss dependence by choosing other ions (80 MeV Ni and 100 MeV Ag) to see the modifications induced by SHI irradiation on the Si NPs. The Si NPs synthesized in other liquids such as water, methanol will also be used for ion irradiation studies for the modification of size and shape with SHI irradiation with different energies and at varied fluences.

With all the above investigations it will be possible to use ion irradiation as an interesting tool in controlled nanostructuring of various materials to modify their properties for many technologically important applications.

CURRICULAM VITAE

SAIKIRAN VADAVALLI

Research Scholar,
School of Physics,
University of Hyderabad,
Hyderabad- 500046. India.

Email: saivadavalli@gmail.com
Contact number: +91 9908041411

Current Position: Submitted Ph.D thesis entitled *õSynthesis, characterization and swift heavy ion induced modification of semiconductor (Ge & Si) nanocrystals* in July 2013 under the supervision of Prof Anand P Pathak, School of Physics, University of Hyderabad.

Publications related to the thesis work:

1. Ion beam irradiation effects on Ge nanocrystals synthesized by using RF sputtering followed by RTA V **Saikiran**, N Srinivasa Rao, G Devaraju, G S Chang and A P Pathak (*in press Nucl. Inst. Meth B* 2013).
2. Formation of Ge nanocrystals from ion-irradiated GeO₂ nanocrystals by swift Ni ion beam V **Saikiran**, N Srinivasa Rao, G Devaraju, G S Chang and A P Pathak (*Accepted in Nucl. Inst. Meth B*).
3. Synthesis, Characterization and Dense Ionization effects on Ge nanocrystals embedded in SiO₂ V **Saikiran** and A P Pathak (*MS under preparation*).
4. Synthesis and characterization of Ge nanocrystals embedded in HfO₂ matrix V **Saikiran** and A P Pathak (*MS under preparation*).
5. Study of swift heavy ion irradiation effects on Si nanoparticles synthesized by picosecond laser ablation in liquids V **Saikiran**, S. Hamad, V S Vendamani, S V S Nageswara Rao, S V Rao, S P Tewari and A P Pathak (*MS under preparation*).

Other Publications:

6. SHI irradiation induced effects in functionalized MWCNTs V **Saikiran**, A P Pathak et.al, *Radiation Effects and Defects in Solids*, Vol 167 (2012) 569.
7. Anharmonic effects on positron channeling angular scans and dechanneling due to stacking faults and platelets V S Vendamani, S Balamuragan, V **Saikiran**, A P Pathak and S V S Nageswara Rao *Radiation Effects and Defects in Solids*, Vol 167 (2012) 594.

8. Synthesis and Tailoring of GaN nanoparticles by RF magnetron sputtering at Room Temperature G Devaraju, A P Pathak V **Saikiran** et al *Radiation Effects and Defects in Solids, Vol 167 (2012) 659*.
9. Synthesis and Characterization of Ge nanocrystals prepared by using microwave annealing N Srinivasa Rao, A P Pathak, G Devaraju and V **Saikiran**, *Vacuum 85 (2011), 927*.
10. Synthesis of Ge nanocrystals by atom beam sputtering and subsequent rapid thermal annealing N Srinivasa Rao, A P Pathak, N Sathish, G Devaraju, V **Saikiran**, P K Kulriya, D C Agarwal, G Sai Saravanan and D K Avasthi, *Solid State Communications 150 (2010), 2122*.

International and national conferences:

1. Structural and optical properties of Ge nanocrystals embedded in SiO₂ prepared by 1 MeV Ge implantation Oral presentation at 22nd International Conference on the Application of Accelerators in Research and Industry (CAARI 2012), held at Fort Worth, Texas, USA during August 5th to 10th, 2012.
2. Effects of Ion irradiation on GeO₂ nanocrystals-fluence dependence study Poster presentation at 22nd International Conference on the Application of Accelerators in Research and Industry (CAARI 2012), held at Fort Worth, Texas, USA during August 5th to 10th, 2012.
3. Synthesis of Si nanocrystals embedded in SiO₂ matrix Poster presentation as a young researcher at International Conference on Nanoscience and Nanotechnology (ICONSAT 2012) in Hyderabad during January 20th to 23rd 2012.
4. SHI irradiation induced effects in functionalized MWCNTs poster presentation at winter school on physics and chemistry of materials held at JNCASR Bangalore during 05th Dec to 10th Dec 2011.
5. Ion beam irradiation effects on Ge nanocrystals synthesized by using RF sputtering followed by RTA Poster presentation at 25th International Conference on Atomic Collisions in Solids (ICACS 2012), held at Kyoto Japan during October 21st to 25th 2012 (presented by Prof A P Pathak).
6. Synthesis, Characterization and Dense Ionization effects on Ge nanocrystals embedded in SiO₂ Poster presentation at 21st International Conference on Ion Beam Analysis (IBA62013), held at Seattle, WA, USA during August 23rd to 28th, 2013 (presented by Dr S V S Nageswara Rao).
7. Study of swift heavy ion irradiation effects on Si nanoparticles synthesized by picosecond laser ablation in liquids Poster presentation at 21st International Conference on Ion Beam Analysis (IBA62013), held at Seattle, WA, USA during August 23rd to 28th, 2013 (presented by Dr S V S Nageswara Rao).

Educational details:

- *Ph.D (Physics)* under the supervision of Prof A P Pathak, School of Physics, University of Hyderabad (thesis submitted in July 2013).
- All the necessary Ph.D course works have been completed with distinctions both at University of Hyderabad and IUAC, New Delhi in 2008.
- *M.Sc (Nuclear Physics)* with distinction (71.8%) from Department of Nuclear Physics, Andhra University, Visakhapatnam in 2004.
- *B.Sc (M P C)* with 85.3% from Acharya Nagarjuna University in 2002.

Research Experience:

- Worked as a *CSIR JRF* under the supervision of Prof A P Pathak from August 2008 to July 2010.
- Worked as a *CSIR SRF* under the supervision of Prof A P Pathak from August 2010 to July 2013.
- Worked as a *Graduate Visiting Scholar* under the supervision of Prof G S Chang at Department of Physics and Engineering Physics, University of Saskatchewan, Saskatoon, Canada from October 2012 to March 2013 through *Canadian Commonwealth Graduate Student Scholarship*.

Teaching Experience:

- Worked as a Lecturer in Physics at ANRPL College, Gudivada from July 2004 to May 2005.
- Worked as a Lecturer in Physics at The Hindu College, Machilipatnam from June 2005 to July 2007.
- Worked as a Lecturer in Physics at Narayana IIT Academy, Vijayawada from August 2007 to April 2008.
- Worked as a teaching assistant at University of Hyderabad for the following courses during 2008-2013.

Advanced Quantum Mechanics

Semiconductor Physics

Digital Electronics

Nuclear Physics Laboratory

Achievements:

- Selected for Canadian Commonwealth Graduate Student Scholarship.
- Qualified for CSIR JRF in UGC CSIR NET 2007 conducted by CSIR, New Delhi.
- Topper in the Ph.D course work at University of Hyderabad.
- 2nd rank in M.Sc Nuclear Physics at Andhra University.
- College topper during B.Sc.

Computer Knowledge:

Programming knowledge of C,
FORTRAN programming,

Instruments: Handling Expertise / Operated:

RF Magnetron Sputtering system

E-beam evaporation equipment

Physical Vapour Deposition

Sample preparation using spin coating method

Confocal micro-Raman spectrometer

X-ray diffractometer

Atomic force microscope (AFM)

Scanning electron microscope

UV-Vis-NIR absorption spectrometers (Varian-Cary 5000)

Transmission electron microscope and sample preparation method

Ion implantation, Ion irradiation and RBS based accelerator facilities (principles of operation)

RTA and normal furnace annealing instruments

Personal details:

Name : V. Saikiran
Father's Name : V. G. K. Rao
Date of Birth : 22-05-1982
Languages Known : English, Hindi and Telugu
Marital Status : Married

References:

1. Prof A P Pathak,
School of Physics,
University of Hyderabad,
Central University (P.O),
Hyderabad - 500 046,
appsp@uohyd.ernet.in anandp5@yahoo.com
2. Prof G S Chang,
Department of Physics and Engineering Physics,
University of Saskatchewan,
Saskatoon, Canada.
gapsoo.chang@usask.ca gapsoo.chang@gmail.com
3. Dr S V S Nageswara Rao,
School of Physics,
University of Hyderabad,
Central University (P.O.),
Hyderabad- 500046.
nageshphysics@gmail.com svnsp@uohyd.ernet.in